Plasmonic-enhanced THz generation and detection using photoconductive antennas

by

Afshin Jooshesh
B.Sc., Islamic Azad University, 2007
M.Sc., Islamic Azad University, 2010

A Dissertation Submitted in Partial Fulfillment
of the Requirements for the Degree of

DOCTOR OF PHILOSOPHY

in the Department of Electrical and Computer Engineering

Supervisory Committee

Plasmonic-enhanced THz generation and detection using photoconductive antennas

by

Afshin Jooshesh
B.Sc., Islamic Azad University, 2007
M.Sc., Islamic Azad University, 2010

Supervisory Committee

Dr. Thomas Edward Darcie, (Department of Electrical and Computer Engineering)
Co-Supervisor

Dr. Reuven Gordon, (Department of Electrical and Computer Engineering)
Co-Supervisor

Dr. Dennis Hore, (Department of Chemistry)
Outside Member

Abstract

Supervisory Committee

Dr. Thomas Edward Darcie, (Department of Electrical and Computer Engineering)
Co-Supervisor

Dr. Reuven Gordon, (Department of Electrical and Computer Engineering)
Co-Supervisor

Dr. Dennis Hore, (Department of Chemistry)
Outside Member

Terahertz technology is rapidly growing for applications in various fields such as medical sciences, remote sensing, material characterization, and security. This accelerated growth has motivated engineers to develop compact, portable, and cost-effective terahertz sources and detectors. Terahertz generation and detection can be achieved using photoconductive antennas (PCAs), which have unique advantages. Notably, they do not require a vacuum or cryogenic cooling to function. PCAs operate on the principle of photoconductivity, which allows for compact integration with a fiber optic laser. It is also possible to launch THz radiation to a waveguide, which can be used for making a robust THz spectroscopy system.

Ultra-short laser pulses are available in both 800 nm and 1550 nm wavelengths. However, the 1550 nm window has distinctive advantages such as availability of fiber amplifiers and fiber based electro-optical components at a relatively lower cost. The goal of this research is to introduce cost-effective and state-of-the-art solutions to develop THz transceivers for use in terahertz time-domain spectroscopy (THz-TDS) at 1550 nm wavelength.

In this thesis we explore three approaches for enhancing THz emission and reception using PCAs. First, an array of hexagonal shape plasmonic nano-structures was used to increase the optical field coupling to the minimum depth of the substrate. Next, nano-structures also helped with enhancing the local electric field inside a low-cost semi-insulating GaAs substrate. This technique resulted in a 60% enhancement of the THz emission compared to a commercial LT-GaAs based PCA with antireflection coating. Moreover, the plasmonic nano-structures efficiently remove heat from the gap area allowing for operation at higher bias voltages. Plasmonic structures on LT-GaAs were investigated, which use a mid-gap Arsenic defect state to absorb 1550 nm light. The plasmonic devices were found to outperform existing InGaAs substrate based THz devices by factor of two. Finally, optimization of the LT-GaAs growth and annealing conditions was investigated to maximize the THz signal at 1550 nm. Outcomes of this research pave the way for designing cost-effective THz transceivers for time domain Terahertz spectroscopy systems at 1550 nm wavelength.

Table of Contents

List of Tables

List of Figures

Acknowledgments

There are many, without whom this work would not have been possible and whom I would like to express my gratitude.

First, I would like to thank my family for their endless support and love. Specifically, my mother Dr. Parisa Nejatkhah Manavi and my wife Yasaman Akbari and my brother Armin Jooshesh. It was indeed your encouragement that inspired me to come this far.

I sincerely appreciate Prof. Thomas E. Darcie for his trust, infinite support, and great leadership. With the same gratitude, I would like to thank Prof. Reuven Gordon for his supervision and guidance. It was truly a privilege to work with you and in your team. This multi-disciplinary project required communication and collaboration with different groups and laboratories at the University of Victoria. Hereby, I would like to take this opportunity to thank Prof. T. Tiedje, the director of the MBE and Thin Film Fabrication Laboratory, for supporting this research. Furthermore, I would like to thank Dr. Elaine Humphrey and Adam Schuetze for providing the training and the access to the nanofabrication facilities.

Last but not least, I would like to thank my friends and colleagues, Levi Smith, Vahid Bahrami Yekta, Mostafa Masnadi Shirazi and Jinye (James) Zhang for their valued contributions to this project.

I would like to dedicate this work in memory of my father Dr. Hossein Jooshesh and grandfather Colonel Jafar Nejatkhah Manavi.

Chapter 1 : Introduction

1.1. THz waves and applications

Naturally occurring Terahertz (THz) radiation or T-ray lies between infra-red and microwave regions of the electromagnetic spectrum with photon energy of 1.24 - 12 meV (Fig. 1.1). Electronics and microwave devices have hardly reached to 1 THz and semiconductor technology does not support such low energy transitions at room temperature to make THz emitters. The lack of technologies in both sides led to the THz spectrum being the so-called "THz gap". The demand for high power THz transmitters and receivers is growing recently and the gap has been narrowed rapidly in the last two decades [1, 2].

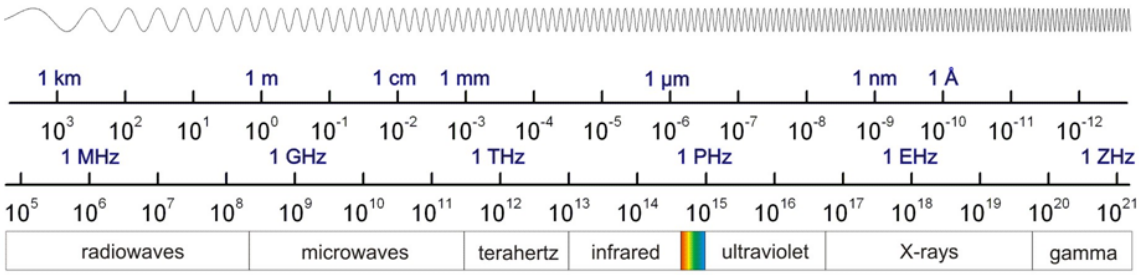

Figure 1.1 Terahertz wave spectrum. The range starts from 300 GHz to 10 THz. [3].

The low photon energy nature of the terahertz waves offers unique applications. Many opaque materials in the visible spectrum are transparent at THz region and some have trace absorption lines [4, 5]. The frequency dependent transmission of THz waves

through samples reveal unique fingerprints of materials. Each molecule or compound such as biological samples have unique characteristic rotational energy levels that determine precise frequencies of the absorption lines [6-8]. The distinctive signatures of rotational spectra have been used for decades to identify chemicals. This process has been applied to the areas of security (identifying explosives) [9-14], atmospheric remote sensing, and analysis of far galaxies [15]. The Herschel Space Observatory (http://herschel.esac.esa.int/) and NASA's Aura satellite (http://mls.jpl.nasa.gov/) are few examples. Monitoring the ozone layer in Antarctica is another noteworthy example of remote sensing of molecular compounds using the THz spectrum [16]. In the past few decades, researchers made significant contributions to collect and organize molecular transition lines both experimentally and numerically. HITRAN (http://cfa-www.harvard.edu/hitran//) and JPL Spectral catalog (http://spec.jpl.nasa.gov/) are two common databases available online [1].

Spectroscopy using T-rays has already found numerous applications in microscopy [12, 17], medicine [6, 18, 19], and material characterization [20]. Hence, terahertz science links a wide range of disciplines including physics, chemistry, engineering, astronomy, and biology.

THz imaging has entered the crowded field of imaging technologies just recently and is still in its infancy. Nevertheless, it has shown exclusive features in comparison with optical, infrared, and x-ray imaging techniques. T-rays penetrate deep into materials with low polarizability such as paper, plastic, clothes, wood, and ceramics. Because these are commonly used in packaging, T-rays are potentially strong replacement to x-ray scanners where destructive effects of high energy photons to the sample are a big concern. The

contrast between reflective metallic materials and partially transparent plastic packages facilitates the inspection of suspicious items or electronic circuits at places like airports (Fig. 1.2).

THz imaging of living tissues or hydrated substances exhibit a strong sensitivity to water [4, 19, 21]. Fig. 1.2 (left) shows water content of a leaf with darker shade indicating more water. T-ray imaging can effectively identify explosives, chemicals, and biological compounds concealed underneath covering substances [9, 13, 18].

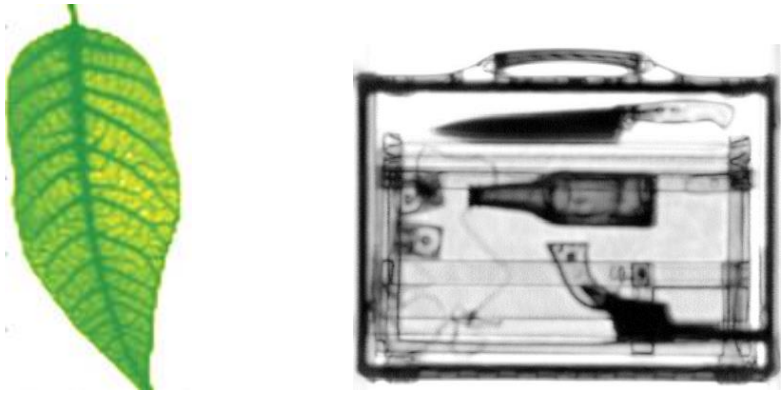

Figure 1.2 Left: THz image of a coffee leaf taken by TOPTICA TeraBeam module [22]. Right: THz image of a briefcase containing threat objects [23].

A big advantage of T-ray imaging is that it is non-invasive and non-contact. Medical imaging using THz radiation can reveal water content in living tissues. Recognising the onset of cancer [19], characterizing burn injuries [24], and identifying tooth decay [25] are few other examples of T-ray imaging in the medical world.

1.2. THz technology

The quest to design a compact, portable, room temperature, and cost effective THz devices led engineers to delve into ultra-fast properties of the materials and charged particles. Conventional particle accelerators such as klystrons, gyrotrons, backward wave oscillators, and free electron lasers need vacuum and huge magnets that make them big

and bulky [1, 26]. Thus, scientists are looking for alternative methods. With low tunability, quantum cascade lasers (QCLs) are well known THz emitters but they need cryogenic cooling that relies on big and expensive laboratory equipment. From the microwave region, radiation frequency of Schottky diodes, and impact ionization avalanche transit-time diodes (IMPATT diodes) have barely reached to 1 THz [27, 28]. Yet, they were unable to close the THz gap (Fig. 1.3).

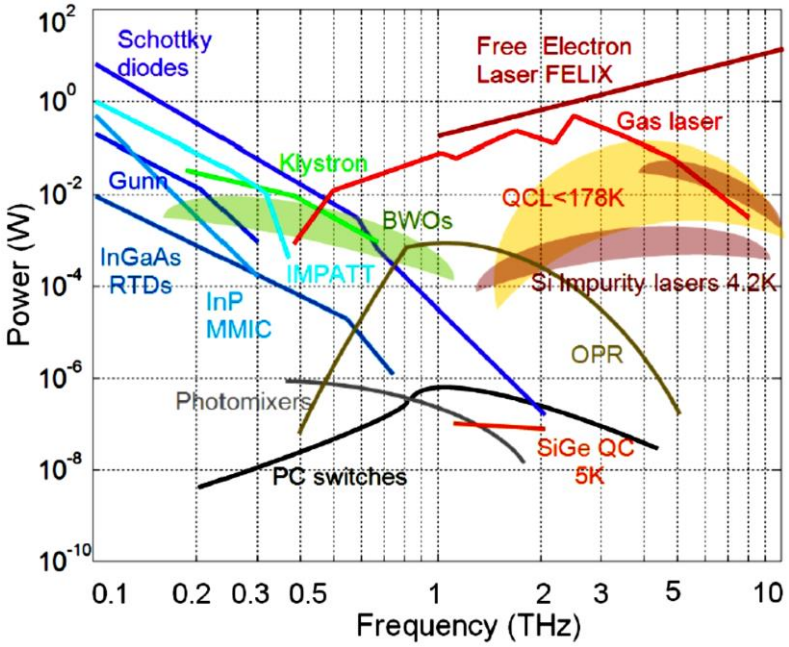

Figure 1.3 Radiation power comparison of various THz emitters. Shaded areas belong to sources with very narrow bandwidth [29].

Meanwhile, devices based on photoconductive materials are pioneers in the THz industry because of their compact size and lower price. Photoconductive antennas (PCA) are composed of an antenna fabricated on a photoconductive material. The impedance of the gap between arms of the antenna modulates by an externally incident optical pulse that in fact imitates the response of an electro-optical switch with an ultra-fast rise/fall time i.e. a photoconductive (PC) switch. Bandwidth and output power of PCAs can scale

up with proper engineering of the switch structure. In addition, they do not need cryogenic cooling or vacuum. Due to these promising features, PCAs have become an interesting field of research in the THz industry.

1.3. Technological limitations of lasers and materials

The future of the THz industry is dependent on whether THz devices can be designed and packaged in a compact and portable size with inexpensive components. Thus, it is less likely for THz devices that need cryogenic cooling, vacuum or bulky magnets to win future markets. Here, THz generation using photoconductive antennas has a promising future because it only requires external lasers, photoconductive materials, simple fabrication processes, bias, and axillary equipment such as a lock-in-amplifier to read the THz detected photocurrent. More importantly, a simple photoconductive antenna can radiate and detect THz waves, significantly reduceing the complexity of designing transmitters and receivers.

Ti:Sapphire lasers are commonly used for generating femtosecond optical pulses around 800 nm wavelength for THz time domain spectroscopy (THz-TDS). They can deliver few watts of optical power but they are expensive, big, and require free space alignment. Fiber coupled femtosecond lasers at 1570 nm are several times less expensive, compact, and their wavelengths are in the range of Erbium-doped fiber amplifiers (EDFAs). EDFAs can deliver huge amounts of optical power at a relatively low price. Furthermore, moving to the telecom window (1530 -1625 nm) has additional advantages. Mature electro-optical technology exists in the telecom window e.g. optical modulators, compensating fibers, fiber delay lines, optical couplers, etc. that eliminate the need for a free space optical layout.

Next step is finding a photoconductive material for the telecom window. While low-cost GaAs and InP are well suited semiconductors for 800 nm excitation wavelength, photoconductive materials in the telecom window are rare, inefficient, and expensive. Semiconductors with small bandgaps like InAs are highly conductive. InGaAs is a less conductive substrate but its carrier lifetime is long. As an alternative approach, it is possible to use a periodically poled lithium niobate (PPLN) nonlinear crystal to generate second harmonic of 1570 nm laser at the location of a GaAs based emitter. But, the goal of this thesis is find a low-cost photoconductive material solution that can directly absorb 1570 nm.

In short, the conceptual THz system can become a reality if PCAs are excited in the telecom window. Transceivers must be fiber coupled and there should be a possibility to launch THz waves into a waveguide rather than free space. This rugged design ensures operation of a portable THz system outside the laboratory environment.

1.4. Scope and outline of this thesis

During past few years, many ideas and methods have been tested at the University of Victoria to develop efficient, low-cost, and compact THz transmitters and receivers. Photoconductive antennas were core elements for all works because PCAs allow waveguide coupling, which is challenging in case of optical rectification. The objectives of this thesis are to enhance THz generation and detection by optimizing antennas, photoconductive materials, and laser coupling to the semiconductors that must eventually push the THz technology to the telecom window. This thesis is written in a standard dissertation format. Thus, the main text gives details on physical theories, innovative ideas, fabrication processes, and experimental results.

The chapters are organized as follows: Chapter 2 reviews fundamentals of THz generation and detection with a THz-TDS setup and recent achievements in development of PCAs around both 800 nm and 1550 nm wavelengths. Chapter 3 explains recipes that were used for in-house fabrication of PCAs and measurement methods to reproduce the results. Chapter 4 describes the design of plasmonic structures, numerical simulation methods, and experimental results. Chapter 5 investigates approaches to optimize materials for THz generation and detection at the telecom spectrum. Finally, contributions of this work to future developments and summary are given in Chapter 6.

1.5. Motivations and contributions

THz transmitters and receivers are the main parts of THz-TDS systems. Yet, PCAs are not powerful and materials are not efficient to utilize advantages of the telecom window. This thesis is an endeavour to find innovative solutions for the rapidly growing THz industry. The major contributions of this thesis are the development of plasmonic structures and material optimization for future waveguide-based portable THz-TDS with 1550 nm excitation. Results in Chapters 4 and 5 have been either published or submitted to peer-reviewed journals and can be found in Appendices. . Contributions of the authors are:

- **Nanoplasmonics enhanced terahertz sources.**

  Optics. Express 2014, 22 (23), 27992-8001, DOI: 10.1364/OE.22.027992

  The manuscript was written by Afshin Jooshesh and Prof. Reuven Gordon. Sample fabrication was done by Afshin Jooshesh, Vahid Bahrami Yekta and Mostafa Masnadi. THz emission and detection results were measured by Levi

Smith and Afshin Jooshesh. The project was founded and supported by Prof. T. Darcie and Prof. R. Gordon.

- **Plasmon-enhanced below bandgap photoconductive terahertz generation and detection**

  Nano Letters 2015, 15 (12), 8306-10, DOI: 10.1021/acs.nanolett.5b03922

  The manuscript was written by Afshin Jooshesh and Prof. Reuven Gordon. Sample fabrication was done by Afshin Jooshesh and Vahid Bahrami Yekta. THz emission and detection results were measured by Afshin Jooshesh. The project was founded and supported by Prof. T. Darcie, Prof. R. Gordon, and Prof. T. Tiedje.

- **THz field enhancement by antenna coupling to a tapered thick slot waveguide**

  Journal of Lightwave Technology 2014, 32 (20), 3676-3682.

  DOI: 10.1109/jlt.2014.2321992

  The manuscript was written by Levi Smith. Sample fabrication was done by Levi Smith and Farid Ahmed. Measurements were done by Levi Smith and Afshin Jooshesh. The project was founded and supported by Prof. T. Darcie. Jinye Zhang provided his knowledge of optics and material, which helped with interpreting the measured data.

- **Plasmon-enhanced below bandgap photoconductive terahertz generation and detection**

  Patent: filed in January 2016

  The patent was written by Prof. Darcie and Prof. Reuven Gordon. Sample fabrication was done by Afshin Jooshesh. THz emission and detection results were measured by Afshin Jooshesh. The project was founded and supported by Prof. T. Darcie, Prof. R. Gordon.

- **THz-TDS Using a Photoconductive Free-Space Linear Tapered Slot Antenna Transmitter**

  IEEE PHOTONICS TECHNOLOGY LETTERS, Submitted

  The manuscript was written by Levi Smith. Sample fabrication was done by Levi Smith. Measurements were done by Levi Smith and Afshin Jooshesh. The project was founded and supported by Prof. T. Darcie.

Chapter 2 : Background theory and literature review

2.1. THz generation and detection

GaAs and InGaAs are popular materials for photoconductive THz generation and detection in both time domain (TD) and frequency domain (FD) operation modes [1]. In this section THz generation and detection in both time domain and frequency domain will be explained. We rely on photoconductive antennas to elucidate the ultra-fast mechanism involved in each mode of operation.

It is also possible to exploit nonlinear properties of crystals to generate THz radiation, which is called optical rectification. Thus we finally review advantages and disadvantages of using photoconductive antennas as opposed to nonlinear crystals for THz generation and detection.

2.1.1. Time domain operation

In a typical THz time domain spectroscopy (THz-TDS) setup, a femtosecond laser pulse is split and focused on a transmitter and a receiver as shown in Fig.2.1. The transmitter is biased and the receiver is directly connected to a lock-in-amplifier. The femtosecond pulse delivers a large amount of current that shorts the electrodes of the transmitter that generates an instant current surge with THz frequency components. The THz pulse propagates through the media, which affects its phase or spectrum. The THz pulse and the optical (probe) beam should reach the receiver antenna at a same time to ensure detection. A delay line is usually placed to provide a variable time frame for

plotting the signal. The time averaged current of the detector is measured by the lock-in-amplifier and its spectrum is obtained by taking its Fourier transform over the current time frame.

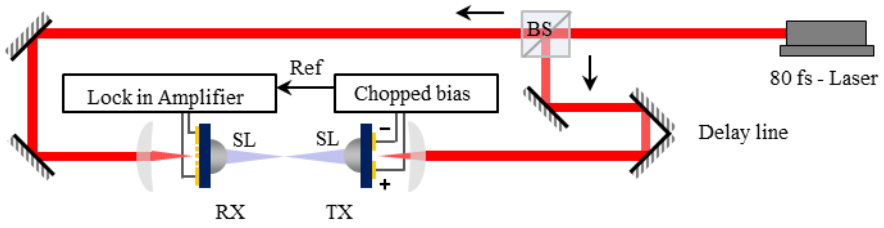

Figure 2.1 Optical setup for time domain THz spectroscopy. RX is the receiver and TX is the transmitter. SL is silicon lens and BS is a beam splitter.

For sake of simplicity, the term “active area” is used in this thesis to call the gap area under exposure. Detection in a time domain setup is basically sampling. The active area of the detector is similar to a simple switch. In fact, both switch-on and switch-off actions must occur very fast i.e. sampling with impulses. Thus, it is preferred for the receiver to have a short (sub-picosecond) carrier life-time to maximize the bandwidth.

2.1.1.1. Photoconductivity

Photon absorption is the first and most important process in photoconductive material. In Fig. 2.2, the resistance of the photoconductive material changes when photons are absorbed. For a direct band-gap photoconductive material like semi-insulating GaAs, a single photon with energy ($h\nu$, Planck's constant × frequency of the beam) equal or above the band-gap excites an electron to the conduction band, leaving a hole in valence band of the semiconductor. Absorption occurs inside the material and decays exponentially with an absorption coefficient rate α. Thus, the light intensity I at the depth of x from surface can be calculated from $I = I_o e^{-\alpha x}$ with respect to its initial value I_o. For

example, the depth corresponding to 99% absorption of the light is about 1 micron for GaAs at 800 nm excitation.

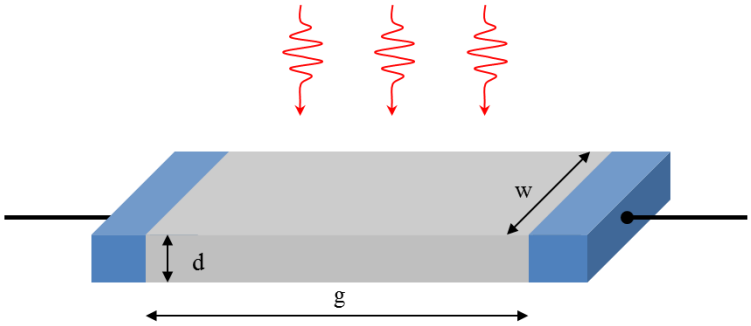

Figure 2.2 Photoconductive material under light exposure.

In order to understand the time varying resistivity of a photoconductive material we can start the modeling by considering the Drude-Lorentz model and the fact that the resistance is $R = g/(\sigma dw)$ with length g, width w, thickness d and cross section area $A=w\times g$. In this relation conductivity is $\sigma = n_o q\mu_n + p_o q\mu_p$. Since mobility of the electron μ_n is about 20 times greater than that of the hole μ_p in GaAs, we can write the time varying carrier density *n(t)* in a semiconductor, with contribution of electrons only [30]

$$\frac{dn(t)}{dt} = \frac{eP(t)\eta_{ext}}{h\nu Ad} - \frac{n(t)}{\tau}. \tag{2.1}$$

Here τ is the carrier lifetime and $\eta_{ext} = (1-\Gamma)(1-e^{-\alpha d})$ is the external quantum efficiency when Γ is surface reflection. Now by considering a Gaussian envelope of the beam in time, we can write the power

$$P(t) = P_0 \exp\left[-4\ln 2(\frac{\tau}{\Delta t})^2\right], \tag{2.2}$$

where P_o is the power of each pulse on the semiconductor. The time dependent number of electrons can be derived by replacing the equation (2.2) to the differential equation (2.1) and solving it for *n(t)*

$$n(t) = \frac{eP_0\eta_{ext}\Delta t}{h\nu Ad}\frac{\sqrt{\pi}}{4\sqrt{\ln 2}}e^{-t/\tau}e^{\frac{-\Delta t^2}{\tau^2 16\ln 2}}\left\{erf\left(\frac{\frac{1}{\tau}\Delta t}{4\sqrt{\ln 2}}\right) - erf\left[\frac{\frac{1}{\tau}-\frac{8\ln 2}{\Delta t^2}t}{4\sqrt{\ln 2}}\Delta t\right]\right\} + n_i, \quad (2.3)$$

where Δt is the duration of the laser pulse. Finally, the time dependence resistance of the substrate will be

$$R(t) = \frac{g}{q\mu A}\left[\frac{eP_0\eta_{ext}\Delta t}{h\nu Ad}\frac{\sqrt{\pi}}{4\sqrt{\ln 2}}e^{-t/\tau}e^{\frac{-\Delta t^2}{\tau^2 16\ln 2}}\left\{erf\left(\frac{\frac{1}{\tau}\Delta t}{4\sqrt{\ln 2}}\right) - erf\left[\frac{\frac{1}{\tau}-\frac{8\ln 2}{\Delta t^2}t}{4\sqrt{\ln 2}}\Delta t\right]\right\} + n\right]^{-1}. \quad (2.4)$$

Fig. 2.3 illustrates variation of the resistance in a short carrier-lifetime (0.2 ps) PCA under 10 mW of 100 femtosecond laser exposure with respect to a THz pulse.

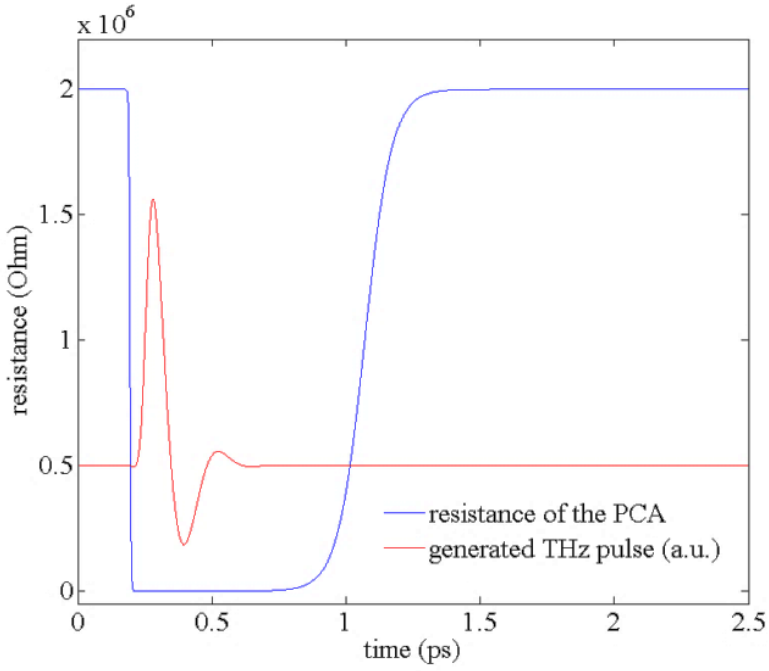

Figure 2.3 Numerically calculated resistance of a 0.2 ps carrier-lifetime PCA as function of time.

2.1.1.2. Transmitter

Fig. 2.4 shows a THz emitter under a femtosecond laser pulse. The optical pulse generates a large number of carriers inside the gap between arms of a dipole antenna. Electrons and holes diffuse with different velocities due to their different mobility. The process forms a charged dipole that radiates electromagnetic waves that extend to THz region. The electric field of the radiated THz beam E_{THz} is proportional to the derivative of the induced photocurrent *i(t)* inside the material

$$E(r,t) = \frac{l}{4\pi\varepsilon c^2 r}\frac{di(t)}{dt}\sin\theta, \tag{2.5}$$

where, L is the length of the dipole, θ is the deviation angle from the surface normal axis of the antenna, ε is dielectric constant of the medium and c is the speed of light in vacuum. Thus, strong THz radiation requires a large photocurrent at a sub-picosecond time. The current density in a very simple form is $j=\sigma E_{net} = -nqv$, where E_{net} is the net electric field that carriers feel and ν is the carrier velocity averaged over the carrier distribution. The conductivity is a function of carrier density n, mobility μ, and electron charge q. To maximize the THz radiation amplitude, both the number of generated carriers and the net field should be increased. In this case, the net electric field is defined by $E_{net}=E_{bias}-E_{scr}$, where E_{bias} is the DC field provided by the antenna electrodes and E_{scr} is the screening field that neutralizes the bias field when electrons and holes start to separate.

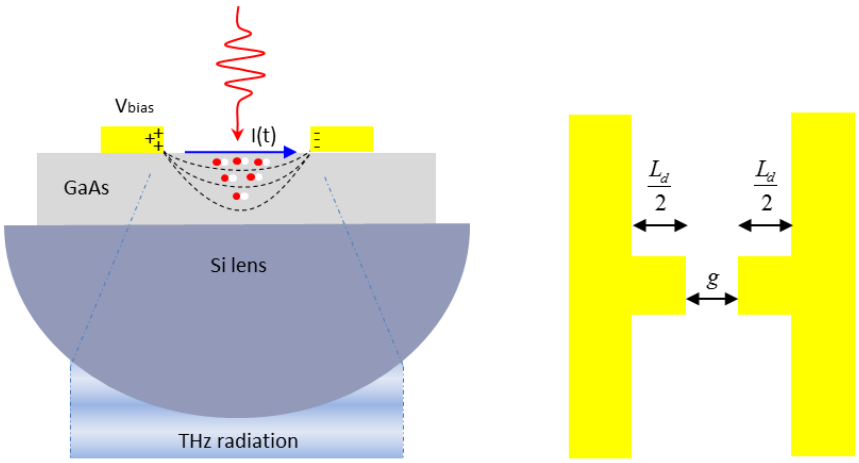

Figure 2.4 Left: off-scale side view presentation of a PCA on silicon lens. Right: geometrical shape of the dipole antenna with labels.

Because the radiated electric field is proportional to the time derivative of the photocurrent in the active area, we can rely on an analytical method explained by Jepsen *et al.* [31] to find the carrier transport of the photo-excited electrons. The equation of motion describing the average velocity is given by Drude-Lorentz model.

$$\frac{dv(t)}{dt} = -\frac{v(t)}{\tau_s} + \frac{q}{m^*} E_{net}, \tag{2.6}$$

where m* is the effective mass of the electrons and τ_s is the momentum relaxation time (~30 fs for GaAs). The E_{net} is known if the effect of screening is included. Here, the screening field is $E_{scr} = P_{sc}/\eta\varepsilon$ where P_{sc} is the space-charge polarization created by the carriers separating in the field for an isotropic dielectric material with permittivity ε and geometrical factor $\eta = 3$. The time dependence of the space-charge polarization is described by

$$\frac{dP_{sc}}{dt} = -\frac{P_{sc}}{\tau_r} + nqv, \tag{2.7}$$

where τ is the recombination lifetime. By taking the time derivative from equation (1.5) we can obtain a second-order differential equation for carrier velocity

$$\frac{d^2 v(t)}{dt^2} + \frac{1}{\tau_s}\frac{dv(t)}{dt} + \frac{\omega_p^2 v}{\eta} = -\frac{qP_{sc}}{m^* 3\varepsilon\tau}, \tag{2.8}$$

where $\omega_p^2 = nq^2 / m^* \varepsilon$ is the plasma frequency. Solving the coupled equations (2.7) and (2.8) with $j = -qnv$ and equation (2.1) predicts the THz pulse shape and the local electric field in the active area [31]. Jepsen *et al.* showed that the plasma frequency plays a crucial role in this model and basically indicates how screening affects the overshooting and the falling edge of the THz pulse for intense laser power $\omega_p \tau_s >> 1$. In other words, THz radiation occur when the total number of generated carriers is much larger than the number of carriers accumulated on the electrodes due to bias and the electric field due to separation of the electrons and holes overcome the external bias field e.g. (10^{18} ~ 10^{19} cm^{-3}). For extremely low laser power $\omega_p \tau_s << 1$, the screening field is much weaker than the bias field and the current is a linear function of applied field. Since few milliwatts of femtosecond laser power satiates the condition $\omega_p \tau_s >> 1$, THz emitters do not need to have a short carrier-lifetime. The photoconductive material of choice must have a high mobility because $v = \mu E_{bias}$ this is important to have a sharp overshoot and stronger THz radiation.

2.1.1.3. Receiver

Unlike transmitters, receivers are not externally biased and so the incident THz field moves the newly generated carriers inside the gap area. In fact, the THz field drives a weak but measurable DC current in the circuit. A lock-in amplifier detects the current and translates the signal for a computer where computational processes perform. An ideal receiver does not affect the shape of the electric field but in reality many factors are involved that can influence the signal waveform. Since the active area becomes conductive, the detector area has total length of $L=L_d+g$ and width of d, where L_d is the length of dipole arms and g is the length of the gap area. These geometrical values are important in defining sensitivity, response, and the bandwidth of the receiver.

Assuming that the incident electric field is composed of superposition of Gaussian beams with different frequencies, we can write the field equation of a single frequency component ω_i as

$$E(x,y) = E_o \exp\left[-(x^2+y^2)/\omega_i^2\right] \tag{2.9}$$

The current flowing across the active area is a function of coupled THz electric field and resistance of the gap. The gap resistance determines with the length g, width w, thickness of the photoconductive material d and its time-averaged resistivity ρ

$$R = \frac{\rho g}{wd}\,. \tag{2.10}$$

The resistivity ρ depends on the photo-excited carrier density that scales as

$$\rho = \frac{gw}{\xi P_o}, \tag{2.11}$$

with laser power to number of photo-excited carriers conversion ratio ξ. The average field over the electrodes is in direct relation to the potential difference across the active area. Thus the average current according to the Ohm's law is

$$I = \frac{E(L_d + g)}{R} = \frac{E(L_d + g)}{g^2} wd\xi P_o, \tag{2.12}$$

where L_d is the length of the dipole antenna. The electric field over the detector area is determined by

$$E(L,d) = \frac{1}{w}\int_{-L/2}^{L/2}\int_{-d/2}^{d/2} E(x,y)dxdy = \frac{E_o \pi \omega_i^2}{Lw} erf\left(\frac{L}{2\omega_i}\right) erf\left(\frac{w}{2\omega_i}\right). \tag{2.13}$$

The peak electric field amplitude is expressed as

$$E_o = \frac{2}{\omega_i}\sqrt{\frac{P_{THz}}{\pi c \varepsilon_o}}. \tag{2.14}$$

The frequency dependant average current at the detector can be re-written by inserting equation (2.14) into equation (2.12) and including the silicon lens parameters from [31]

$$I(f) = \xi P_o \sqrt{\frac{cP_{THz}}{\pi \varepsilon_o}} \frac{2R_L d}{g^2 w \omega_o (n_i - 1)} \frac{1}{f} \times erf\left[\frac{L}{2}\frac{\pi\omega_o(n_i-1)}{cR_L} f\right] erf\left[\frac{w}{2}\frac{\pi\omega_o(n_i-1)}{cR_L} f\right], \tag{2.15}$$

where f is the frequency, c is the speed of light in vacuum, R_L is the radius of the silicon lens with reflective index of n_i and initial THz beam spot size ω_o. The maximum of equation (2.12) is located approximately at the frequency

$$f_{\max} = \frac{cR_L}{\omega_o(n_i - 1)} \frac{1}{\sqrt{\pi d(L_d + g)}}. \tag{2.16}$$

It can be inferred that the current response of the detector is a function of the antenna dimensions. For a fixed size antenna, the current rises as frequency reaches f_{max} but it decays at high-frequency limit $f \to \infty$. Equation (2.16) shows that the maximum of the

current response shifts to higher frequencies as the size of the detector decreases, meaning that a high bandwidth dipole antenna must have a smaller size relative to its wavelength. Unluckily, less amount of incident electric field couples to the antenna when its size shrinks. In many works, dipole antennas with length of 20~30 μm and gap size of 5 μm show reasonable trade-off between current responsivity, amplitude, and bandwidth [1, 31-33].

In addition, the shape and the width of the optical pulse plays an important role in defining bandwidth of a THz-TDS system. A femtosecond Gaussian pulse with Δt pulse width has a bandwidth of $\Delta\nu=4.4/\Delta t$ [34]. For instance, a 100 femtosecond laser pulse results in an optimistically 4.4 THz of bandwidth. However, alignment, geometry of the antenna, material response, and external circuits raise the noise floor and reduce the bandwidth in real measurements. It is noteworthy to add that reducing the pulse width does not necessarily result in linearly increasing the bandwidth. An ultra-short pulse (<40 fs) has a wide Fourier spectrum and gives more energy required by electrons to overcome the band-gap, resulting in an increased effective mass (injection of electrons to the L valley) and lower mobility [35].

2.1.2. Frequency domain operation

As mentioned previously, conductivity of a photoconductive material increases under laser exposure. The resistance of the active area modulates with rate of oscillations when a variable intensity laser beam excites the PCA. Such variation is achievable by mixing two monochrome laser beams. Laser wavelengths are chosen such that the frequency offset or beating frequency falls in the range of THz region. If the photomixer is biased, the variable conductivity modulates the current that ultimately drives the antenna. This

process is photomixing and photomixer refers to any photoconductive device that uses continuous wave (CW) laser sources to generate continuous wave current with a terahertz frequency component.

Fig. 2.5 Shows a CW THz setup with fiber coupled photomixers. Detection in frequency domain operation is heterodyne because laser beams are shared between emitter and detector. On the receiver side, the output current is a product of the modulated conductance and the THz field. To obtain a wide THz spectrum, a step-by-step frequency tuning is required. The maximum tunable range or the bandwidth is determined by carrier lifetime and RC roll-off of the photomixers.

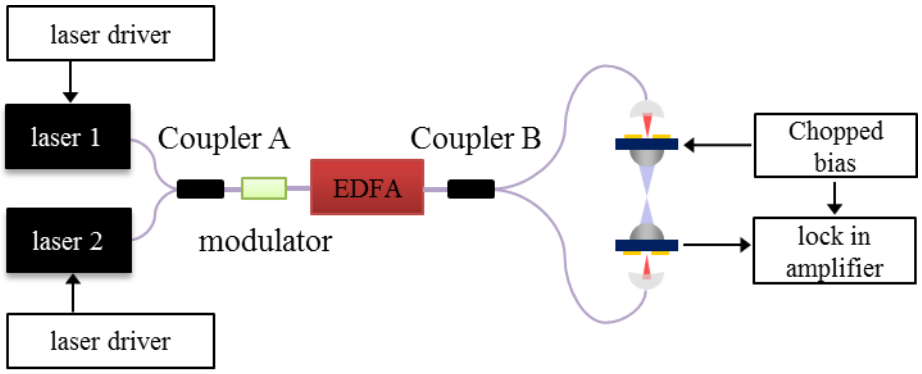

Figure 2.5 Frequency domain spectroscopy THz setup. EDFA is an erbium doped fiber amplifier. Modulator switches the optical beam with a short duty cycle pulses to avoid overheating.

2.1.2.1. Transmitter

For two laser beam co-propagating and co-linear in space with the same polarization angle, the total electric field is the superposition of their individual fields modulated at different frequencies. Here terms ω_1 and ω_2 are used to refer angular frequencies of two laser beams with powers P_1 and P_2. Thus, the combined instantaneous power on the surface of the photoconductive material is

$$P(\omega,t) = P_1 + P_2 + 2\sqrt{\eta_m P_1 P_2}\cos(\omega t)\ , \tag{2.17}$$

where $0 \le \eta_m \le 1$ is the matching parameter describing the quality of spatial overlap between two beams [36]. The time dependent carrier density of equation (2.1) is re-written as

$$\frac{dn(t)}{dt} = \frac{e\eta_{ext}}{h\nu Ad} P(\omega,t) - \frac{n(t)}{\tau} \ . \tag{2.18}$$

Substituting (2.17) to (2.18) and solving the differential equation for n(ω,t) gives

$$n(\omega,t) = \frac{\eta_{ext}(P_1+P_2)\tau}{h\nu Ad}\left[1+\frac{2\sqrt{\eta_m P_1 P_2}}{P_1+P_2}\right]\times\left[\frac{\omega\tau\sin(\omega t)+\cos(\omega t)}{1+(\omega\tau)^2}\right]. \tag{2.19}$$

The conductance of the active area under exposure is

$$G(\omega,t) \approx \frac{\sigma d\sqrt{A}}{w} = \frac{\mu q d\sqrt{A}}{w} n(\omega,t). \tag{2.20}$$

For photomixers the cut-off frequency is a dominant factor in defining the operational bandwidth. Thus, impedance of the active area is composed of the gap capacitance and its conductance *G(ω,t)*. Because input impedance of the antenna is in series with the impedance of the gap, the equivalent input impedance of the circuit as seen from the source is

$$Z(\omega,t) = R_A + \left[G(\omega,t) + j\omega C\right]^{-1}. \tag{2.21}$$

The instantaneous dissipated power in the antenna when a bias voltage of V_{bias} is applied to the photomixer is

$$P_{Antenna}(\omega,t) = R_A\left[\frac{V_{bias}}{Z(\omega,t)}\right]^2, \tag{2.22}$$

which can be re-written considering the fact that *RG<<1*,

$$P_{Antenna}(\omega,t)=\frac{R_A V_{bias}^2}{A}\left[\frac{\eta_{ext}\mu q\tau}{wh\nu}\right]^2\frac{1}{1+(\omega R_A C)^2}\times\left[P_1+P_2+\frac{2\sqrt{\eta_m P_1 P_2}}{1+(\omega\tau)^2}(\omega\tau\sin(\omega t)+\cos(\omega t))\right]^2. \quad (2.23)$$

By disregarding the average sinusoidal terms and the constant offset, the mean THz radiated power can be derived similar to calculations of Brown *et al.* [37]

$$P_{THz}(\omega)=2\frac{R_A V_{bias}^2}{A}\left[\frac{\eta_{ext}\mu q\tau}{wh\nu}\right]^2\frac{\eta_m P_1 P_2}{\left[1+(\omega\tau)^2\right]\left[1+(\omega R_A C)^2\right]}. \quad (2.24)$$

The first conclusion from equation (2.24) is the high-frequency limit $P_{THz}(\omega)\propto\omega^{-4}$, and hence a roll-off of -12 dB per octave is expected. For a photomixer with a sub-picosecond carrier life-time, gap capacitance of 1~5 fF and resistance of few kΩ, the roll-off starts immediately after 1 THz [36].

Verghese *et al.* have studied roll-off for 20 × 20 μm and 8 × 8 μm size active area photomixers [38]. In their experiment a log-spiral antenna with an interdigitated gap structure was used because its radiation pattern and input impedance is constant over the tuning range. For the smaller gap size photomixer, the input impedance of the log-spiral antenna $R_i=60\pi/\sqrt{\varepsilon_{eff}}=72\Omega$ yields a 200 fs RC time constant that is close to typical carrier-lifetime of LT-GaAs. The photomixer with smaller size (8 × 8 μm) showed a higher bandwidth (roll-off about 1.2 THz) due to smaller gap capacitance, which is also in agreement with experimental results reported Gregory *et al.* [36].

One important challenge in designing photomixers is heat dissipation. A typical way to cope with the overheating is to give a long rest time to the material after intense laser exposure. High intensity optical pulses at a short duty cycle (quasi-CW) can also help

with reducing the gap resistance at the time that the gap and the antenna impedances must match. A very recent study claims an instantaneous 0.8 mW of radiation power at 1 THz under 150 mW of optical power with duty cycle of 2% [39].

There are also other approaches with the goal of enhancing the output power. One successful method is modified semiconductor heterostructures such as p-i-n photodiodes. The design contains an i-region InP layer with exceptionally high mobility where electrons diffuse and accelerate between a p-type InGaAs absorption layer and an n-type contact semiconductor. The device is called Uni-Traveling-Carrier (UTC) diode. An output power of 10.9 μW at 1.04 THz has been reported from a UTC diode connected to a resonating antenna [40].

2.1.2.2. Receiver

Bolometers are the most common detector for output power characterization of the photomixers, but they are bulky and they need cryogenic cooling. Theoretically, another photomixer must be able to down-convert the THz signal with the same combination of optical beams. In a simplified form, the current appeared on electrodes of the detector is calculated from Ohms' law if we assume that both the incident THz wave and the conductance of the gap have a sinusoidal modulation scheme at THz angular frequency ω,

$$I(\omega,t) = V(\omega,t)G(\omega,t) = V_o \cos(\omega t + \phi) G_o \cos(\omega t) = \frac{1}{2} I_o \left[\cos(\phi) + \cos(\phi + 2\omega t)\right] \quad (2.25)$$

where ϕ is the phase of the THz wave. Here, the cosine term containing $2\omega t$ disappears and the DC current is measurable by an external ammeter e.g. lock-in-amplifier.

The advantage of frequency domain operation is the lower laser components cost in comparison with the femtosecond lasers. In addition, the power can be easily amplified

without any concerns of dispersion or pulse broadening. However, additional components increase complexity of a complete system and challenges such as heat dissipation, impedance matching, slower and limited tuning range of the lasers always question credibility of this method over time domain operation.

2.1.3. Optical rectification

Optical rectification is a non-linear process when an intense optical pulse forces electrons of a noncentrosymmetric medium to oscillate. Because of an asymmetric electron charge distribution inside the medium, the oscillation cannot be symmetric. This will give rise to an asymmetric electric field that fits in the envelope of the optical pulse. In the case of a femtosecond excitation, a THz pulse is generated along with the propagation of the laser beam. Thus, phase velocity of the THz wave and group velocity of the laser pulse must match for a constructive conversion.

Despite the simple alignment and lower noise, THz generation using optical rectification is limited by the properties of the crystals such as electro-optical coefficient, transparency and refractive indexes at optical and THz regions. For each crystal, the term "coherence length" defines the maximum thickness that two waves (optical and THz) are constructively interacting. Equation (2.26) shows how coherence length is dependent on the refractive indexes of the nonlinear material in the THz (n_T) and optical (n_o) regimes

$$l_c = \frac{\pi}{\Delta k} = \frac{c}{2 f_{THz}(n_T - n_o)}, \tag{2.26}$$

where f_{THz} is the THz frequency [1]. The crystal must be transparent for both THz and optical frequencies. Among the zincblende crystals, ZnTe is the most popular crystal for 800 nm excitation because of its transparency in both regimes. Nahata *et al.* [41] first reported THz generation and detection with a pair of (110) orientation ZnTe crystals with

up to 3 THz of bandwidth. It was understood that the thickness must be reduced to gain bandwidth at the cost of THz amplitude. With this approach, Han *et al.* [42] reported bandwidth of 17 THz that was only limited to absorption caused by the crystal's lattice vibrations, also known as phonon absorption e.g. 5.3 THz for ZnTe. But ZnTe was not the only crystal used for optical rectification. GaSe is a promising semiconductor with a large nonlinear electro-optical coefficient (54 pm/V) that has been exploited recently for THz generation. Another work claimed 41 THz of bandwidth from GaSe [43]. Crystals such as LiTaO3 and LiNbO3 have a large electro-optical coefficient that is very useful for nonlinear application. Unluckily, they are opaque in the THz region (Fig. 2.6) and it is difficult to extract THz from the crystal owing to total internal reflection. In 1980, Auston reported 5 THz of bandwidth achieved by femtosecond excitation of LiTaO3 [44, 45]. Recently, organic electro-optic crystals with extraordinary large second-order nonlinear electric susceptibility have become interesting sources of THz. Zhang *et al.* first used an organic crystal, dimethyl amino DAST, with an electro-optical coefficient of >400 pm/V [46]. In this work, 180 mW optical pump beam was focused to a 200 μm diameter spot, resulting in 15 times stronger THz signal in comparison with LiTaO3 and 42 times larger than GaAs under same experimental conditions.

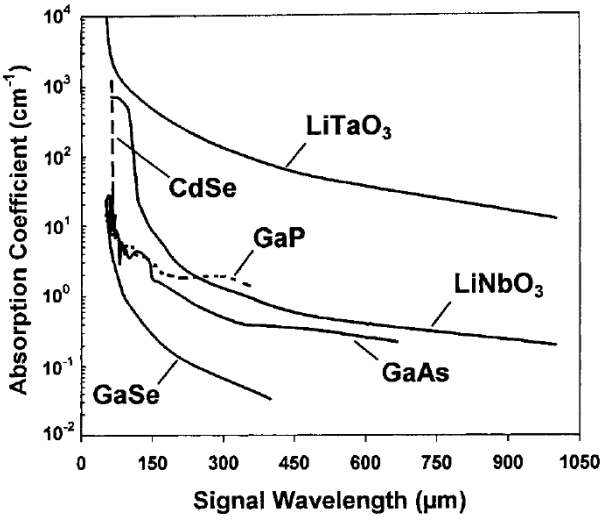

Figure 2.6 THz absorption spectra of popular nonlinear crystals, CdSe, LiNbO3, GaSe, LiTaO3, and GaAs [47].

2.1.3.1. Electro-optical sampling

THz detection using nonlinear crystals relies on birefringence and utilizes the Pockels effect. Fig. 2.7 shows a time domain THz electro-optical sampler. The setup comprises a nonlinear crystal followed by a quarter wave plate that makes circularly polarized light in the absence of the THz field. If both the THz field and the probe beam co-propagate inside the crystal, the E field of the THz wave rotates polarization of the probe beam resulting is an elliptically polarized beam. A Wollaston beam splitter and a differential photodetector can detect small changes between vertical and horizontal polarisation components. A delay line changes the time-space position of the THz beam similar to the THz-TDS using PCAs and the electro-optical sampler plots a time varying signal.

GaAs is a low cost semiconductor that is transparent in both the THz and telecom windows. It possess the longest coherent length at 1550 nm wavelength among all nonlinear crystals with a phonon absorption band located at 8.1 THz [1]. The main

weakness of GaAs is its small electro-optical coefficient (1.5 pm/V) [48]. Yet, in a scheme proposed by Nahata *et al.* electro-optic detection of continuous-wave terahertz radiation using GaAs was studied and considered feasible [49].

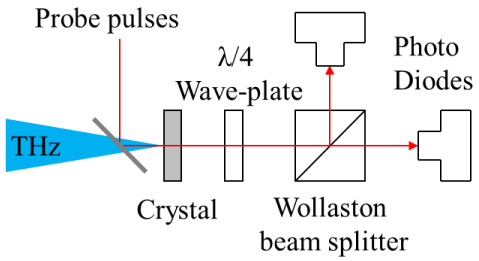

Figure 2.7 THz electro-optical sampling using nonlinear crystals.

Regardless of all efforts to push the optical rectification technology to the 1550 nm window and obtain stronger signal, the THz wave generates inside the crystal. Thus, it is challenging to launch waves into waveguides. Unlike photoconductive antennas with virtually unlimited development capacity, there is an optical to THz conversion efficiency (10^{-9} ~ 10^{-6}) associated with properties of the crystals [33] and heat defines a limit in illumination intensity. Hence, in this thesis, we didn't investigate THz generation and detection based on nonlinear crystals.

2.1.4. Thermal detectors

Thermal detectors are usually made from a radiation absorber material that converts the radiation energy into heat. A Golay cell is a type of thermal detector with a gas-filled enclosure that expands as the temperature increases. The displacement translates into voltage on the output with a noise equivalent power of 10^{-9} ($W/Hz^{1/2}$), which is close to the sensitivity of PCAs. They can be used to characterize output power of the THz transmitters but due to their lower sensitivity, their application is limited to high power emitters.

Bolometers are much more sensitive thermal detectors that operate at a few degrees Kelvin above absolute zero in vacuum. The noise equivalent power of the bolometer is in range of 10^{-19} (W/Hz$^{1/2}$). Bolometers are commonly used power detectors in pulsed and continuous wave THz systems but they are big, expensive and slow [36, 39, 50-52]. Therefore, application of thermal detectors has been limited to laboratories.

2.2. THz optics

THz waves are electromagnetic waves and their properties can be described by Maxwell's equations. Here, basic electromagnetic theory of dipole radiation is briefly covered. Then, important factors in selecting an antenna for THz devices will be discussed. The last part of this section explains properties and types of silicon lenses in THz alignment.

2.2.1. Electric dipole radiation

THz radiation is generated by accelerating charges in a time varying current, which by definition is an oscillating electric dipole. In a spherical coordinate system (r,θ,φ), electric E and magnetic H field equations of a vertically oriented short dipole antenna (length $L << \lambda$ wavelength) can be approximated for far-field by

$$E(r,\theta) \cong j\eta \frac{kI_o L e^{-jkr}}{4\pi r} \sin\theta, \tag{2.27}$$

$$H(r,\varphi) \cong \frac{E(r,\theta)}{\eta} = j\frac{kI_o L e^{-jkr}}{4\pi r} \sin\theta, \tag{2.28}$$

where $\eta = 120\pi$ is free space intrinsic impedance, k is the propagation constant $k = 2\pi/\lambda$ and I_o is a constant current parameter [53]. The radiation resistance R_r of a small dipole antenna is

$$R_r = \eta \frac{2\pi}{3}\left(\frac{L}{\lambda}\right)^2. \tag{2.29}$$

It is interesting to note that the field amplitude escalates as the length of the antenna increases when the condition $L << \lambda$ is recognized [32, 53]. Also, the field amplitude is dependent on the deviation angle θ from the orientation of the dipole. In other word, it is important to know whether the radiated beam is directed to the receiver. Directivity measures the total radiation intensity in the direction of the strongest emission opposed to an isotropic radiation (uniform emission in all directions). Directivity of maximum radiation intensity by definition is expressed as

$$D_{\max} = \frac{4\pi U_{\max}}{P_{rad}}, \tag{2.30}$$

where $U_{\max}$ is the maximum radiation intensity per solid angle and P_{rad} is the total radiation power. This ratio is 1.5 for a small dipole antenna [53]. When the size of the antenna increases, a complex form of equations must be used. The electric and magnetic field equation of an arbitrary length dipole are [53]

$$E(r,\theta) \cong j\eta \frac{I_o e^{-jkr}}{2\pi r}\left[\frac{\cos(\frac{kL}{2}\cos\theta) - \cos(\frac{kL}{2})}{\sin\theta}\right], \tag{2.31}$$

$$H(r,\varphi) \cong j\frac{I_o e^{-jkr}}{2\pi r}\left[\frac{\cos(\frac{kL}{2}\cos\theta) - \cos(\frac{kL}{2})}{\sin\theta}\right]. \tag{2.32}$$

Input impedance of an antenna is the ratio of the voltage to current measured at the terminals. The real part of the input impedance is considered as input resistance R_i, which for a lossless antenna reduces to the radiation resistance R_r. Here, a longer antenna

does not necessary increase the field amplitude at the location of the receiver in far-field. Similarly, directivity of the antenna changes as the length increases. Fig. 2.8 shows how input resistance and directivity changes as the length of the antenna increases per wavelength. Therefore, it is better to use a short antenna (10 ~ 30 micrometers) to ensure that the radiation pattern is uniform even for high frequency components.

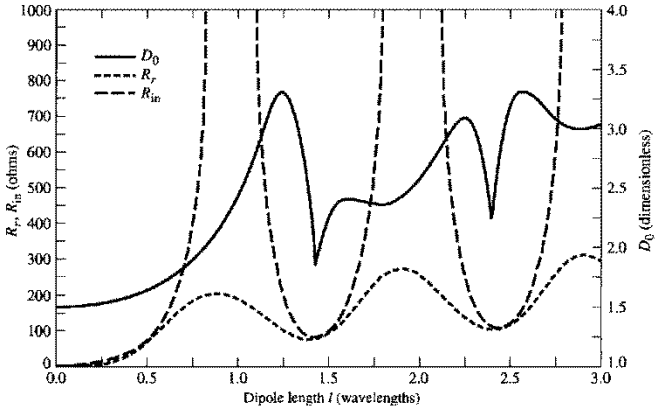

Figure 2.8 Input resistance Ri, radiation resistance Rr and directivity of the main lobe D_o of an arbitrary length dipole antenna with sinusoidal current [53].

2.2.2. Antennas for THz photoconductive switches

Antennas are key elements of PCAs. They have two crucial tasks. First, they radiate the THz current generated inside the gap. Second, they provide bias to drive the active area. The antenna is usually made of Gold because it has superior electrical and thermal conductivity and it does not oxidize. Fig. 2.9 shows typical THz antennas. Applications of these antennas vary depending on the operation mode. Dipole and bowtie antennas are used in THz-TDS whereas spiral antennas are common in THz-FDS.

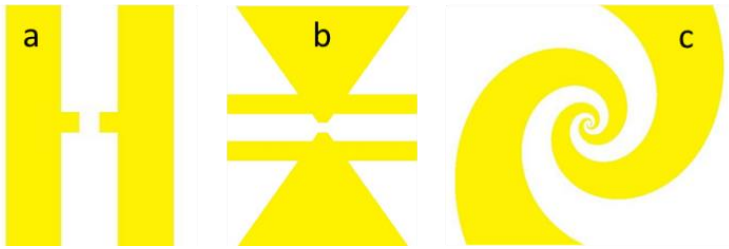

Figure 2.9 Three common THz antennas. (a) a dipole antenna. (b) centre-fed bowtie antenna. (c) log-spiral antenna.

It is noteworthy to mention that maximum power transmission to the load (antenna) is possible if the impedance of the active area is matched to the input impedance of the antenna. Impedance matching is not similar in time domain and frequency domain operation modes.

In a continuous laser excitation THz-FDS, impedance of the active area is in the range of kΩ. Thus, it is necessary to have an antenna with higher input impedance. As mentioned earlier, logarithmic antennas are preferred in photomixers because they have a flat input impedance over their entire tuning range. However, this is at the cost of a lower input impedance, compared to a typical dipole antenna, the log-spiral antenna has a relatively lower output power because of its low radiation resistance e.g. a 50 μm long dipole antenna with 5 × 5 μm gap size has peak 360 Ω of radiation resistance at resonant frequency of 1.8 THz [54]. With the aim of having a higher radiation resistance and broader tuning range, research was conducted on CW THz antenna shape. The best example is a dual dipole antenna with inductive loads to cancel out the gap capacitance. This dual antenna was designed by Duffy *et al.* and showed superior output power of 2, 0.8, and 0.3 μW at 1.0, 1.6, and 2.7 THz, respectively [55].

In a THz-TDS the radiation mechanism is different. Resistance of the gap area is driven too low (<1Ω) under femtosecond optical pulse and the THz photocurrent is not sinusoidal. The surge current initiates the electric field, which then couples to the antenna. So, the shape of the antenna has a stronger impact on the THz signal.

A research by Tani *et al.* showed that the bowtie antenna generates much higher THz field amplitude but most of the power radiates at lower frequencies [32]. In that work, multiple dipole antennas with different lengths were tested with the conclusion that a 30 μm long antenna results in maximum radiation amplitude with no loss of high frequency components up to 3 THz. Therefore, small dipole antennas are better candidates for high bandwidth THz-TDS. We used similar dipole antennas in this research to obtain maximum bandwidth and to be consistent with dipoles of the commercial PCAs for an "apples-to-apples" comparison.

2.2.3. THz beam shaping and steering

Since the generated THz field is very weak, it cannot be picked up by the detector if we rely on directivity of the dipole itself [56]. Usually, the power radiated into the photoconductive material is larger than into air by a factor of the substrate dielectric constant e.g. $\varepsilon_r = 12.9$ in GaAs. Thus, just like a parabolic antenna that collimates the microwave radiation, it is expected from a silicon lens attached to the back side of a PCA to absorb and direct the THz wave to a line of sight receiver [31]. These lenses are made of highly resistive silicon to be matched with the refractive index of most PCA substrates. Besides, silicon is almost transparent at THz frequencies and its dispersion is negligible.

There are two types of lenses, aspheric focusing lens and hyper-hemispherical lens. While focusing lenses are better for a line-of-sight alignment, hyper-hemispherical lenses

are popular for beam shaping applications that external parabolic mirrors or Teflon lenses are used. In this section, we label the emission angle ϕ, the internal reflection angle θ, and the distance between the focal point and the tip of the lens d to reach a simple general relation [31]

$$(d - R_L)\sin\phi = R_L \sin\theta, \tag{2.33}$$

where R_L is the radius of the silicon lens as seen in Fig. 2.10. The distance between the tip of the silicon lens and the focal point (position of the dipole) is expressed as

$$f_{focus} = R_L(1 + \frac{1}{n-1}), \tag{2.34}$$

$$f_{hyper} = R_L(1 + \frac{1}{n}), \tag{2.35}$$

where n is the refractive index of the lens.

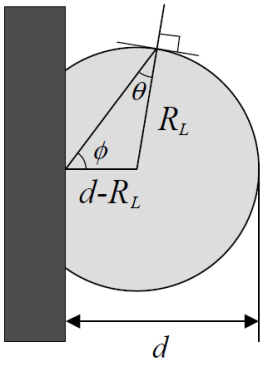

Figure 2.10 Silicon lenses. RL is the radius of the lens, d is the distance between the focal point and the tip of the lens, ϕ is the emission angle, μ is the internal incidence angle, and n is the refractive index of the lens.

The size of the beam at the focal point is a function of the beam profile. Assuming a Gaussian beam profile for THz waves incident of a focusing lens with initial beam waist w_0, the size of the beam at focal point is [31]

$$w_1 = \frac{\lambda_{THz}}{\pi w_o}\frac{R_L}{n-1}. \tag{2.36}$$

This indicates that the THz spot size at focus on the dipole is proportional to wavelength λ_{THz}. Therefore, it is more challenging to get high frequency components during the alignment. To get an optimum focus for all frequency components, the distance between transmitter and receiver must be determined. The initial position of the beam waist from the tip of the focusing silicon lens is usually given by datasheet of the lens e.g. it is 53 mm for the 6 mm radius focusing lenses that were used in this thesis.

Fig. 2.11 shows CST Microwave Studio simulation results for radiation pattern, directivity and angular width (divergence angle) of the THz beam from a PCA mounted on a 5 mm diameter silicon lens at far-field. It is evident that the radiation pattern is dependent on frequency and the divergence angle decreases as the frequency increases as expected.

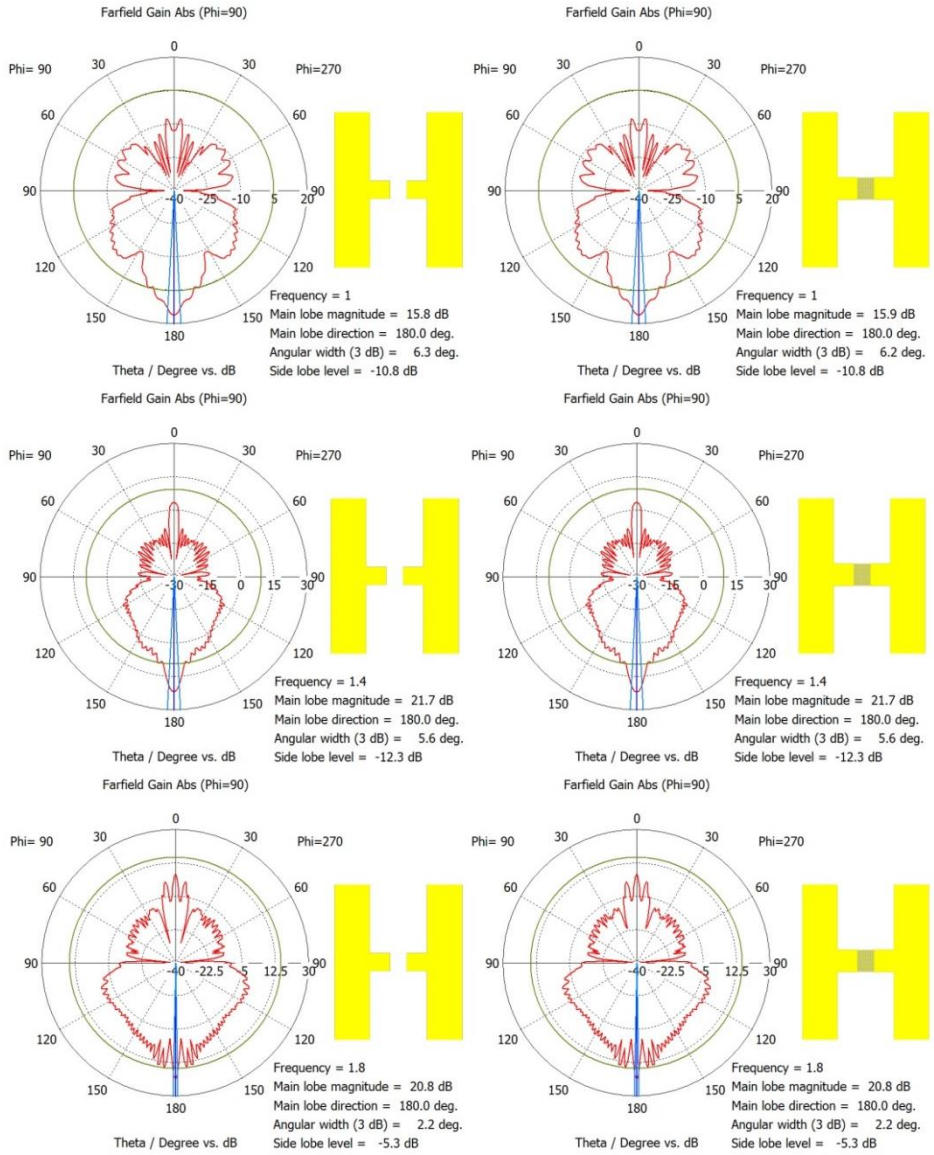

Figure 2.11 Simulated directivity of the photoconductive antennas mounted on silicon lens for a large gap (left) and a gap composed of nanostructures (right). The frequency was swept from 1 to 1.8 THz.

2.3. Recent studies on photoconductive materials

As mentioned earlier, material plays a definitive role in the performance of THz photoconductive antennas. An optimum material for photoconductive THz generation and detection must possess a high mobility, short carrier lifetime (sub-picosecond), high breakdown voltage and high electron saturation velocity. In addition, it must have a low conductance in the absence of light. Many III-V semiconductors such as GaAs, GaP, GaSb, InP, InGaAs, InGaAs, and InAs have been implemented in THz devices [57]. Some have also reported photoconductivity from carbon nanotubes and PbS [58-60], which may find applications in THz industry. Below is a brief description of advantages and disadvantages of most studied photoconductive materials. Since the goal of this thesis is to push the THz-TDS to the telecom window, we finally discuss methods and evaluate candidate materials for implementation in PCAs at 1570 nm excitation.

2.3.1. GaAs

Undoubtedly, GaAs is the most popular photoconductive material in THz industry. GaAs is a compound of III-V group materials with a direct bandgap in a zinc blende crystal structure. Properties of GaAs at 300 degree of Kelvin can be summarized below [61]

- Dielectric constant (static): 12.9
- Effective electron mass: 0.063 m_e
- Energy gap: 1.424 eV
- Intrinsic resistivity: $3.3\times10^{8}\ \Omega\cdot cm$
- Intrinsic carrier concentration: $2.1\times10^{6}\ cm^{-3}$
- Effective conduction band density of states: $4.7\times10^{17}\ cm^{-3}$
- The longest lifetime of holes: 3×10^{-6} s

- The longest lifetime of electrons: 5×10^{-9} s
- Voltage breakdown field: 4×10^{5} V/cm
- Electron saturation velocity: 1.27×10^{5} m/s
- Mobility electrons: $\leq$8500 $cm^2\ V^{-1}s^{-1}$
- Mobility holes: $\leq$400 $cm^2\ V^{-1}s^{-1}$
- Thermal conductivity: 0.55 W cm^{-1} °C $^{-1}$
- Infrared refractive index: 3.29
- Long-wave TO phonon resonance: 8.1 THz
- Long-wave LO phonon resonance: 8.72 THz

THz radiation was first observed from the surface of semi-insulating (SI) GaAs under 840 nm femtosecond laser excitation in 1991 [62]. Since then, numerous works have been published on applications and advantages of this material in terahertz generation and detection. The most important feature of GaAs is its large bandgap energy that make the semiconductor very resistive at the absence of light but its carrier lifetime is long. The low dark conductivity of GaAs allows below thermal breakdown operation of the emitter PCA at high bias voltages i.e. electric field as high as 40 MV/m. A large gap GaAs based receiver has a lower Johnson-Nyquist noise that is essential for obtaining a wide dynamic range [33, 63]. Hale and co-workers have reported up to 20 THz of bandwidth using a simple semi-insulating GaAs in a THz-TDS setup with 15 fs optical pulse excitation [64]. Nevertheless, receivers require a short carrier lifetime to ensure maximum bandwidth.

In order to reduce the carrier-lifetime a few attempts have been made such as ion implantation [65-67] but results are not impressive [68]. The remarkable feature of GaAs is that it can be grown at lower temperatures (200 ~ 350 ^{o}C), resulting in a material

known as LT-GaAs. At lower temperatures, more Arsenic is incorporated into the growth process, which forms defect states. Arsenic defect states reduce the carrier lifetime [69-77]. In a study by Tani *et al.,* detection response of semi-insulating GaAs is compared with that of a LT-GaAs based receiver [78]. They concluded that the SI-GaAs-based detector has a responsivity comparable to LT-GaAs only at very weak laser power. But, the signal to noise ratio of SI-GaAs based detector was severely weaker than LT-GaAs PCA as a result of background noise originating from a huge amount of stray photo-excited carriers. In the meantime, a carrier-lifetime as low as 100 fs has been achieved with annealing of LT-GaAs [79] and a bandwidth up to 60 THz has been reported using photoconductive antennas based on LT-GaAs [80].

The excess Arsenic defects cause a localized energy state inside the GaAs bandgap, which is known as the EL_2 defect [70, 81]. Arsenic defect densities are typically in range of 5×10^{18} - 6×10^{20} cm^{-3} [69, 82]. The bandgap energy associated with Arsenic defects are distributed in range of 0.08 to 0.85 eV below the conduction band with maximum probability at 0.71 eV [72, 73, 83]. The Fermi level in LT-GaAs is pinned to the mid-gap due to the high density of EL_2 defect states. Annealing can significantly alter the performance of the LT-GaAs [36, 84]. defects begin to move and merge as the annealing temperature and time increases, causing formation of metallic Arsenic clusters [76, 85]. Clusters have lower concentration and larger capture cross section for electrons inside the lattice, which induce stronger trapping sites for bypassing electrons to the valance band in a non-radiative recombination process [75]. It is important to note that although the carrier-lifetime can be reduced below 100 fs [86], a trade-off is always required. Since an

ultra-short carrier lifetime kills carriers before they contribute to the photocurrent, THz amplitude may be sacrificed for a wider bandwidth [36].

LT-GaAs is a unique material, which features inexpensive fabrication cost, controllable carrier lifetime, and low conductivity with mid-gap defect states. In 1996, Dankowski *et al.* showed that the absorption of LT-GaAs outreaches the telecom window [81] and it decays by annealing. In theory, a 1.55 μm photon delivers 0.78 eV energy to the electrons of the valance band to jump to the mid-gap states. In an intense exposure case, electrons are kicked out of the mid-gap states with enough energy to reach the conduction band [87]. Fig. 2.12 clarifies this two-step process, which is strongly dependent on the intensity of the light [88]. The absorption coefficient of LT-GaAs at 1.55 μm is about 1200 cm^{-1} [81], which is 7 times lower than the absorption at bandgap edge of SI-GaAs [89]. Nevertheless, a weak but measurable photocurrent is generated if the gap area of a biased LT-GaAs based PCA is exposed to 1570 nm laser illumination.

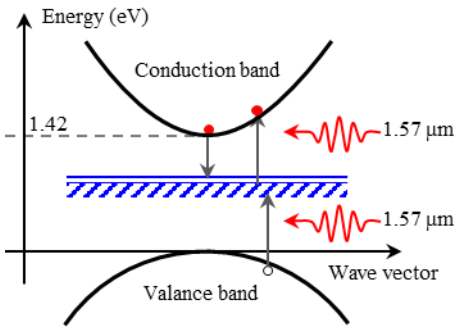

Figure 2.12 Two-step 1.55 μm photon absorption process enabled by mid-gap states in LT-GaAs.

2.3.2. GaAsBi

Bismuth, the heaviest group V semi-metal, is an element that incorporates along with Arsenic in the GaAs lattice during the growth process. GaAsBi has unique features. It has been shown that even a few percent of Bi shrinks the bandgap of GaAs by making shallow localized states near the valance band [90]. Fabrication of GaAsBi is at higher temperatures (300 - 350 C). Thus, mobility of the material is usually higher than LT-GaAs i.e. electron mobility of >2300 $cm^2V^{-1}s^{-1}$, as compared to 500 $cm^2V^{-1}s^{-1}$ for LT-GaAs. Unfortunately, annealing for GaAsBi with the aim of reducing the carrier lifetime is not as effective as the case of LT-GaAs because the material is not grown at low temperature. In addition, Bismuth is a bigger defect than Arsenic and its movement due annealing produces much damage to the structure of the lattice [91]. It has been reported that a carrier lifetime of a few picoseconds can be achieved with a proper and accurate annealing [92]. Nevertheless, annealed GaAsBi devices have shown much lower dark current and higher photocurrent than LT-GaAs under 800 nm excitation [93].

In order to find electro-optical properties of GaAsBi one can use a photoluminescence (PL) measurements method that uses a high photon energy beam to excite the electrons and looks at the reflected wavelengths induced by recombination of carriers. The higher the percentage of Bi concentration is, the more the PL peak shifts into infrared (~80 meV/1% [94]). About 14% of Bi is required to obtain a bandgap of nearly 0.7 eV i.e. an engineered GaAs based material for 1550 nm. Unfortunately, the excess Bi percentage increases the conductivity of the film to few $\Omega \cdot cm$, which is not suitable for PCAs. An attempt for making a photoconductive antenna with 14% Bi was made at the University of Victoria THz laboratory, but the PCA failed at 1 V_{DC} bias due to the excess heat generated inside the photoconductive material.

2.3.3. InAs

Among semiconductors, InAs may exhibit some features that may look very tempting for photoconductive THz generation. Indium arsenide is a direct bandgap semiconductor with zinc blende crystal structure that has found many applications ranging from infrared detectors 1-3.8 μm and diode lasers to FET transistors. Below is a list of InAs properties at room temperature

- Dielectric constant (static): 15.15
- Effective electron mass: $0.023m_e$
- Energy gap: 0.354 eV
- Intrinsic resistivity: 0.16 Ω·cm
- Intrinsic carrier concentration: 10^{15} cm^{-3}
- Effective conduction band density of states: 8.7×10^{16} cm^{-3}
- Breakdown field: 4×10^{4} $V\cdot cm^{-1}$
- Mobility of electrons: ≤ 40000 cm^2 $V^{-1}s^{-1}$
- Mobility of holes: ≤ 500 cm^2 $V^{-1}s^{-1}$
- The longest lifetime of holes: 3×10^{-6} s
- The longest lifetime of electrons: $3\cdot10^{-8}$ s
- Infrared refractive index: 3.51
- Thermal conductivity: 0.27 W cm^{-1} °C $^{-1}$

InAs has almost all features suitable for the 1.55 μm window. It has been reported that p-type InAs can generate an order of magnitude stronger THz than GaAs and InP [95], but not in the form of a conventional PCA THz emitter. InAs is very conductive at room temperature (intrinsic resistivity of InAs is 0.16 Ω·cm). Thus, THz generation is only possible by surface exposure and carrier diffusion that relies on the Photo-Dember effect

[95, 96]. In the literature, enhancement has been achieved by applying a surface parallel magnetic field. The best example is by J. N. Heyman *et al.* who reported 12 μW of THz generated power from an n-type InAs in a 3.2 Tesla magnetic field [97]. Yet, the extra spacing and weight required for the setup weakens the chance of any application in future portable THz-TDS systems.

2.3.4. InGaAs

InGaAs is the most popular material in the telecom industry for application such as photodetectors 1.1-1.7 μm and HEMT transistors. The energy bandgap of $Ga_{0.47}In_{0.53}As$ is 0.74eV (corresponding to 1680 nm) and it is less conductive than GaSb, InAs, and InSb. Thus, InGaAs can potentially shift the THz generation to the telecom window. InGaAs is normally grown on InP substrates. Properties of the InP lattice matched $Ga_{0.47}In_{0.53}As$ at 300 degree of Kelvin are

- Dielectric constant (static): 13.9
- Effective electron mass: 0.041 m_e
- Energy gap: 0.74 eV
- Intrinsic resistivity: 8.16×10^{2} Ω·cm
- Intrinsic carrier concentration: 6.3×10^{11} cm^{-3}
- Effective conduction band density of states: 2.1×10^{17} cm^{-3}
- The longest lifetime of holes: 10 s
- Voltage breakdown field: 2×10^{5} V/cm
- Mobility electrons: ≤12000 cm^2 $V^{-1}s^{-1}$
- Mobility holes: ≤300 cm^2 $V^{-1}s^{-1}$
- Thermal conductivity: 0.05 W cm^{-1} °C^{-1}

- Infrared refractive index: 3.43

Similar to LT-GaAs, Arsenic defect states are produced during low temperature growth of InGaAs. However, defects move closer to the conduction band due to the presence of Indium content [98]. This results in an activation energy of 32 meV at room temperature and energy of band-gap state levels only at 150 meV below the conduction band as explained by Grandidier *et al.* [99]. Because Arsenic defect states are closer to the conduction band in $In_{0.53}Ga_{0.47}As$, the material exhibits high carrier concentration (10^{17} - 10^{18} cm^{-3}), at room temperature [100]. Maintaining the crystalline structure of the InGaAs lattice at elevated temperatures (annealing) is a real challenge. Thus, it is difficult to obtain a short carrier lifetime and low conductivity InGaAs after a low temperature growth process. Several methods have been used to overcome this challenge. Among those Fe-implantation [101, 102], erbium super-lattice integrated ErAs:InGaAs [103, 104], and Beryllium p-type doping [105, 106] have been extensively investigated.

The Fraunhofer Institute of Technology has recently developed multi-quantum-well InGaAs/InAlAs heterostructures [107]. Carriers are trapped in isolating InAlAs layers resulting in sub-picosecond carrier lifetime and low conductivity [108, 109]. Further modifications have been applied by etching-out a MESA structure [110], which results in lower dark current and a uniform electric field distribution between electrodes. Transmitters built on this material have achieved 5 μW of radiation power [111]. Nevertheless, the design complexity and fabrication processes increase the price of each PCA.

2.4. Enhancement of optical coupling using plasmonic nanostructures

Photon absorption is the first and vital step in generation and detection of THz modulated currents. It is expected to see a stronger THz signal if more light couples to the photoconductive material. But for standard large gap dipole PCAs, the active area is a bare interface of air and semiconductor. Most materials such as GaAs, InGaAs have relatively higher permittivity than air. Thus, they reflect a significant amount of light due to refractive index mismatch e.g. 28% for GaAs. A classical way to avoid reflection loss is to fabricate an anti-reflection coating layer on top of the semiconductor [1]. But, it is also important to consider that only carriers generated in 200 nm distance of the electrodes can participate to photocurrent in a sub-picosecond time. The rest of the carriers either recombine or feel a weak bias field to accelerate. In fact, intensity of light should be maximized in a minimum depth of the photoconductive material for an optimum performance. Therefore, we consider plasmonic structures to enhance optical coupling to the material.

2.4.1. Surface plasmons

In 1957, Ritchie predicted a special interaction between light and metal that can excite electron waves at the interface of dielectric and metal [112]. Here, the energy of the light is shared between the propagating electron charge density of the metal (plasmon) and the electromagnetic wave in the dielectric (photon). The coupling between a surface plasmon and a photon is called surface plasmon polariton [1]. Fig. 2.13 shows surface plasmon wave at the interface of Gold and air. The most interesting feature of surface plasmons is that the field is maximum at the interface of metal and dielectric and it decay exponentially in two medias. Note that the surface plasmon wave is transverse magnetic (TM) mode wave propagating along the interface with propagation constant of

$$k_x = k_0 \sqrt{\frac{\varepsilon_m \varepsilon_d}{(\varepsilon_m + \varepsilon_d)}}, \tag{2.37}$$

where k_0 is the free space wave-vector, ε_m and ε_d are the dielectric constants. Surface plasmon resonance occurs when plasmon waves are confined between boundaries and oscillate with the frequency of the excitation beam. Surface plasmon oscillations allow extraordinary light confinement, transmission and manipulation at small scales. Using Drude fit, the frequency of the surface plasmon wave, where the propagation constant approaches infinity can be found as

$$\omega_{sp} = \frac{\omega_p}{\sqrt{1+\varepsilon_m}}, \tag{2.38}$$

where $\omega_p = \sqrt{Ne^2/\varepsilon_0 m^*}$ is the bulk plasma frequency of metal with charge density *N* and the carrier effective mass *m** (*e* and ε_0 are charge and vacuum permittivity constants). The wavelength associated to surface plasmon resonances is dependent on refractive indices and it is smaller than the wavelength of the incident wave in free space [113, 114].

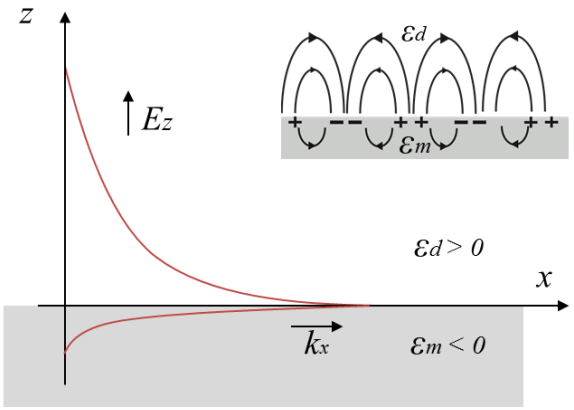

Figure 2.13 Exponential electric field decay in transverse direction of bounded surface plasmon wave at the interface of metal (Gold) and dielectric. εm and εd are the metal and dielectric permittivity values.

2.4.2. Launching surface plasmons

The wavevector mismatch between the propagation constant of plasmon waves k_x and in-plane momentum of impinging photons k can be overcome by using diffraction effects at a grating pattern on the Gold surface. These grating structures comprise an array of metallic fingers, rods or other periodic geometric features fabricated on the surface of a semiconductor [115-124]. Fig. 2.14 shows an array of plasmonic grating structure (side-view), which can be made by milling slits in Gold. The gap spacing between these structures allow light to pass through and reach the semiconductor that enables optical field enhancement under sharp edges of the structures.

For a one-dimensional grating of slits as depicted in Fig. 2.14, phase-matching takes place whenever the condition [125]

$$k_x = k_o \pm m\frac{2\pi}{\Lambda}, \tag{2.39}$$

is fulfilled, where Λ is periodicity and m = 1,2, 3…, k_o is the propagation constant of the incident photons.

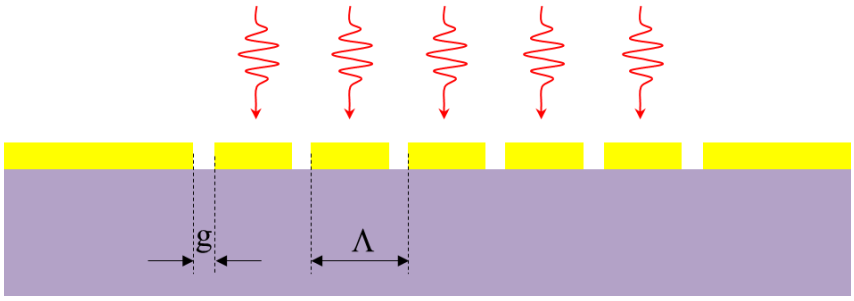

Figure 2.14 Presentation of a plasmonic structure with periodicity Λ and gap size g that can launch plasmon waves at the interface of air and semiconductor with a surface normal excitation.

Plasmonic structures have been used in many applications, such as filtering [126], spectroscopy [127], lasers, optoelectronic devices [128, 129], and waveguides [130]. Surface plasmon waves make a strong electric field specially near the edges and tips of the metal layer [131, 132]. In the case of photoconductive antennas, a thin adhesion layer is usually deposited between dielectric and metal. Titanium or chromium are two popular adhesive materials for Gold and GaAs. Aouani *et al.* has recently studied plasmonic enhancement in a 120 nm gap size hole on different adhesion layers [133]. By comparing fluorescence emission, it was shown that Ti can provide stronger field at the interface which is important for carrier generation. Cr enhances the electrical field on top of the plasmonic structure (the interface of Gold and air), resulting in a weaker field inside the photoconductive material.

The thickness of the Gold, the size of the gap and the periodicity with respect to the incident wavelength determine transmission and reflection. High optical transmission (>70%) is achievable with periodic plasmonic structures similar to Fig. 2.14. The periodicity and gap size are usually obtained from FDTD simulations [113, 134].

In a research by Heshmat *et al.* plasmonic structures were used to enhance optical coupling to GaAs [113]. In similar works, over one order of magnitude enhancement in

THz current with plasmonic contact electrodes was reported [39, 113, 135]. Berry *et al.* have claimed 250 μW of THz power radiation from a plasmonic structure in comparison with some 12 μW power from a conventional large gap photoconductive antenna [136]. Park *et al.* have reported 2.4 fold total optical power enhancement at the interface of metal and photoconductive material using plasmonic nano-antennas [135]. THz amplitude and bandwidth improvement using such structures is the main scope of this thesis.

2.4.3. Surface plasmons in THz frequencies

In the THz frequency range, the real part of metal permittivity is over two orders of magnitude higher than that of the dielectric. Hence, propagation constant of waves at the interface is simplified to $k_x \cong k_0\sqrt{\varepsilon_d}$ that leads to a slower field decay rate at the interface and poor confinement of surface waves [137]. This type of waves was first studied by Zenneck and became known as Zenneck waves [138]. In THz regime, ε_m is mostly imaginary. Thus, the attenuation length δ_m and δ_d can be found from [1]

$$\delta_m = \frac{1}{\Re[k_m]} \cong \frac{1}{\pi\sqrt{2|\varepsilon_m|}}\lambda_o, \tag{2.40}$$

$$\delta_d = \frac{1}{\Re[k_d]} \cong \frac{\sqrt{|\varepsilon_m|}}{\pi\sqrt{2}}\lambda_o, \tag{2.41}$$

where free space wavelength k_m and k_d are wavenumbers of metal and dielectric at THz free space wavelength $\lambda_o = 2\pi / k_0$. By comparing δ_m and $\delta_{d,}$ it becomes clear that the electrical field at THz frequencies extends into dielectric much further than its wavelength e.g. a few centimeters.

Unlike the optical regime where subwavelength confinement is usually obtained at frequencies near plasma frequency, plasmonics at THz employ structured surfaces to circumvent the limitations of lower frequencies. For example, extraordinary transmission of terahertz waves through metallic hole arrays was studied by Azad *et al.* [139] and [140]. Chen *et al.* studied THz waves coupled into a 2 nm wide slit that leads to field enhancement factor of 1300 [141]. In another work, surface plasmons are guided on a periodically corrugated conical wire and focused down to 1 μm at its tip [132]. Such configurations have found applications in near field imaging, THz filters, sensing, and manipulation of nanometer scale structures [142-144].

Chapter 3 : Fabrication and experimental methods

3.1. Fabrication processes

This chapter explains standard fabrication processes and measurement techniques for prototyping and testing photoconductive antennas. Procedures and recipes that were used for preparation of each sample were repeated multiple times for each project. Typically, substrates are grown in-house at the molecular beam epitaxy (MBE) laboratory. Then, antennas were patterned on the surface of the semiconductor using a photolithography process. An accurate geometry can be milled through metals using focused ion beam with 10 nm resolution. It uses an accelerated stream of Ga+ ions to cut the surface at nano-scale. The excess Ga+ particles, oxide layer or biochemical residuals are typically cleaned using wet etching or plasma etching techniques prior to packaging. The final step is to mount photoconductive antennas on printed circuit boards (PCB). To ensure electrical connection to laboratory equipment, Gold wire bounding or silver paste was used.

3.1.1. Molecular beam epitaxy growth of thin films

There are different methods of growing crystalline semiconductor layers in industry. Molecular beam epitaxy (MBE) has the highest crystal quality among all methods. MBE growth is expensive but clean and accurate. With an MBE machine, pure thin films of crystalline semiconductors can be grown with precise controllability of the thickness, material composition, and growth temperature.

The VG-V80H MBE machine at the University of Victoria consists of three sections that are separated by gate valves: growth and preparation chambers and a load lock. The goal of the design is to keep the growth chamber ultra-clean and under ultra-high vacuum at a pressure less than 10^{-9} Torr. An epitaxy layer is grown on top of a crystalline substrate. In this work, semi-insulating GaAs (001) orientation, 2" wafers were used as a substrate for LT-GaAs devices. For the first step, a GaAs wafer is heated up to 460 ^{o}C in the preparation chamber to remove the moisture from its surface. Once the substrate is placed inside the growth chamber, its temperature is raised to 610 ^{o}C for 10 minutes under Arsenic flux. This process ensures the oxide layer formed on the substrate is removed prior to growth. The oxide removal process leaves the surface with 40 nm craters. Therefore 500 nm of GaAs buffer layer is usually grown at 580 ^{o}C on the substrate to smooth the surface. Now the substrate is ready for epitaxial growth of desired materials.

3.1.1.1. MBE growth of low temperature GaAs

Growing a LT-GaAs layer requires lower operation temperatures (200 ~ 270 ^{o}C) at a certain ratio of Arsenic and Gallium. In fact, more Arsenic is incorporated during the film growth process at a low temperature, resulting in desired excess Arsenic clusters. The ratio is measured with a retractable ion gauge that reads the beam equivalent pressure (BEP) at the location of the substrate. Later, the BEP number of sources will be translated to flux ratio [145].

Arsenic defects are actually damaging the lattice structure of the GaAs (Fig. 3.1). Therefore, as the As/Ga ratio increases, the chance of continuing a crystalline growth

decrease. LT-GaAs growth stops when the substrate surface roughens. Reflection high energy electron diffraction (RHEED) and light scattering setups are used to monitor the surface evolution during growth. A beam of electrons is emitted to the surface and the RHEED setup detects the diffraction pattern, which contains information about the way atoms line up on the surface [146]. A beam from a 488 nm laser hits the surface and its specular reflection is allowed to leave the chamber through a window while the scattered light is detected by a photo multiplier. The scattered light intensity corresponds with the surface roughness. Relaxation in the growing occurs when the light scattering signal increases and RHEED pattern turns from elongated lines into star shape spots. At this time, the growth is no longer crystalline and has to be stopped. For example, surface roughening happened at the thickness of 500 nm for a LT-GaAs layer with As/Ga (BEP) ratio of 20, whereas a thickness of 3 μm was achieved without any roughening with the As/Ga (BEP) ratio of 3.2.

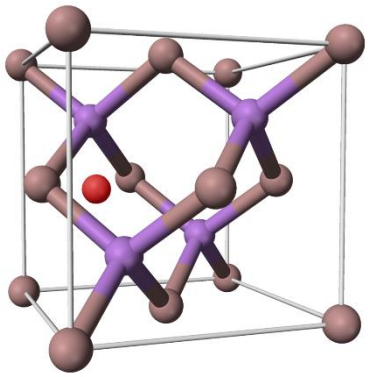

Figure 3.1 Lattice structure of GaAs with an interstitial Arsenic (red ball). Grey balls are Gallium atoms and blue balls are Arsenic atoms (reconstructed from [147]).

Once the epitaxial growth stops, the substrate is taken out for quality check. At The University of Victoria, a D8 Discovery high resolution x-ray diffraction (XRD) Bruker

machine was used to evaluate thickness and defect concentration of MBE grown LT-GaAs. Diffraction of an x-ray beam with the wavelength in the order of the spacing of the atomic planes gives the Fourier transform of the atom distribution in the lattice. An XRD machine collects multiple diffraction patterns by emitting and detecting x-ray beams from different angles with respect to the surface planes (Fig. 3.2). When angles ω and 2θ satisfy Bragg diffraction condition for a certain set of crystal planes, a peak appears. The height, shape and angle between diffraction peaks gives information about thickness, composition and even crystal relaxation.

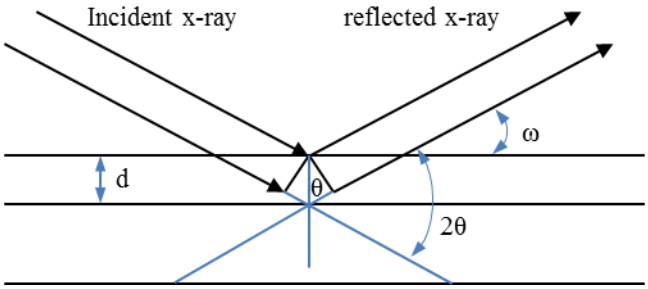

Figure 3.2 Crystalline planes and diffraction of incident x-rays.

Fig. 3.3 compares XRD curves for two LT-GaAs materials. The right peak is from SI-GaAs substrate. The left is a result of LT-GaAs layer. For example, the height of the left peak shows the thickness of the LT-GaAs. The separation between peaks shows how much the LT-GaAs is different to a pure SI-GaAs e.g. Arsenic content. A software models the pattern by sweeping thickness and As/Ga ratio and once the model matches the measured curve, the accurate thickness and As/Ga ratio of the LT-GaAs are found.

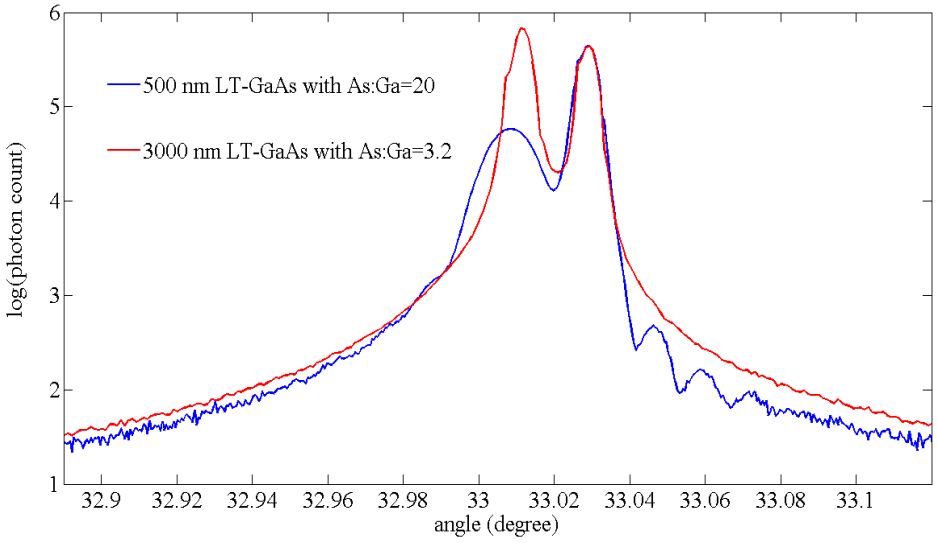

Figure 3.3 X-ray diffraction results. The red curve belongs to a low Arsenic but thick LT-GaAs substrate and the blue curve belongs to a thin but Arsenic rich LT-GaAs.

3.1.2. Photo-lithography

With an inexpensive material and processing cost, lithography is the primary part of the PCA fabrication after MBE growth. It relies on the change in chemical property of a thin resist layer under UV light. Photolithography involves light exposure through a mask to project images on a flat surface. There are two types of patterning. First, is contact photolithography that uses 1:1 scale mask in contact with the surface of the material (see Fig. 3.4). Second, is projection photolithography where the mask is a bigger replica of the pattern. In the case of non-contact photolithography, light passes through the mask and focuses on the surface with a set of optical lenses. In both cases, light diffraction places a limit on the smallest size of the features. The diffraction limit is about one-half of the wavelength of light [148] and that is the reason why precision lithography has been shifted to UV and X-ray wavelengths.

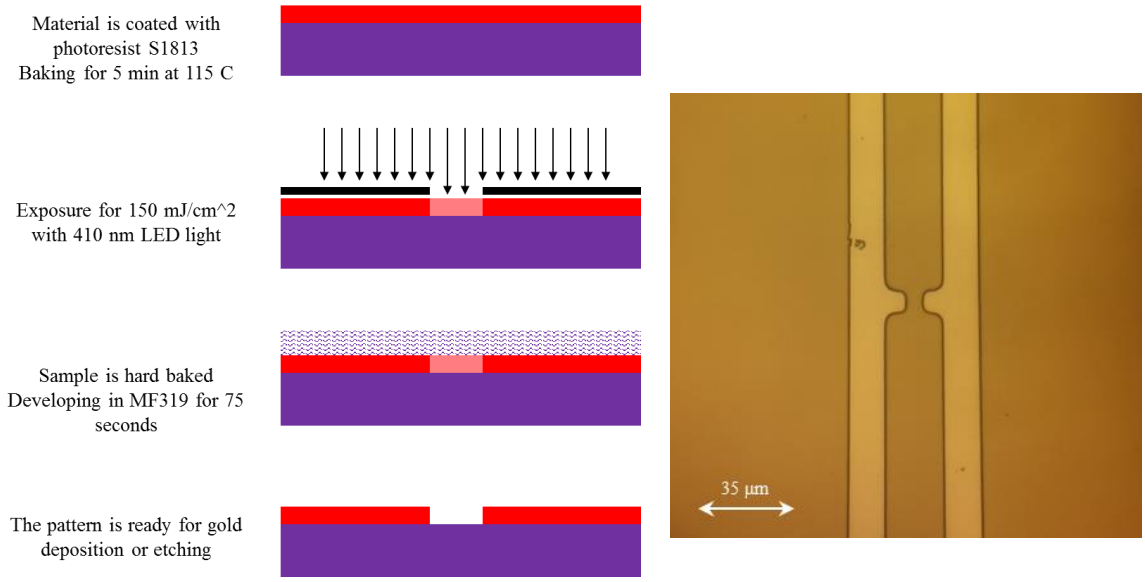

Figure 3.4 Left: photolithography processes used for PCA fabrication. Right: image of a GaAs substrate sample patterned with a large gap dipole structure and ready for metal deposition.

The process starts with cleaving wafers. In this work all samples were 5 × 5 mm slices. Below is a step-by-step recipe to pattern antennas with facilities at the University of Victoria.

- **Surface cleaning:** Dust and small particles are typical contaminants on the surface of the substrate. Using labeled wash bottles, each sample must be cleaned by acetone, isopropanol and DI water respectively. Then, the liquids must be taken away immediately using a compressed nitrogen blower.
- **Oxide layer removal:** An oxide layer forms on the surface of GaAs with a logarithmic growth rate after first contact to air. It is the fast in first few hours and slows down as the thickness reaches 40 Angstrom [149]. The oxide can be removed

if the sample is submerged in an aqueous solution of (1:1) HCL: H_2O for one minute [150].

- **Spin coating with photoresist:** The substrate must be held at the centre of the spinner by vacuum. Depending on viscosity of the resist, a uniform layer obtains with 3000-6000 RPM spinning speed. For example, a thickness of two micrometers is achieved at 5000 RPM for S1813 resist.
- **Soft baking:** In this step the photoresist hardens. Each resist has its own specifications. Baking parameters for S1813 is 115 ^{o}C for 5 minutes on a hotplate. In general, higher temperatures give slower development rates, and lower temperatures do the opposite.
- **Exposure:** Samples were exposed to 40 mW of UV light for 8 seconds. According to the datasheet 150 mJ/cm^2 exposure dosage is required around 410 nm wavelength for S1813 photoresist.
- **Hard baking:** Similar to soft baking, a 5-minute bake time is required at 115 ^{o}C for S1813 photoresist.
- **Developing:** MICROPOSIT MF319 was used for developing all exposed samples. The optimum timing for MF319 was found to be 75 seconds. MF319 does not stop dissolving the photoresist after 75 seconds. Thus, timing is important if a number of samples must be produced with equal dimensions.
- **Washing:** Samples were submerged in DI water for at least 20 seconds. It is important to keep samples clean and to place them in vacuum within few hours after the photolithography process.

3.1.3. Electron-beam deposition

Electron beam (E-beam) evaporation is a form of physical vapour deposition (PVD) process that uses electron beam to heat a source material in vacuum similar to the drawing in Fig. 3.5. Thermionic emission with a filament and electron beam steering using magnetic fields are the two fundamental mechanisms of each E-beam machine. E-beam requires vacuum pressure less than 7.5×10^{-5} to allow electron emission and beam guidance without arcing [151]. Thus, the chamber must be pumped for 2~6 hours depending on the performance of its cryopump.

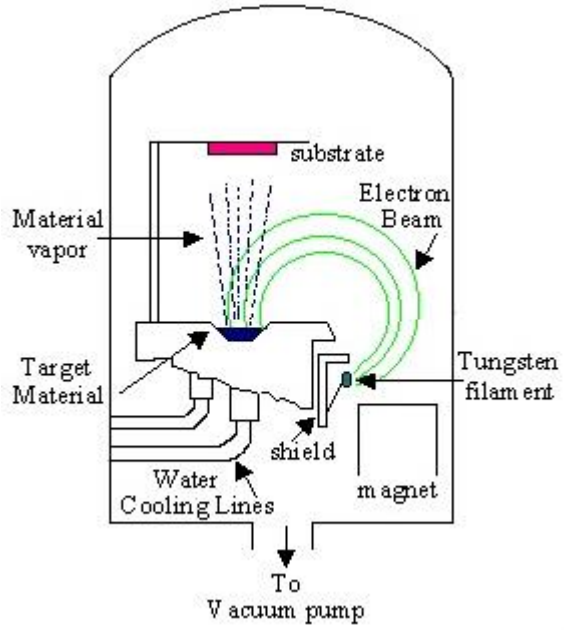

Figure 3.5 Diagram of a typical electron beam evaporator. The target source is heated by an electron beam. The evaporated source material rises up and coats onto the substrate.

Once the electron beam falls on the surface of the source material, the temperature rises and the material evaporates and coats the surface of the sample holder above the source. A crystal sensor monitors the growth rate with an angstrom per second resolution (typically 1 A/s). The source can be any kind of metal or oxide. For conductors, Gold is the most popular source material. But, it does not bond with GaAs and an adhesion layer

is needed to hold it on the surface. For our samples, 5 nm of Titanium was deposited prior to the Gold evaporation.

Lift-off is the final process after the E-beam evaporation. The photoresist dissolves in remover liquids (solvent) e.g. acetone. The Gold that is deposited on the resist peels off in the solvent, leaving the patterned area intact. Note that deposition and lift-off is very effective for thin layers of Gold but for thick layers, surface polishing may be used. Sometimes and especially for thicker Gold layers (>150 nm), edges of Gold bends and flips over the electrodes.

3.1.4. Plasma etching and cleaning

Plasma etching is a form of etching technique that uses a stream of high-speed ionized gas particles to etch the surface of the sample. These particles collide with atoms of the target sample and produce volatile products that will be removed by a gaseous stream. At high energies, plasma etching can be used to cut and modify the sample. In this work, it was used only for cleaning purposes.

3.1.5. Rapid thermal annealing

As mentioned earlier, annealing helps to reduce conductivity and carrier-lifetime of the low temperature grown GaAs samples. Annealing is very sensitive to temperature variations and time. The quality of the process is dependent on how sharp the temperature rises and drops.

At the University of Victoria, this process was performed via a vacuum chamber connected to a turbo pump (Fig. 3.6). An operator manually controls the duration of the process. The temperature rises instantly as a halogen light bulb turns on under a copper sample holder. A k-type thermocouple was mounted on the surface of the copper holder

and to monitor the temperature. A closed loop controller module turns the light bulb on/off in vacuum to maintain a pre-set temperature. Once the annealing time elapses, the operator must vent the chamber immediately with nitrogen gas.

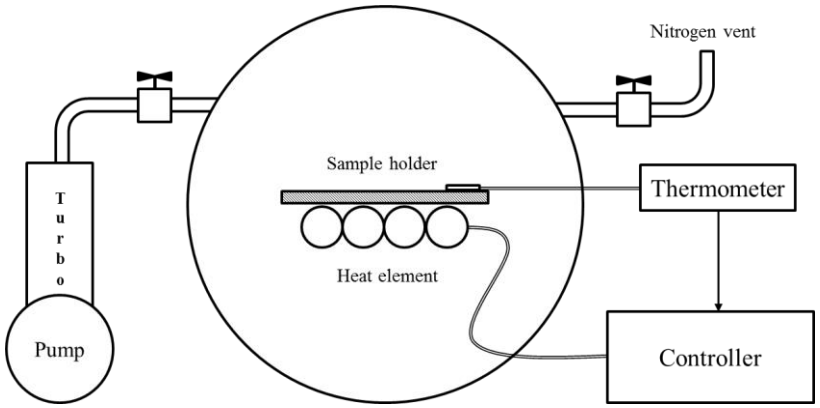

Figure 3.6 Diagram of the rapid thermal annealing chamber used at the University of Victoria.

3.1.6. Focused ion beam

Also known as FIB, it is a milling machine used in semiconductor industry with nanometer fabrication accuracy. The operation principle of FIB resembles a scanning electron microscope. But, it uses a focused beam of positive ions instead of electrons e.g. Ga+ is used for Hitachi FB-2100 FIB at the University of Victoria. A stream of high velocity ions bombards the surface of the sample, resulting in a controllable material removal. Beam steering, alignment, and stigmation correction are performed with a set of condenser, octopole, and objective magnetic lenses. A detector is usually positioned beside the sample to collect the reflected ions for creating real-time images. Usually multiple beam configurations are available with a FIB machine. For our fabrications 40-1-15 and 30-0-30 were used. The first two digits show the acceleration voltage in kV, the middle digit shows whether the condenser lens is on/off and last two digits show the beam intensity (Ga+ aperture size). The condenser lens provides better accuracy and

increases the beam power. The aperture size controls number of ions that fall on the surface.

Hitachi FB-2100 accepts 2000 × 2000 pixel bitmap images to pattern the working area. Fig. 3.7 shows an interdigitated plasmonic structures fabricated by FIB with a pre-designed bitmap mask. The size of the array is usually determined by the GaAs thermal breakdown (~1 mW/μm^2 light intensity) and it is about 7 × 7 μm for our PCAs. For this size, 20 k magnification results in 10 nm cut resolution. The Ga+ beam sweeps the bitmap pattern with 1 μs dwell time. Number of sweep iterations depends on the Gold thickness and it is about 100 times for a 100 nm Gold film using 40-1-15 beam. Reducing the number of iterations and increasing the dwell time may have a same result. However, prolonged stay (larger dwell time) increases the heat and deforms the edges of the Gold during milling process.

It is also important not to cut the photoconductive material. One way to find the optimum iteration number is to cut rectangles in a practice area and look for any significant change of the pattern. The color of the surface changes as the FIB reaches the interface between Gold and semiconductor.

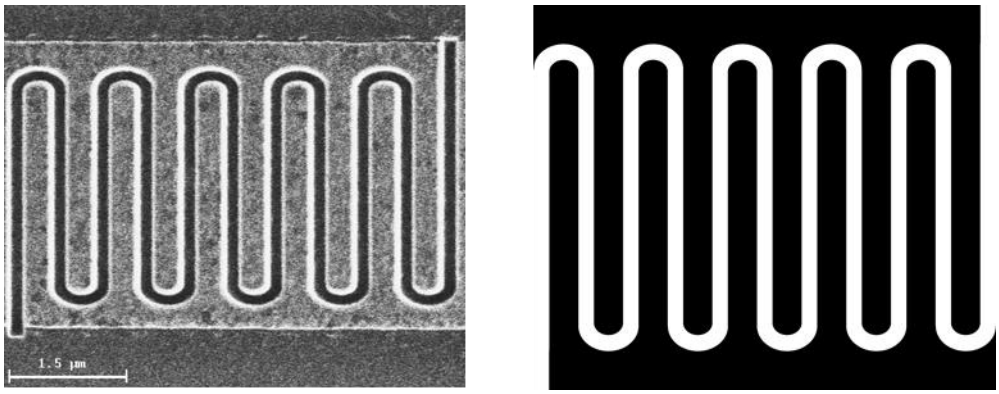

Figure 3.7 Left: horizontal plasmonic structure fabricated on a 100 nm Gold strip. Right: bitmap mask drawn by CorelDraw and imported to the FIB for patterning the Gold surface.

Ga+ ions usually embed in GaAs after FIB processes and increase the conductivity of the processed area. The common way to remove Ga+ ions is to submerge the sample in an aquatic solution of (1:1) HCL: H_2O for 10 minutes. Care must be taken as the nanostructures are very delicate and may be removed by the air blower or water wash.

3.1.7. Characterization using scanning electron microscope

The scanning electron microscope was invented to see objects below the diffraction limit of visible light. It uses an electron beam to scan across the sample surface. When high-speed electrons strike the material, multiple signals are generated. While an electron count detector collects electrons for imaging the surface, an x-ray detector looks for high energy photons emitted by electrons colliding with the sample (see Fig. 3.8). The energy of the photon carries information from the parent element. Analysis of this signal (Energy Dispersive X-ray Spectroscopy or EDS) provide elemental composition information of the sample. It can also show elemental distribution on the sample surface.

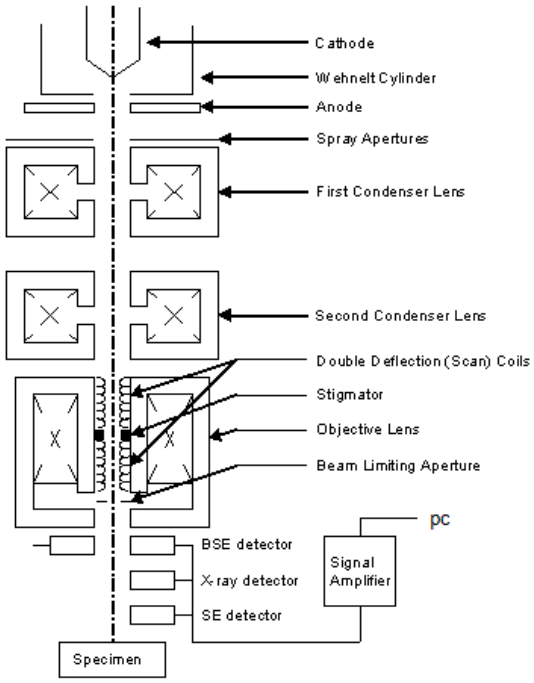

Figure 3. 1 diagram of a scanning electron microscope (SEM).

EDS at the university of Victoria was used to determine bismuth from Ga that form Ga-Bi droplets on top of the GaAsBi surface. The SEM was also used for taking high resolution images of the nano-structures.

3.1.8. Wet etching of metals and semiconductors

Wet etching refers to fabrication processes that involve liquid etchant for removing target materials. One advantage of using wet etching as opposed to plasma etching is selectivity. Chemicals can be chosen such that they only react with a specific material at a controllable etch rate. As mentioned earlier HCL: H_2O was used for removing Ga+ and the oxide layer formed on the surface of GaAs. The important benefit of this compound is that the hydrochloric acid neither attacks Gold, nor GaAs.

The photoconductive material can be etched selectively as well. A MESA structure for example, is an etched out column of photoconductive material grown on a latticed

matched substrate [110]. To etch GaAs or LT-GaAs, one can use aqueous solution of (5:1:1) H_2SO_4: H_2O_2: H_2O (rate: 1.4µm/s) [152].

It is also possible to etch the Gold layer without affecting the GaAs substrate. Gold and iodine form Gold iodide and it can be removed by adding KI into the solution. The Gold etch rate of 1um/min is expected in a mixture ratio of (4 g: 1 g: 40 ml) KI: I_2: H_2O at room temperature. Titanium can be removed by HF or a concentrated HCL acid. These processes can help salvaging valuable photoconductive materials from defective PCAs.

3.2. THz time domain spectroscopy setup and alignment

Transmission and detection are line of sight in a typical THz-TDS setup, which was also used in this thesis. With focusing silicon lenses, The THz beam will have a Gaussian beam profile, which is narrower for higher frequency components. Thus, it is challenging to obtain the best bandwidth with the initial alignment. Fig. 3.9 Shows a THz-TDS setup and component labels that are necessary for the alignment.

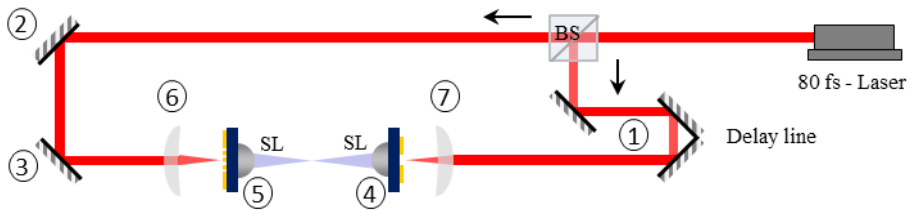

Figure 3. 2 step-by-step alignment procedure for a THz-TDS setup.

As the first step, it is essential to align two optical beams (transmitter pump beam and receiver probe beam) such that they propagate in parallel with the surface of the optical table. The delay line is a retro-reflector mirror on a motorized stage, which is less sensitive to misalignment. The path of the transmitter beam can be aligned by adjusting two knobs of the kinematic mirror mount. An iris may be used to check the position of

the beam in front, and far from the mirror. If the iris translates horizontally/vertically on the table and the beam passes the iris, the beam in aligned and it is parallel to the surface.

Now, mirrors 2 and 3 must be placed in the setup. The probe beam should be aligned with these mirrors such that it exactly follows a same path as the transmitter beam propagates. To do that, the third mirror must be placed at the spatial location such that both beams cross each other orthogonally. The role of the third mirror is to re-direct the probe beam exactly on the transmitter beam.

Once the optical path is established, silicon lenses (number 4 and 5) should be inserted in the setup. Laser beams must illuminate the approximate centre of each silicon lens. At this time, the position of silicon lenses is not accurate but it should be enough for getting the initial THz signal.

The next step is to insert optical lenses (number 6 and 7) in place with their flat surfaces facing silicon lenses. If the laser beam is orthogonally incident on silicon lenses, translation of optical lenses must result in circular spots at focus of the laser beams. If this condition is met, the PCA should be placed inside the setup with its back side touching the silicon lens. Because all lenses are positioned along a straight line, it is better not to change their locations at this time.

A camera, which is sensitive to the excitation wavelength can be placed beside the setup to look at the reflected beam coming from the surface of the sample. The camera may need a beam splitter that deflects the reflected beam from the direction of the through beam. Real-time video of the PCA at microscale is a vital tool for alignment. The active area of each PCA must be moved toward the location of the lasers at focus.

If PCAs are biased, their photocurrent increases once the laser beam scans their gap area. The photocurrent must be maximized by slightly tweaking the spatial position of the optical lenses.

Now if the biased transmitter is chopped electrically or optically and the frequency of the chopping is fed to the lock-in-amplifier connected to the receiver, a small photocurrent appears. By changing the position of the delay line, the peak of the THz signal may be found. At this point, it is not likely to have an optimum alignment with the best bandwidth. Fig. 3.10 shows three different signals recorded for different positions of the silicon lens.

If the THz beam hits the dead centre of the silicon lens, it travels the longest thickness of the silicon. Therefore, the sharpest THz signal always appears with maximum delay. The best alignment technique is to move the silicon lens and record the position of THz signal on the time axis. The full width half maxima FWHM and bandwidth must be monitored in each step as well. This algorithm must be repeated for both x and y axis to obtain the maximum bandwidth.

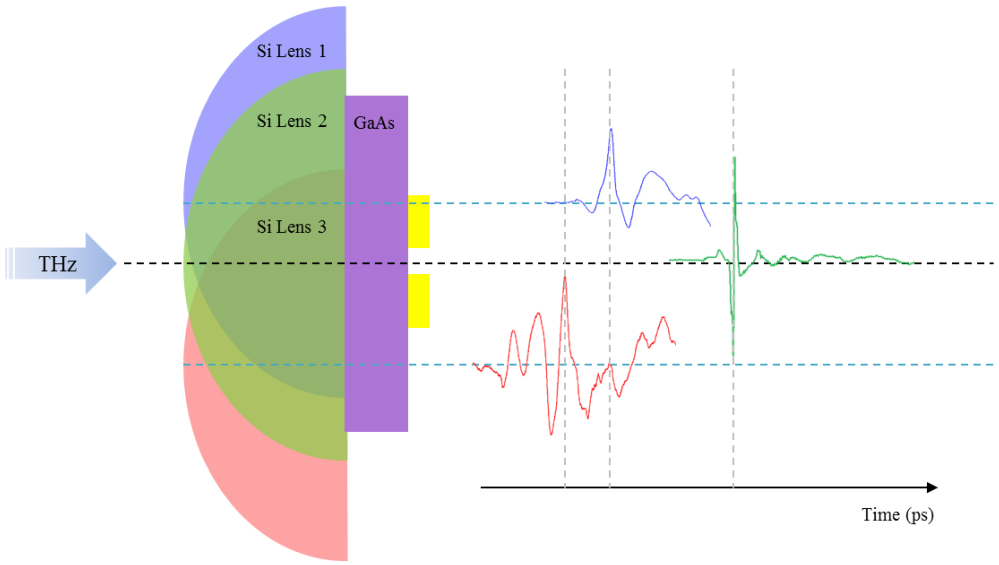

Figure 3.8 Illustration of the THz signal quality with respect to the position of the silicon lens. The best THz signal has the smallest FWHM and appears with the longest delay because the THz beam passes the thickest portion of the silicon lens (green lens).

3.3. Computational processes and data acquisition

Typically, a lock-in amplifier reads the current that is generated by the receiver PCA. Since the delay line maps the phase of the THz signal, displacement of the delay line translates into time. In our measurements, the delay line has a maximum displacement of 20 mm corresponding to a 132.5 ps time window. An application was developed in C# to communicate with the lock-in amplifier through GPIB port and to control the delay line. The software moves the delay line step-by-step and reads the current from lock-in amplifier. The output is a CSV file with two columns; time and signal amplitude.

Because each THz pulse contains the whole spectral information, the speed of the measurement is only limited to the speed of the motorized delay stage and the time constant of the lock-in amplifier. Of course, a longer integration time results in a lower noise, but it is also possible to average multiple scans to eliminate the effect of noise. Wieweg *et al.* demonstrated a bandwidth of 4.5 THz with 90 dB dynamic range by

averaging 1000 scans at 4.4 s integration time [153]. Most of the measurements at the University of Victoria were single 180 seconds long scans with 1 second lock-in amplifier integration time resulting in 50 dB dynamic range. Nevertheless, scanning at much faster speed is possible if the delay line is equipped with an oscillatory transition stage and calculations are performed by a fast processor at real-time.

The spectrum of the THz signal can be obtained by taking the fast Fourier transform (FFT) over the time window. Note that the signal level at the start and the end of the time window must be equal. Otherwise, the discontinuity results in ringing in the spectrum. In our presentations, the power spectrum is two times of the absolute value of the FFT result in a log scale. A simple MATLAB code such as the one shown Fig. 3.9 provides a matrix with spectral information of the THz signal.

```
% ========================================  Fast Fourier Transform ==============
L=length(X);                                % Time matrix e.g. 132.5 ps for 20 mm delay
data = Y;                                   % Y is the THz amplitude matrix for X
period = 1e-12*max(132.5);

T=period/L;
Fs=1/T;

nfft = length(X)*1;                         % Multiply by 2,3,... for more spectral details

full_fft = abs(fft(data,nfft));             % Taking fast Fourier transform
NumUniquePts = ceil((nfft+1)/2);
f = (0:NumUniquePts-1)*Fs/nfft;

Spectrum = abs(log(2.*full_fft));           % Obtaning power spectrum from amplitude


plot (f(1:300),Spectrum(1:300))             % Plotting results

```

Figure 3.9 Simple MATLAB code for obtaining the power spectrum of the THz detected photocurrent. Y is a matrix of THz current amplitude as a function of time X.

It is also important to mention that the tail of the THz signal has essential information about the material inside the THz path. Thus, the THz peak must be the in first quarter of the time window.

Chapter 4 : Simulation, modeling, analysis, and measurement results

4.1. FDTD simulation methods

The design principle of PCAs combines multiple fields of science and physics. It includes optics and photonics, electromagnetics and material science. Thus, performance of the design may not be estimated solely using a single simulation environment.

The optical response of the system can be simulated with finite-difference time-domain (FDTD) method. In this method, both space and time are segmented into small discrete elements. The field vectors are known on each cell and time is quantized into small segments that the electromagnetic wave needs to travel from one to the other cell. The time-dependent Maxwell's equations (in partial differential form) is applied to each cell to find the electric and magnetic field components. At each step of time, electric fields and then magnetic fields are computed. The combination of many FDTD cells provides a map for the field distribution inside the simulation volume [154]. Numerical calculations continue while field values decay and until a state of convergence has been reached e.g. the total field inside the simulation area decays to a pre-defined value like 10^{-6}. In this work, FDTD was used to simulate interaction of light with the gap area of the PCAs. The periodicity and gap size of the plasmonic structures are obtained from Lumerical FDTD Solutions V 8.15.758.

4.1.1. Optical field coupling analysis and plasmonic structure design

To find the best periodicity and size of the plasmonic structures it is most efficient to simulate a single cell of the structure. Because an array of unit cells is usually fabricated inside the active area, periodic boundary conditions may be applied to the FDTD simulation volume. Once the design is complete, the software can sweep dimensions, wavelengths, or any other variables using a script command file one by one. This is a common way to find optimum parameters of periodic plasmonic structures.

Modeling starts by building components. Solid structures can be used to define geometrical shapes of the unit cells. Materials are available in a library and they must be assigned to each component correctly. For example, Palik [155] and Johnson & Christy [156] permittivity values were used for GaAs and Gold respectively. If permittivity values (real or imaginary parts) are not in the library, it is also possible to add them manually at discrete wavelength set-points. The user must define a simulation region by placing FDTD boundaries and setting up the mesh size. A general rule of thumb is to use ten cells per wavelength to obtain an acceptable resolution. Then, sources and monitors must be placed at desired locations. Fig. 4.1 shows a 2-dimentional view of a single resonator on GaAs. Monitors on the surface, behind the source and deep inside the material provide normalized transmission, field and power values at the location of the monitors. The difference between transmission values on the surface and deep in the GaAs indicates the amount of light that is coupled into the specific depth of the semiconductor. Maximizing this value is the goal of each simulation.

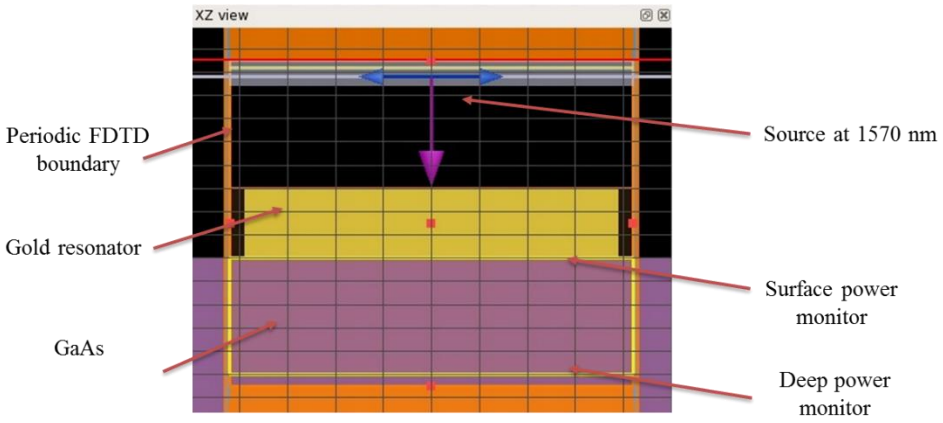

Figure 4.1 2D view of a single cell in Lumerical FDTD simulation environment. Here, the pink arrow points at the direction of the light and blue arrows show the electric field polarity.

Two main plasmonic structures were studied in this work as shown in Fig. 4.2. A slit structure is fabricated by milling narrow grooves on the surface of the Gold. Fig. 4.2b shows a scanning electron microscope (SEM) image of an array of hexagonal cells at the centre of the dipole antenna. Simulation region (Fig. 4.1) is a side-view presentation of a single cell in Fig. 4.2c. Although stronger field is expected under the edges of the Gold inside the gap, but this is a flat edge along with the length of each slit. To further increase the field between cells, a hexagonal design was proposed.

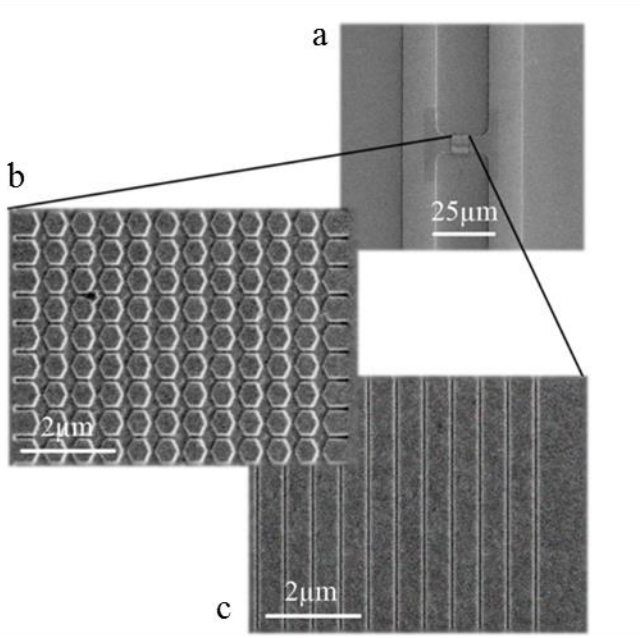

Figure 4.2 Images of nanostructures fabrication using focused ion beam at the center of dipole antennas.

Fig. 4.3 compares power density profiles of a 785 nm laser source with hexagonal or slit structures obtained from Lumerical FDTD simulations. To find the optimum dimensions, 2-dimensional periodicity of the Gold and the apex angle were varied from 400 nm to 800 nm and between 90˚ and 180˚ respectively. It was found that periodicity of 587 nm with θ=127˚ results in maximum transmission with a source at 785 nm wavelength. Hexagonal structures bring more benefits to the overall performance of the PCA, which will be discussed in next sections.

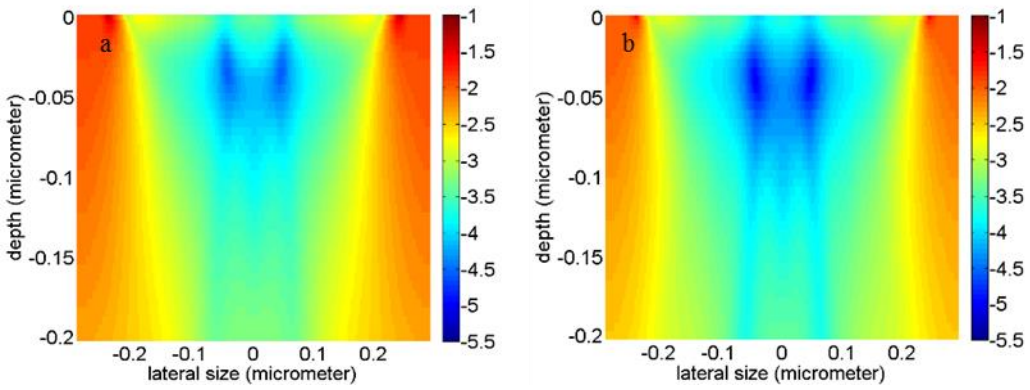

Figure 4.3 FDTD simulation results for optical power "log(|P|)" distribution inside the substrate of a single cell in an arbitrary unit. (a) cross section view of a hexagonal cell and (b) cross section view of a strip cell.

As expected, Fig. 4.4 shows a stronger optical power close to the apexes of the hexagonal cell. Because periodicity is 587 nm in both x and y directions, the structure absorbs light even with a vertical polarization (transverse electric excitation mode). This ensures carrier generation even if the light is not horizontally polarized. However, the THz signal is maximum when the polarization is horizontal.

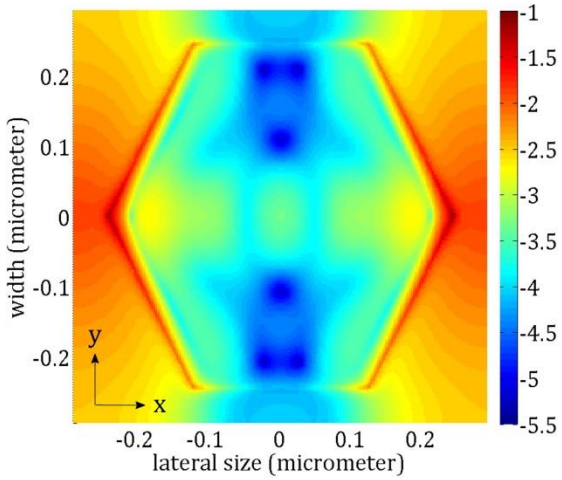

Figure 4.4 2D surface power density profile of a single cell period from top.

It is also possible to manipulate propagation of surface plasmons with plasmonic structures. Section 2.4.2 explained how a grating structure can launch surface plasmons on the surface of Gold. Usually, the periodicity of grating is smaller than the wavelength of impinging beam. A grating structure with half that periodicity can reflect the surface waves.

As an example, an array of shallow grating structure with periodicity of 772 nm was placed beside a grating structure with twice its periodicity to unilaterally launch surface plasmon waves with a normal incident source at 1570 nm. FDTD simulation result in Fig. 4.5 depicts performance of a grating reflector structure in directing surface plasmon waves to the left.

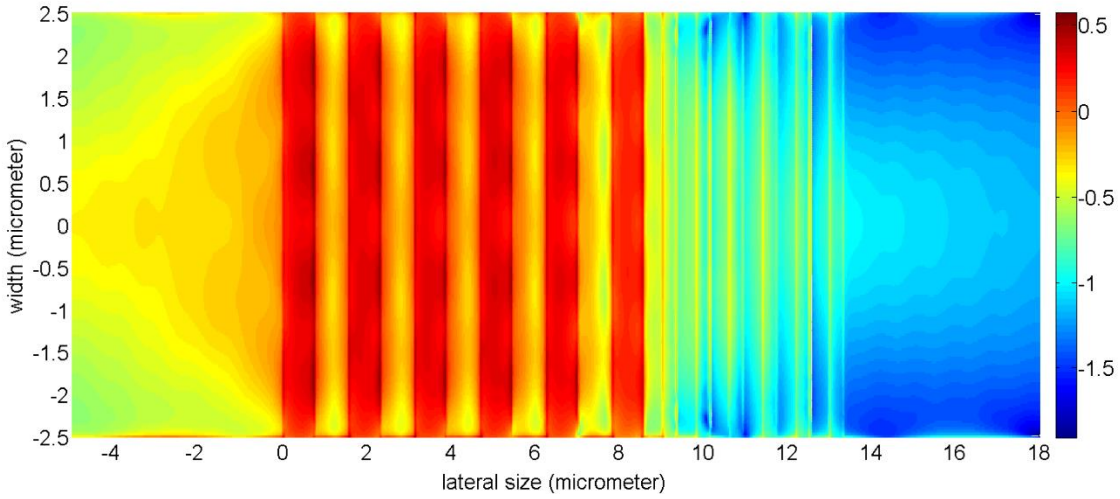

Figure 4.5 FDTD simulation of a unidirectional surface plasmon wave launch system with a grating structure and a grating reflector with periodicities of 1545 nm and 772 nm respectively. Colorbar is in log scale and in an arbitrary unit.

4.1.2. DC field distribution analysis

Since the THz radiation power is proportional to the total energy stored in the gap capacitance, it is important to have a larger bias voltage over the structure. The reason is the stored energy, which is proportional to the square of voltage i.e. $U = 0.5CV^2$ where U is the total energy, C is the capacitance and V is the voltage [31, 35]. In addition, a higher bias voltage generates a stronger electric field amplitude, which is important for acceleration of the carriers.

Plasmonic structures provide stronger localized field near the edges of metal due to shorter distance between cells. Nevertheless, filling the active area with Gold structures reduces the semiconductor gap and lowers the overall resistivity of the PCA and the breakdown threshold. Therefore, a trade-off between the gap size and bias voltage is required to obtain high power THz radiation.

Fig. 4.6 illustrates common periodic structures. The electric bias field inside the gap in all configurations is greater than a large gap dipole. Thus, stronger THz emission is expected. Note that all electrodes in both structures shown in Fig. 4.6 a and c are electrically in parallel [36, 113, 157]. Our experiments showed that maximum bias of 1 V_{DC} can be applied on a 100 nm GaAs gap. This means that both interdigitated and tip-to-tip structures are limited to one volt of bias, resulting in significantly lower radiation power in comparison with a large gap dipole.

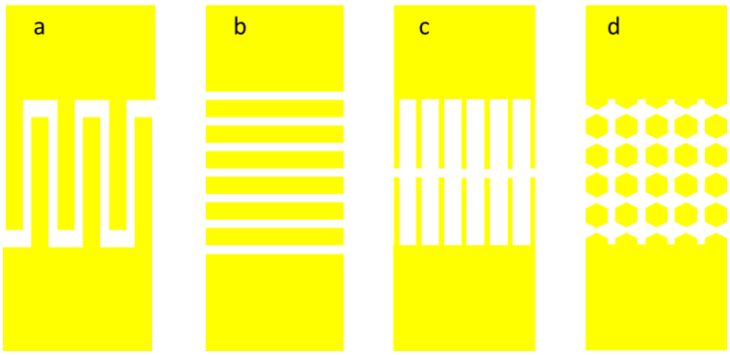

Figure 4.6 Different periodic Gold structures for optical and electrical field enhancement of the active gap area. (a) interdigitated structure. (b) slit structure. (c) tip to tip structure. (d) hexagonal structure

Our experimental studies have confirmed superiority of the hexagonal and slit structures shown in Fig. 4.6 b and d [93]. Apexes of the hexagonal cells can further increase the local field amplitude that eventually contributes to stronger THz emission. Fig. 4.7 compares the local electrical field amplitude of a hexagonal, slit, and a large gap dipole structures. Field amplitudes were obtained by monitoring the electric field at the interface of Gold and semiconductor with a source at 1 THz in a Lumerical FDTD simulation. The red spikes are associated with the apexes of the hexagonal cells and clearly show a stronger electric field at the interface of Gold and semiconductor.

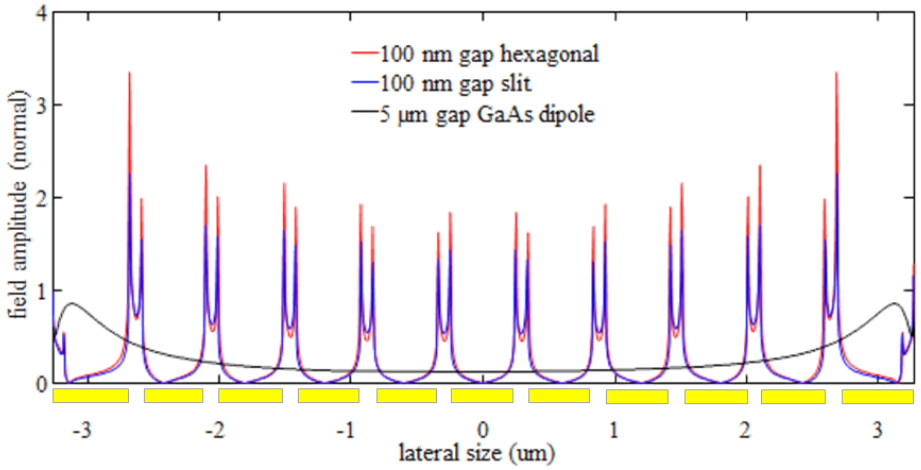

Figure 4.7 Electric field distribution across the active area and on the surface of GaAs obtained from Lumerical FDTD simulation. Strongest field peaks belong to the hexagonal array structures. Yellow rectangles represent Gold cells and the gap location between them.

An array of ten or more 100 nm gaps enables >10 V_{DC} bias voltage with reasonably high dark resistance (>200 kΩ) that is important to work below the thermal breakdown.

4.2. Heat management and plasmonic structures

The main reason for the failure of the photoconductive antennas is thermal breakdown. Most semiconductors, including GaAs possess poor thermal conductivity e.g. 0.55 W cm^{-1} $°C^{-1}$ for GaAs [158]. As a result, their temperature increases when substantial amount of current passes through them and convection cannot take the excess heat away. Carriers participate in the Joule heating process and further increase the chance of failure.

It has been seen that current-voltage (I-V) curve of PCAs respond nonlinearly beyond specific bias voltages [32]. Over-biasing the gap area results in gradual material deformation and thermal breakdown. Therefore, it is important to operate below the onset of nonlinearity. While this onset is 25 V_{DC} for a typical large gap (5 µm) PCA, a slit

structure can be biased up to 10 V_{DC} with ten 100 nm size grooves (see Fig. 4.8). It can be inferred that the electric field amplitude inside the slit structure is two times stronger when both devices are operating just under the thermal breakdown threshold.

Our measurements suggest that the metallic plasmonic structure improves the poor thermal conductivity of the GaAs by removing heat from the active area. More accurately, Gold has a thermal conductivity of (3.14W/cm·K), which is 6 times that of the GaAs (0.55 W/cm·K). The current density is localized underneath the Gold edges for the nano-plasmonic structures, so it benefits efficient heat removal. This process ensures safe operation of the device even at high bias voltages. Hence, carriers accelerate faster resulting in stronger THz radiation.

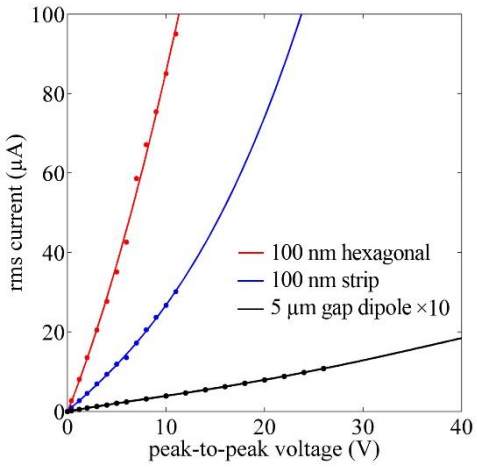

Figure 4.8 I-V curves of a hexagonal, slit and a large gap dipole photoconductive switches at dark condition. Note the onset of nonlinear response for different structures.

4.3. Lumped element model of the photoconductive antennas

There are two phases involved in operation mechanism of PCA emitters in a THz-TDS setup. First is the charging process that happens in the dark. The gap capacitor charges with the bias voltage and charges accumulate on both electrodes. Then, the optical pulse

arrives and reduces the resistance of the gap that launches a surge of current flow and generates electromagnetic radiation.

Therefore, there are two modes of operation describing operation of a PCA: DC and AC modes. In the DC mode, the source is an external power supply with equivalent components shown in Fig. 4.9a. The discharge process launches a transient current burst that forms a radiative electric field i.e. THz radiation. Hence, the AC model has a voltage source, which is at the centre of the active area. The AC source drives the input impedance of the antenna R_i as a load (Fig. 4.9b). Resistance of the gap under illumination *R(t)* is actually the internal impedance of the source.

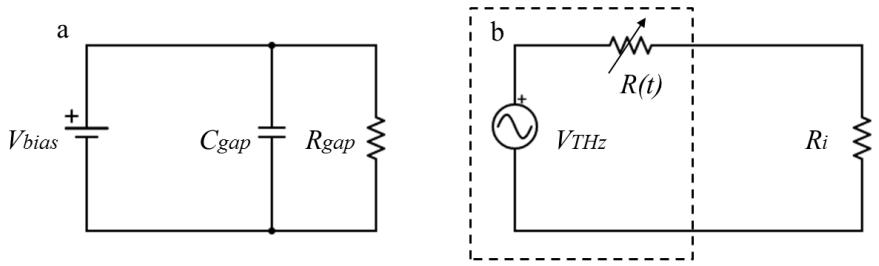

Figure 4.9 Simplified equivalent circuit model of a photoconductive antenna emitter. (a) dc model (b) ac model.

To understand the transient response of the circuit, impedances must be determined. The dark resistance of the PCA is measurable with laboratory equipment. It is around 5 MΩ for a large gap (5μm) dipole, 200 kΩ for a plasmonic slit structure and 10 kΩ for an interdigitated design with same sizes. The resistance under exposure can be estimated from photocurrents and optical pulse parameters i.e. pulse duration and repetition rate.

Because the gap capacitance is not directly measurable, a conformal mapping technique was used to estimate the capacitance of the planar electrodes on GaAs [159]. This technique includes fringing fields to accurately estimate the capacitance for any

configurations including interdigitated, slit and the large gap (5 μm) structures. For a typical active area size of 5 × 5 μm, the capacitance of a large gap PCA was 1.8 fF. A slit structure array with 10 cells has 3.2 fF capacitance and an interdigitated structure with same number of cells possess 8.9 fF of capacitance. 3D models of gap structures were designed and studied in COMSOL Multiphysics with stationary field analyzer. Simulation results confirm numerical capacitance calculations using conformal mapping i.e. with tolerance of <10 %.

With both resistance *R* and capacitance *C* of the gap, the charging time constant (*RC*) associated with each design can be easily calculated. The charging time (5 × *RC*) of the large gap, slit and interdigitated dipole structures are 45 ns, 3.2 ns, and 0.44 ns respectively. It can be concluded that the PCA is virtually disconnected from the power supply during the femtosecond exposure time because the gap is short circuited. Moreover, stronger THz radiation is expected if optical pulses arrive when the gap structure is charged. This means that a laser with lower repetition rate would potentially result in a stronger THz field at each cycle.

The detector has a relatively simpler model. From the circuit point of view, the receiver antenna can be replaced by a voltage source. Therefore, the input impedance of the antenna in Fig. 4.9b must be replaced with the inputs of the lock-in-amplifier Fig. 4.10. The impedance of the active area *R(t)* is the only resistor in the circuit that defines the amount of current, which flows through the circuit.

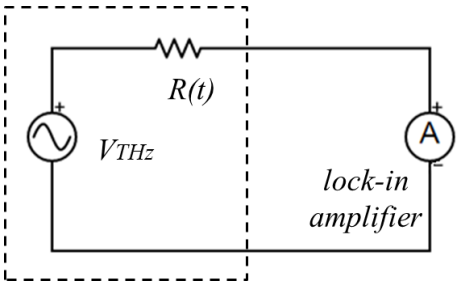

Figure 4.10 Simplified ac model of a detector photoconductive antenna.

4.4. Noise analysis

While extensive research has been conducted on increasing the THz amplitude, few studies are focused on noise. Reduction of noise may be as important as the THz signal generation for obtaining a large signal to noise ratio and dynamic range [33]. Sources of noise in photoconductive antennas are: bias or laser power fluctuations, shot noise and Johnson-Nyquist noise.

The origin of shot noise is current fluctuations of discrete carriers leaving an electrode or passing through potential barrier i.e. non-Ohmic schottky barrier of metal-semiconductor. Spectral density of the shot noise is frequency independent and it is $S_{i-shot}(\omega) = 2qI$, where q is an electron charge, I is current, and ω is an angular frequency. Therefore, the shot noise current for the frequency range Δf is

$$I_{n-shot}^2 = 2q(I_{photocurrent} - I_{dark})\Delta f \tag{4.1}$$

The dominant output noise current of the receiver is determined by Johnson-Nyquist noise. The spectral density of this type is $S_{i-\text{Johnson}}(\omega) = 4kT / R_{gap}$. The noise current can be obtained from

$$I_{n-Johnson}^2 = \frac{4kT\Delta f}{R_{gap}}, \tag{4.2}$$

where R_{gap} is the impedance of the active area, T is temperature in Kelvin, and k is Boltzmann's constant.

There are multiple approaches available to reduce the noise and increase signal to noise ratio. In a very likely case that the input impedance of the antenna becomes larger than R_{gap} under exposure, reducing the gap size or increasing the optical excitation increases the detector noise current [33]. Thus, it is better to use a large gap dipole structure. Because photoconductive antennas based on short carrier lifetime materials exhibit lower noise level, LT-GaAs can be a better candidate for designing a low noise detector.

An intuitive idea to remove carriers in a SI-GaAs based detector is to apply bias over the active area. The bias voltage ensures carriers sweep-out in sub-picosecond time, which imitates a short carrier lifetime material e.g. LT-GaAs. Our experimental results in Fig. 4.11 suggest that even a very low bias voltage over the active area of the detector can enhance both the bandwidth and the amplitude of the THz signal.

The THz current can be isolated from the DC bias with a simple inductive-capacitive filter. In the presence of a DC bias, carriers accelerate toward electrodes. However, a large bias induces heat inside the active area that degrades the signal by increasing the noise current and reducing the mobility i.e. $\mu \propto T^{-3/2}$ [160]. Thus, a biased detector may benefit from this technique with a good level of bias voltage. According to the experiments, 1 V_{DC} for large gap and 0.1 V_{DC} for plasmonic structure dipoles result in maximum signal to noise ratio.

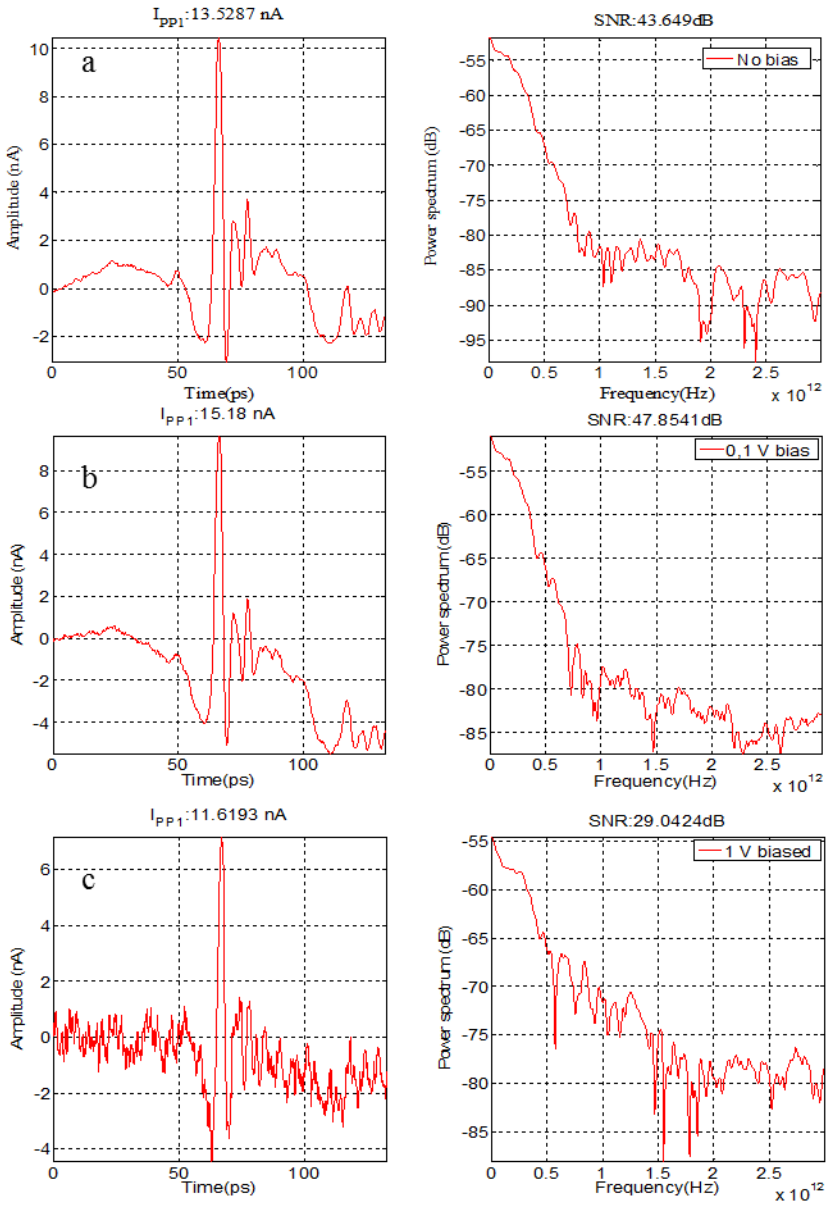

Figure 4.11 THz photocurrents and power spectrum of the biased SI-GaAs PCA receivers with hexagonal structures. (a) no bias. (b) biased at 0.1 VDC (c) biased at 1 VDC.

4.5. Measurements and experimental results

Advantages of plasmonic structures over a large gap dipole have been discussed previously. Measurement results in this section confirm superiority of plasmonic structures and study their performance. Here, we want to focus on the performance of plasmonic structures. Thus, we used SI-GaAs as a substrate to reduce the complexity of the fabrication and samples were tested at 785 nm laser. In addition, SI-GaAs has a high mobility, which is essential for a transmitter PCA. During this experiment multiple PCAs with hexagonal, slit and large gap structures were fabricated.

To be consistent, all gap structures were fabricated on short dipoles (20 μm long × 7 μm wide). A 100 femtosecond 785 nm mode-locked laser generated optical pulses with 68.9 MHz repetition rate. Transmitters were biased below the onset of the nonlinearity and received an average 10 mW of optical power. A commercial BATOP (PCA-40-05-10-800-a) photoconductive antenna was placed as a receiver during the measurements at the distance of 10.6 mm from the transmitter and exposed to an average 13 mW of optical power. A lock-in amplifier (Stanford SR830) was used to measure the received THz photocurrent. To reduce the complexity, none of the receivers were biased. Measurements were taken when the temperature and humidity were 23 ^{o}C and 32%. To verify the results, the THz spectrum was overlapped with the HITRAN water absorption lines.

Experimental results in Fig. 4.12 show THz radiation enhancement from hexagonal and slit array structures in comparison with the large gap dipole reference samples. It is clear that the hexagonal plasmonic array outperforms the commercial PCA, which uses an antireflection coating to absorb more light. As explained previously, this is due to stronger localized field next to the apexes of the hexagonal cells.

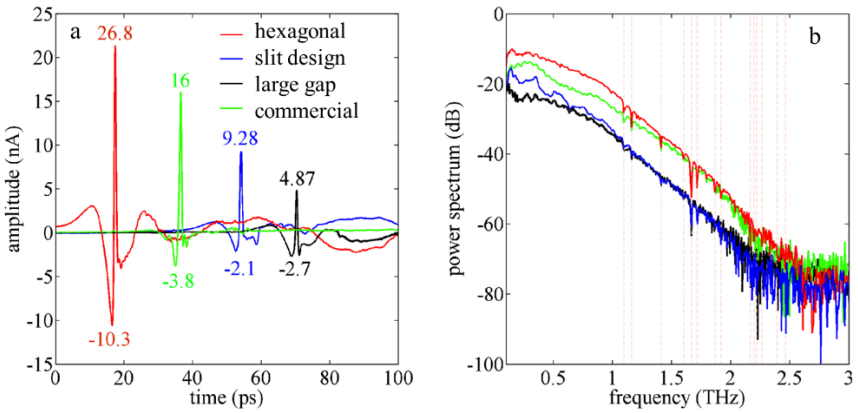

Figure 4.12 THz photocurrent received from a plasmonic hexagonal, a slit structure, a large gap dipole and a BATOP commercial PCA.

Fig. 4.13a shows the received THz peak to peak photocurrent as a function of 785 nm laser power. By comparing the hexagonal and slit-structure PCAs, it is clear that the initial slope is greater for the hexagonal array structure, in same experimental conditions including bias voltage of 10 V_{DC}. We believe that this is caused by a combination of the higher local bias field and the localization of the photo-excited carriers close to the hexagon apexes. Besides, screening plays an important role in performance of the hexagonal array structure due to the larger photo-excited carrier density. This can be seen from the saturation in the enhancement factor in Fig. 4.13b. Here, results of the hexagonal and the slit structures are normalized to the 5-micron gap.

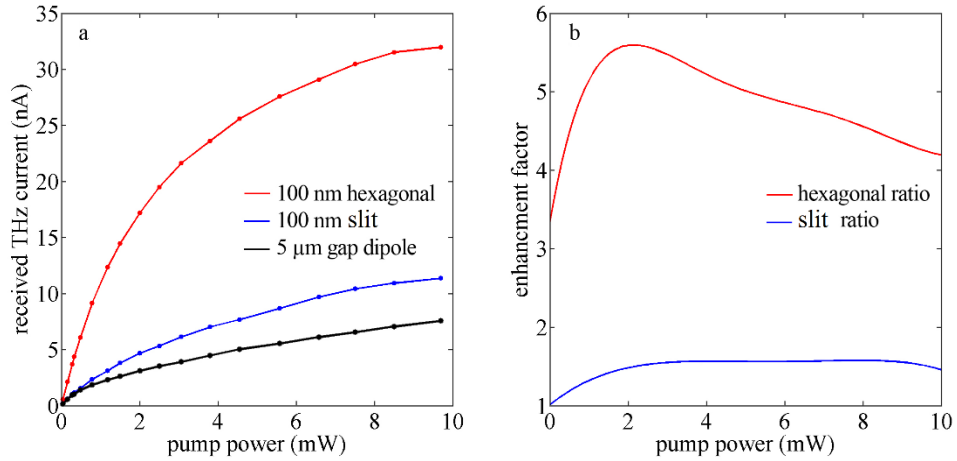

Figure 4.13 (a) Peak to peak received THz photocurrent of the samples as the function of the pump power. (b) Emission enhancement with respect to 5-micron large gap dipole.

A key factor in determining radiation efficiency of the PCAs is the photocurrent that is generated during the light absorption. Since the number of photo-excited carriers is proportional to the electro-optical power inside the gap we can re-write the current density as $J \propto PE$ where P is the 785 nm optical power and E is the electric bias field inside the gap. In a FDTD simulations a plane wave source at 0.5 THz (a nominal low frequency value) was used to find the quasi-static electric field profile in a 3-dimentional unit cell of the plasmonic structures. Then, the electric field was normalized to the voltage drop over each cell based on the experimental conditions. Similarly, the 3D optical power profile of a unit cell was obtained using a 785 nm source. The product of P and E gives the current density distribution profile inside the cell. After integrating from $P.E$ in yz plane slices, the current profile was plotted over the x axis Fig. 4.14. Lastly, the photocurrent enhancement $\eta = \int E.P dv$ was obtained by integrating $E.P$ over the active area and along the x axes.

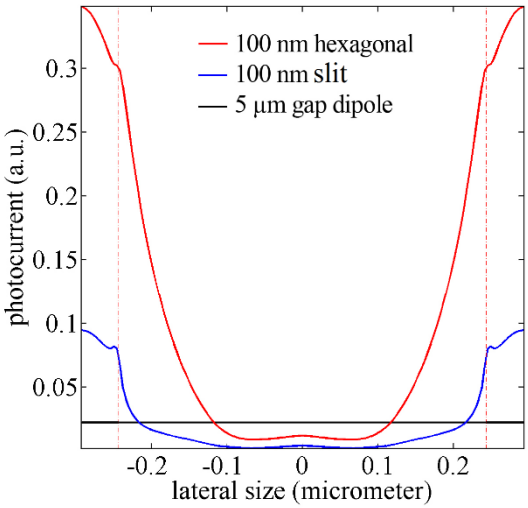

Figure 4.14 Calculated photocurrent (*P.E*) over a unit cell of the plasmonic structures. Dashed line is the edge of Gold on GaAs substrate.

In Table 4.1 the hexagonal array plasmonic structure possesses the highest enhancement factor. If we multiply η by the experimentally used bias voltages, we see reasonable quantitative agreement with experimentally measured peak to peak THz photocurrent. in this calculation, the effect of screening is neglected, which has an influence on the hexagonal structures, as described earlier. Screening explains the lower measured THz photocurrent for the hexagonal structure as compared with the numerical prediction.

Table 4.1 Theoretical and measured emission amplitudes of plasmonic photoconductive antennas. C=0.93 is a fitting constant that was applied to numerical calculations.

gap structure	η	bias (V)	$I_{THz}=\eta\times C\times V$ (a.u.)	measured I_{THz} (nA)
hexagonal	4.26	10	39.6	32
strip	1.13	10	10.51	11.38
5 μm gap	0.29	20	5.39	7.57

To study the effect of the gap size, two more hexagonal structures with 50 nm and 150 nm gap sizes were fabricated. Fig. 4.15 compares THz emission of these samples. The smaller gap size increases the DC bias field but it allows less optical transmission to the substrate. Thus the 50 nm gap size hexagonal structure showed the least THz emission. The 150 nm gap size design allows more light. However, the lower DC field has a negative impact on carrier acceleration that results in lower bandwidth. The 100 nm gap size was found as an optimum trade-off to obtain maximum bandwidth and THz radiation amplitude.

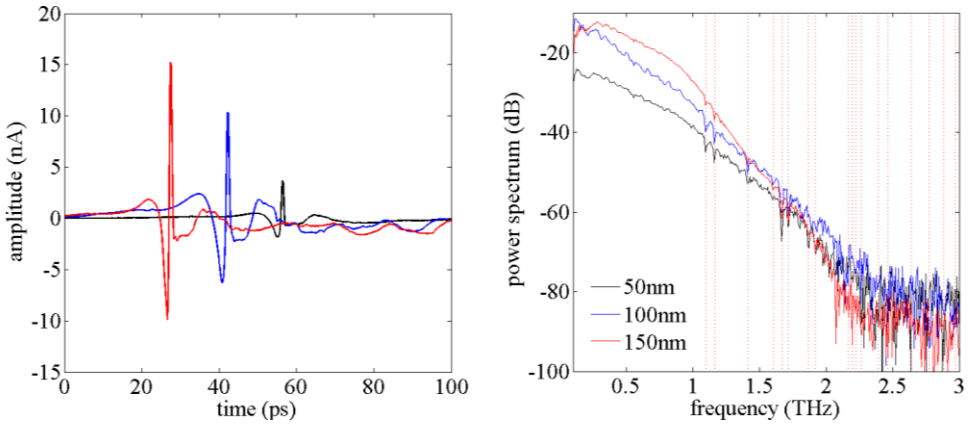

Figure 4.15 THz photocurrent received from 50, 100 and 150 nm gap size hexagonal structures PCA emitters.

Finally, all plasmonic structures were over biased to find thermal breakdown threshold. While the 100 nm gap hexagonal structure was functional up to 18 V_{DC}, the 100 nm slit structure failed at 13 V_{DC}. According to the observations, not all hexagon cells were removed from the surface at the breakdown. This makes plasmonic hexagonal structures more robust than the slit design.

An easy experimental way to prove optical coupling to the substrate is to rotate the polarization of the light and check the reflection from the plasmonic structure. While this is not really effective for hexagonal structures, Fig. 4.16 shows reflection images from a slit structure when polarization of electric field on the surface is vertical (transverse electric TE) or horizontal (transverse magnetic TM).

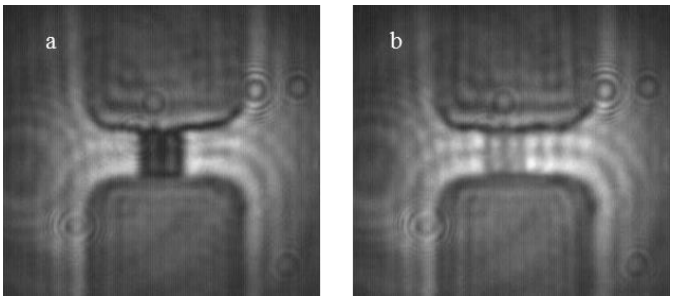

Figure 4.16 Reflection images of a plasmonic slit structure captured with a CMOS camera at 785nm wavelength. (a) polarization is horizontal (b) polarization is vertical.

Variations in reflection means whether the light is coupled effectively to the substrate or not. This also has a strong effect in performance of the PCA in THz-TDS setup. For instance, Fig. 4.17 shows THz photocurrent measured from a plasmonic slit structure fabricated on LT-GaAs i.e. PE-LT-GaAs. The slit structure is designed to absorb 1570 nm wavelength light. Due to the polarization dependence, THz photocurrent goes to zero as the mismatch angle between the electric field of the light and the array reaches 90˚. The figure also shows the superiority of the plasmonic structures in comparison with a large gap dipole in a same experimental condition.

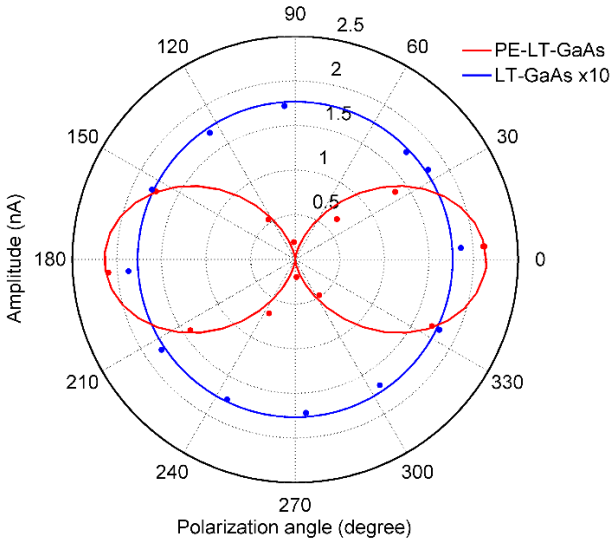

Figure 4.17 THz photocurrent received as a function of laser polarization. Polarization dependency of the plasmonic slit structure (PE-LT-GaAs) is compared with a large gap (5μm) dipole.

In summary, we explained Lumerical FDTD simulations and discussed design criteria for a plasmonic structures. Hexagonal and a slit design plasmonic structures were fabricated and tested in a THz-TDS setup. It was found that the plasmonic structures can enhance THz generation and detection by increasing the localized field and coupling more light into minimum depth of the semiconductor. Covering the active area with Gold nano-structures also increases thermal conductivity, which is essential for safe operation of the PCA at higher optical excitation power. Biased receiver measurements showed that Johnson-Nyquist noise can reduce signal to noise ratio in the time domain THz setup.

Chapter 5 : Optimization of photoconductive materials

5.1. Photoconductive materials for 1550 nm

Although InGaAs is a popular photoconductive material, its low resistivity and long carrier lifetime set a limit in the performance of InGaAs based PCAs in terms of output power and bandwidth. Recent advances in fabrication of InGaAs/InAlAs multi quantum well were successful to overcome the material deficiencies. However, complexity of fabrication increases total cost of these InGaAs based PCAs. Currently InGaAs photoconductive antennas are several times more expensive than comparable LT GaAs devices in the 800 nm window.

Meanwhile LT-GaAs is the only low cost photoconductive material with proven performance in the THz industry that can also absorb 1550 nm light by means of mid-gap Arsenic states [71, 81]. LT-GaAs was not considered as photoconductive material for 1.5 μm excitation because it is almost transparent at this wavelength. Just recently, it has been recognized that LT-GaAs can generate substantial carriers under intense 1.5 μm laser exposure to generate and detect THz waves [87, 161]. The advantage of LT-GaAs is its lower price in comparison with InGaAs, its lower conductivity, and short carrier-lifetime.

Absorption of 1570 nm by an in-house fabricated LT-GaAs was confirmed at the University of Victoria during an experiment in December 2014. This chapter explains initial experimental results and discusses the potential of LT-GaAs as a material of choice for future PCA devices. Following our initial results, several LT-GaAs films were fabricated on GaAs wafers with different Arsenic to Gallium ratios. Moreover, different thicknesses of LT-GaAs were grown and annealed to further study properties of Arsenic defect states at 1570 nm excitation.

5.1.1. Below bandgap absorption of LT-GaAs and experimental results

According to the literature, photo-carrier excitation improves if intensity of the light increases [88]. Therefore, we used plasmonic structures to localize the light inside the minimum depth of LT-GaAs layer. A slit design plasmonic structure was used to cope with poor absorption of LT-GaAs at 1570 nm.

In this experiment, a 2 μm thick LT-GaAs layer with As/Ga ratio of 6.7 was annealed at 630 ^{o}C for 1 minute. The annealing condition was previously obtained and repeated multiple times for optimization of LT-GaAs under 800 nm excitation [93]. 20 μm long dipole antennas were patterned on the surface of LT-GaAs using contact photolithography. A 5 nm Titanium layer followed by a 150 nm Gold layer were deposited according to the recipe explained in Section 3.1.3 over the surface of all samples at the same time.

To make plasmonic structures, an array of 18 slits (490 nm periodicity) was milled through the Gold at the centre of each closed gap dipole using FIB. We call this sample plasmonic-enhanced (PE) LT-GaAs PCA. Fig. 5.1a shows the 2-dimentional field

intensity profile of the plasmonic structure, which is compared with a same size large gap area dipole Fig. 5.1b. The inset is a closer look of the field enhancement under Gold edges in a 100 nm gap and shows a stronger light in comparison with the bulk LT-GaAs material Fig. 5.1b.

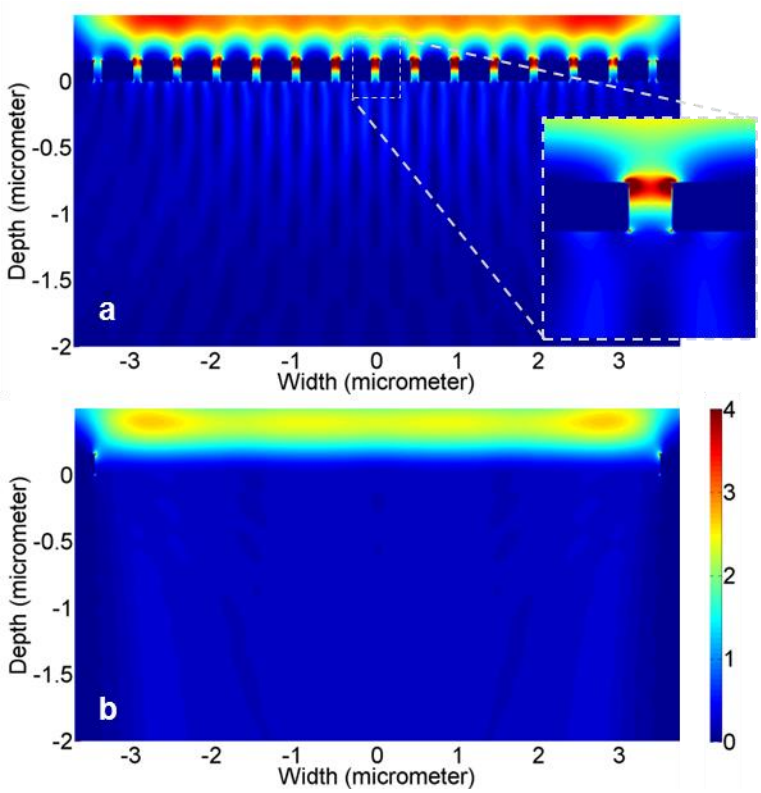

Figure 5.1 Cross section view of a gap are (a) with and (b) without plasmonic structures. Inset shows local intensity increase under the Gold.

Fig. 5.2a and b show diagrams of the THz-TDS setup, which was used to test PCAs as receivers and transmitters respectively. For alignment purposes, we relied on second harmonic generation (SHG) in a periodically poled lithium niobate (PPLN) crystal that was used to drive a commercial LT-GaAs photoconductive switch (BATOP, PCA-40-05-10-800-a). The reason is to ensure a high-bandwidth and high-power THz source/detector on the opposite side for characterization. All devices under test were pumped only with

1570 nm and 80 fs (PolarOnyx - Mercury) laser beam, which was ensured by implementation of dual long-pass filters – Edmund Optics 950 nm dichroic). The commercial sample was biased and chopped at 1 kHz according to its datasheet specifications and the receivers were directly connected to the lock-in amplifier [162].

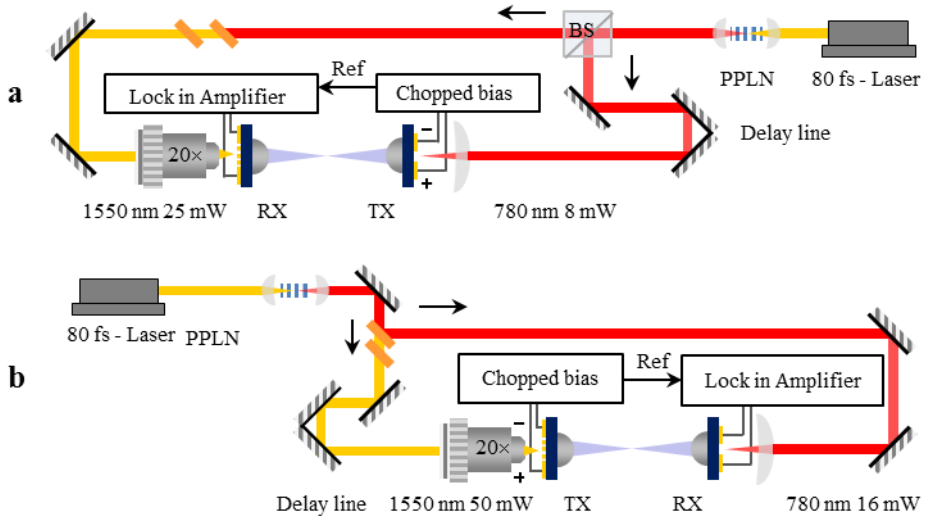

Figure 5.2 Dual beam THz-TDS setups used for characterization of LT-GaAs based PCAs. (a) receiver setup. (b) transmitter setup.

Results of Fig. 5.3 demonstrates that the plasmon-enhanced (PE) LT-GaAs devices outperform existing commercial InGaAs devices (BATOP, PCA-40-05-10-1550-a) as transmitters and receivers, doubling both the bandwidth and power. The number of phot-excited carriers is more important for the transmitter to ensure quick depletion of the gap capacitor in sub picosecond time. Thus, the bandwidth of the transmitter is more vulnerable to absorption of 1570 nm in LT-GaAs. It is expected to obtain 2.5 THz (similar to the receiver results) if more optical power and As/Ga ratio are provided.

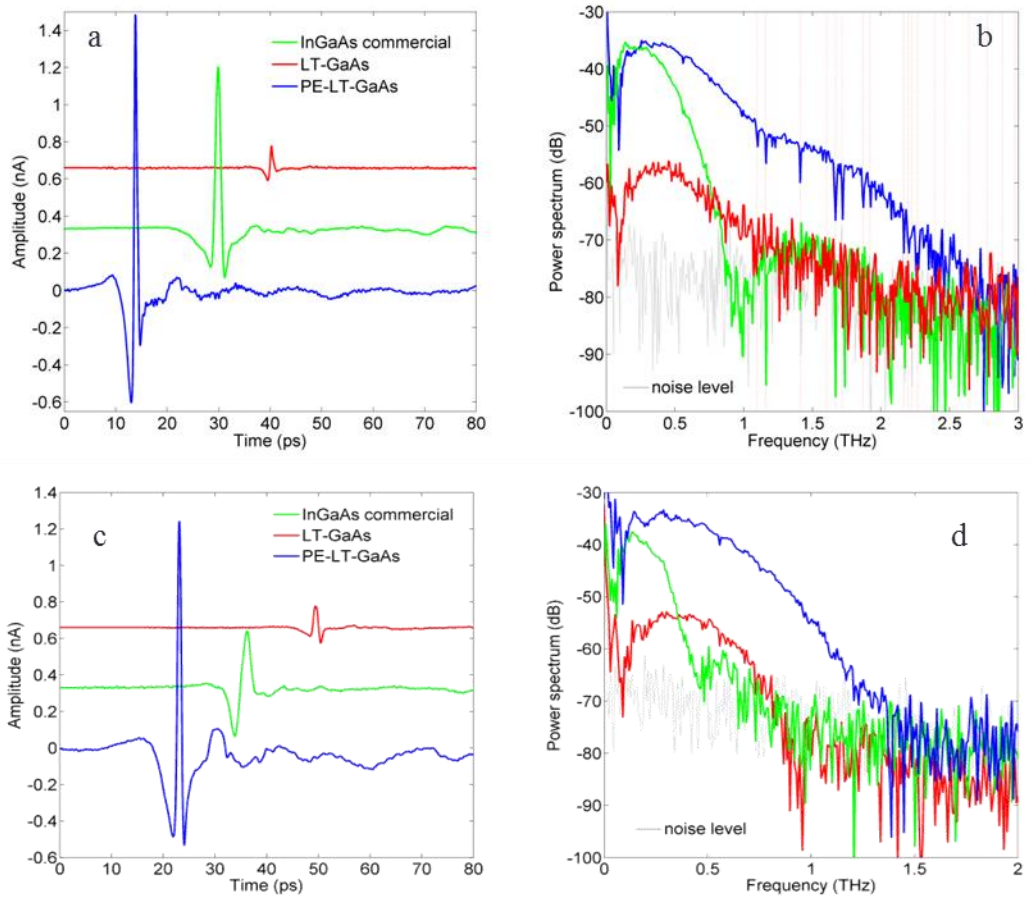

Figure 5.3 (a) THz photocurrents detected by the plasmonic-enhanced LT-GaAs, large gap LT-GaAs dipole and a commercial InGaAs PCAs. (b) power spectrum of the received signals. (c) THz signal radiated by PE-LT-GaAs, large gap LT-GaAs dipole and a commercial InGaAs.

Fig. 5.4 shows THz generation and detection with pure 1570 nm laser beams on both LT-GaAs based PCAs. In this experiment, the LT-GaAs commercial sample (BATOP, PCA-40-05-10-800-a) was used as a transmitter and the PE-LT-GaAs sample was placed at the location of the receiver. First, the THz path was aligned at 780 nm. Then, the PPLN crystal was removed from the laser path and 1570 nm beams were re-aligned to the gap area of both samples. Due to the poor performance of LT-GaAs commercial emitter at

1570 nm, the signal amplitude is low but the experiment demonstrates a fully operational THz-TDS setup with LT-GaAs based PCAs under 1570 nm laser excitation.

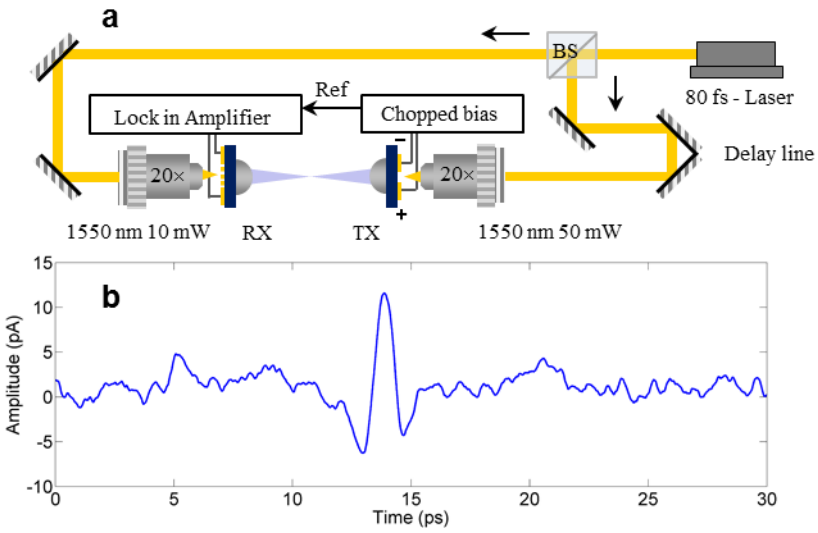

Figure 5.4 Time domain THz current of both LT-GaAs based source and receiver at 1570 nm. Transmitter is a LT-GaAs commercial sample and detector is the PE-LT-GaAs sample.

It is important to note that the PE-LT-GaAs device can handle much higher optical powers. There are two reasons to explain this. First, GaAs is almost transparent at 1550 nm. Second, plasmonic structures can remove heat efficiently from the surface. During a thermal breakdown threshold test, the PE-LT-GaAs was exposed to 200 mW of 1570 nm laser power but did not fail. Fig. 5.5a shows the photocurrent recorded with 1 V_{DC} bias voltage as a function of pump power. Fig. 5.5b shows that unlike the commercial InGaAs sample none of the LT-GaAs PCAs were saturated at normal operation condition (< 25 mW). This indicates that if the pulse broadening produced by the EDFA is compensated, the PE-LT-GaAs PCA can generate much stronger THz signals. Currently, femtosecond lasers have built in amplifiers and dispersion compensators that can reach to half a watt in

output power. Thus, pumping PE-LT-GaAs PCAs with extraordinary optical powers is technologically feasible.

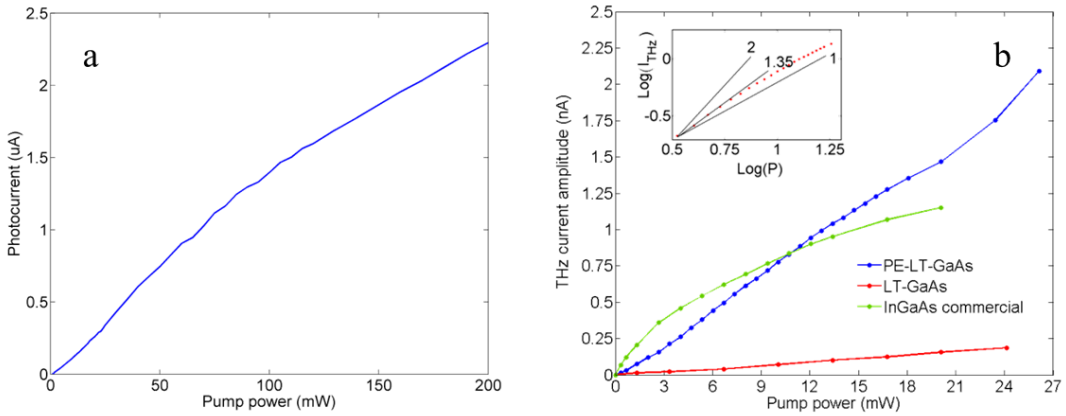

Figure 5.5 Dependency of the photocurrent to the pump power. (a) Photocurrent of the PE-LT-GaAs sample exposed to 1570 nm laser power. (b) Peak to peak THz received photocurrent of three devices that does not show any saturation for LT-GaAs.

Considering all benefits of LT-GaAs, it is possible that PE-LT-GaAs devices can potentially displace all InGaAs based PCAs in the market today. Therefore, the material must be studied in detail to find the optimum growth condition for maximum performance.

5.2. Optimization of LT-GaAs for 1550 nm excitation

Section 3.1 explained how the beam equivalent pressure (BEP) was used to control the incorporation of Arsenic into the LT-GaAs. There are three important parameters involved in growth of the LT-GaAs layer. As/Ga ratio or Arsenic density, material thickness and annealing temperature. For this experiment seven LT-GaAs films were grown on semi-insulating GaAs. Table 5.1 provides specifications of LT-GaAs substrates that were used in this experiment.

Table 5.1 list of LT-GaAs substrates with their growth conditions.

Sample number	Thickness	Growth temperature	As:Ga BEP ratio
R2348	1 μm	230 ^{o}C	15
R2617	2 μm	226 ^{o}C	6.7
R2639	3 μm	230 ^{o}C	3.2
R2640	500 nm	230 ^{o}C	10
R2643	400 nm	230 ^{o}C	20
R2647	450 nm	230 ^{o}C	5
R2648	450 nm	230 ^{o}C	15

Fig. 5.6 compares absorption of as-grown LT-GaAs films as the function of BEP and wavelength for substrates with almost similar thicknesses (r2640, r2643, r2647, r2648).

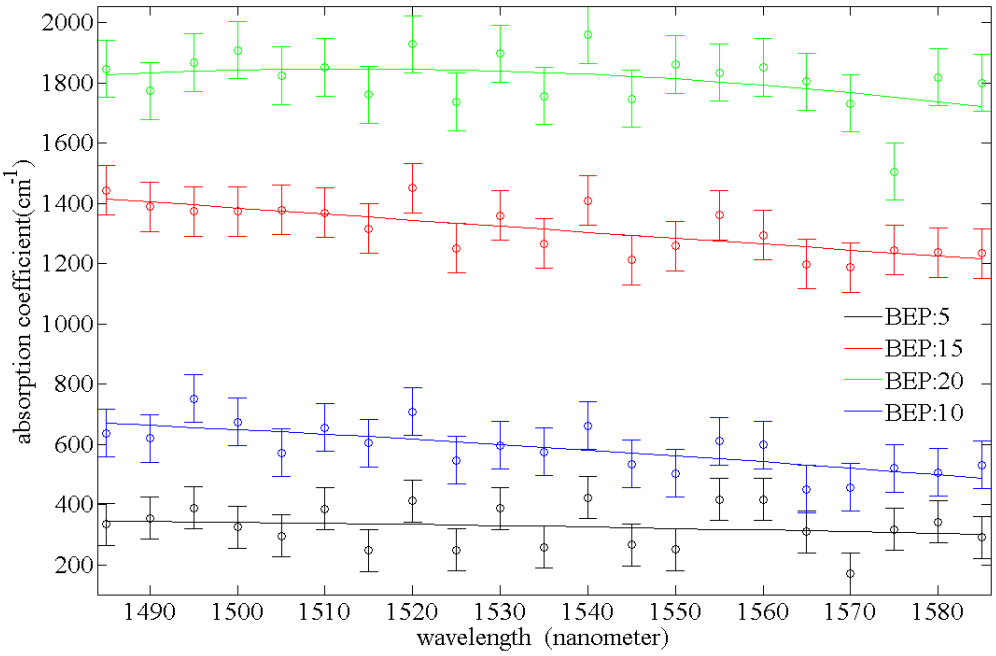

Figure 5.6 Absorption of as-grown LT-GaAs films with different Arsenic to Gallium ratio.

Here, we patterned similar large gap dipole antennas on LT-GaAs substrates listed in Table 5.1. PCAs were tested as receivers at a same time and under a same test condition. Each PCA was exposed to 40 mW of 1570 nm optical power. the THz transmitter was a commercial (BATOP, PCA-40-05-10-800-a), which was pumped with 12 mW from the 780 nm beam.

THz photocurrents were directly measured with a SR830 lock-in amplifier. In the absence of a THz beam, the signal level settled down at -80 dB. Thus, -80 dB was selected as a reference (noise level) to find the bandwidth associated with each measurement.

In the first phase of the tests, large gap (5 µm) dipoles were fabricated and tested on different thicknesses of LT-GaAs substrates. Table 5.2 summarizes the preliminary results with less than ±20% accuracy. Here, we measured current with Keithley 2010 multimeter at 5 V_{DC} bias voltage. I_p is the pure photocurrent generated by light i.e. the subtraction of the currents measured with and without light.

Table 5.2 Photocurrent Ip, dark current Id, and peak-to-peak THz currents of similar PCAs fabricated on different thicknesses of LT-GaAs film. Each sample was annealed and tested to understand the influence of annealing.

	R2647 (0.5 µm) BEP: 5		**R2348 (1 µm) BEP: 15**		**R2617 (2 µm) BEP: 6.7**		**R2639 (3 µm) BEP: 3.2**	
Bias: 5V	As grown	630C 1 min	As grown	630C 1 min	As grown	630C 1 min	As grown	630C 1 min
I_p (µA)	2.6	0.8	6.1	3.37	4.19	0.87	3.8	2.16
I_d (µA)	1.1	0.06	5.09	0.19	14.56	0.15	7.1	1.24
THz (pA)	314	354	336	370	457	670	512	860

It was expected to see a rise in peak-to-peak THz signal amplitude as thickness increases. Because it is not possible to growth a thick (>2 μm) crystalline LT-GaAs with large As/Ga ratio, we used the LT-GaAs substrates with close BEP ratio numbers.

An evident fact here is the nonlinear dependent of THz photocurrent to thickness. The peak to peak THz of the PCA fabricated on r2639 is not 6 times the signal amplitude that was recorded from the PCA on r2647 even with greater BEP. As explained in Chapter 2, carriers generated deep inside the material cannot participate to photocurrent in a sub-picosecond time. Thus, increasing the thickness does not necessarily improve the photoconductive material per dollar e.g. growth of a 3 μm LT-GaAs takes 3 hours or MBE time whereas a 0.5 μm thick LT-GaAs needs only 30 minutes of MBE time.

It is interesting to see that annealing enhances photocurrent. This can be explained by the nature of annealing. As-grown LT-GaAs material has Arsenic defect states distributed between the conduction and valance band. As the temperature rises clusters form defect states closer to the mid-gap that increases the efficiency of the two-step absorption process.

In another experiment, a 1 μm thick LT-GaAs substrate was used to test the effect of annealing temperature. In total 5 samples were made. Results in Table 5.3 indicate that the performance of the mid-gap states degrade at very high temperatures. In fact, material purifies from Arsenic defects as the annealing temperature or time rises. Arsenic clusters move upward and those on the surface escape immediately due to the high vapor pressure of Arsenic. Therefore, annealing at 630 degrees Celsius for 1 min is recommended for an optimum performance of the LT-GaAs.

Table 5.3 Photocurrent Ip, dark current Id, and peak-to-peak THz currents for a same LT-GaAs substrate annealed at different temperatures.

Bias: 5V	**As Grown**	**500 C – 1 min**	**580 C – 1 min**	**630 C – 1 min**	**680 C – 1 min**
I_p (μA)	2.2	2.06	1.21	0.309	0.27
I_d (μA)	4.42	3.24	2.34	0.12	0.68
THz (pA)	313	306	363	454	206

The most important phase of this experiment was the study of Arsenic to Gallium ratio. It is expected to have more photocurrent from an Arsenic rich LT-GaAs. However, extremely high As/Ga BEP ratio makes the material conductive that results in greater dark current and smaller dynamic range. Experimental results in Table 5.4 support the theory and show that the optimum trade-off is for the LT-GaAs with As/Ga BEP ratio of 10 in this list.

Table 5.4 Photocurrent I_p, dark current I_d, and peak-to-peak THz current for as grown LT-GaAs films with different As/Ga BEP ratio. A similar large gap (5 μm) dipole antennas were fabricated on all substrates.

Bias: 5V		**R2647 (BEP:5)**		**R2640 (BEP:10)**		**R2648 (BEP:15)**		**R2643 (BEP:20)**	
I_p (μA)		2.6		2.87		2.76		3.3	
I_d (μA)		1.1		3.41		2.77		2.32	
THz (pA)	BW(THz)	314	1.6	1163	2	100	1.2	106	1.23

Finally, a similar slit design (100 nm gap, 490 nm periodicity) plasmonic structure was milled through the Gold to make three samples on LT-GaAs with As/Ga BEP of 3.2, 6.7, and 20 as shown in Fig. 5.7. PE-LT-GaAs samples were tested as receivers receiving 40 mW of 1570 nm laser power.

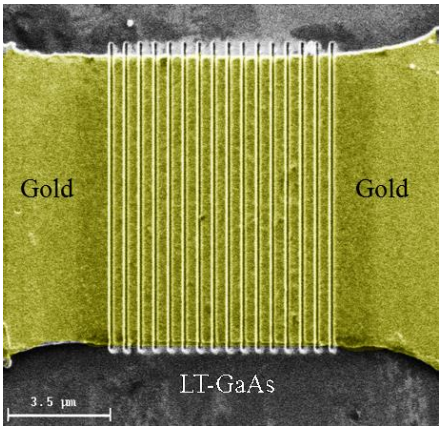

Figure 5.7 Scanning electron microscope (SEM) image of a slit design plasmonic structure with 100 nm gap size and 490 nm periodicity. The thickness of Gold is 150 nm.

According to Table 5.5, the Arsenic rich (BEP:20) LT-GaAs based PCA generates the highest THz signal but its dynamic range and bandwidth shrunk because of its conductivity (see Fig. 5.8). The best trade-off between signal and bandwidth in this experiment belongs to the sample with As/Ga BEP ratio of 6.7.

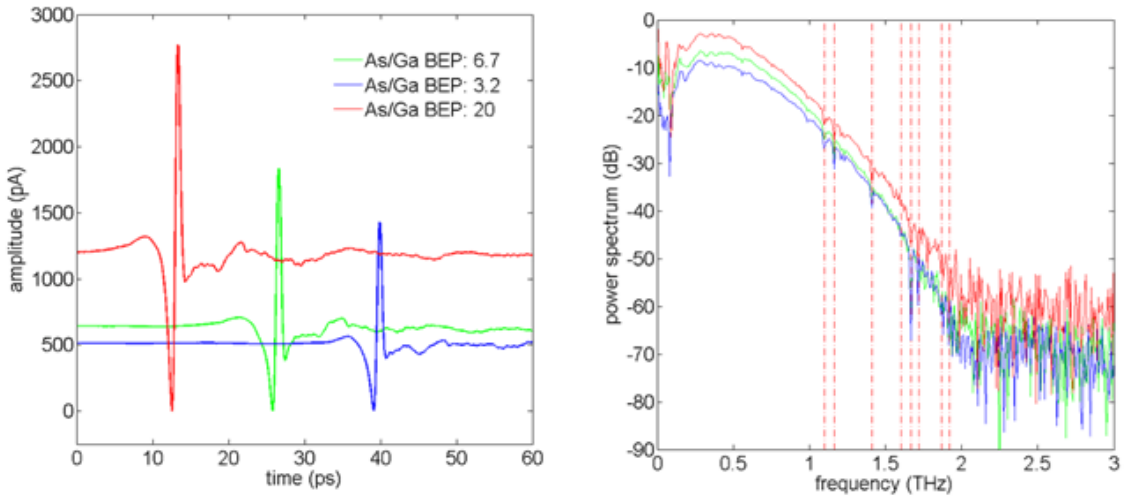

Figure 5.8 THz photocurrent received by plasmonic PCAs fabricated on LT-GaAs substrates with different BEP ratios.

Table 5.5 Photocurrent Ip, dark current Id, and peak-to-peak THz current for different As:Ga BEP ratio LT-GaAs films annealed at 630 ^{o}C for 1 minute with slit design plasmonic structure.

Bias: 0.5V		**R2643 (BEP:20)**		**R2639 (BEP:3.2)**		**R2617 (BEP:6.7)**	
Ip(uA)		0.83		0.3		1.04	
Id(uA)		1.72		0.42		0.73	
THz(pA)	BW(THz)	2771	1.9	1431	2.1	1835	2.15

In conclusion, it was learned that THz signal and bandwidth do not rise linearly with Arsenic density inside the LT-GaAs film. It can be inferred that a thickest possible LT-GaAs film, annealed at 630 ^{o}C for 1 minute with As:Ga BEP ratio between 7 to 9 can potentially results in an optimum performance at 1570 nm excitation.

Chapter 6 : Conclusion and future work

6.1. Conclusions

In this dissertation, enhancement of photoconductive antennas for THz-TDS was studied. The work was divided into three sub-sections. Enhancement of the electrical field, increasing the optical field coupling, and optimizing material with the goal of reducing the cost for THz spectroscopy systems.

Chapter 4 explained how plasmonic structures can help with increasing optical field coupling into the minimum depth of the photoconductive material. The superiority of hexagonal shape plasmonic structures in increasing the local electrical field was also studied in detail. Experiments showed that plasmonic structures can efficiently remove heat from the active area, which increases the bias range and the output power.

Many photoconductive materials were tested in this research such as GaBiAs, InGaAs, GaSb, InP, InAs, and LT-GaAs. Considering that an optimum photoconductive material must have the least dark conductivity, sub-picosecond carrier-lifetime, and high mobility, LT-GaAs was selected as the best fit. Chapter 5 showed how mid-gap states help LT-GaAs to outperform existing InGaAs based PCA and reviewed experimental results. Finally, outcomes of the study on thickness, As/Ga BEP ratio and annealing were explained.

6.2. Contribution of this work to future visions

Main contributions of this work can be summarized below:

- Reviewing operation principle and modeling of THz PCAs both as a transmitter and a receiver.
- Understanding radiation pattern, efficiency, and input impedance of micro-scale THz antennas.
- Comparing and evaluating performances of semiconductor photoconductive material as transmitters and reviewers.
- Explaining fabrication recipes and measurement techniques for THz-TDS setups.
- Studying plasmonic structures and their applications in optical and electrical field enhancement at minimum depth of the photoconductive materials.
- Introducing plasmonic enhanced LT-GaAs technology that exploits Arsenic mid-gap defect states to operate at telecom window.
- Optimizing Arsenic concentration, annealing, and thickness of LT-GaAs to obtain maximum performance at telecom window.

Along with the main achievements and contributions of this work, dozens of projects were defined and explored. For example, feasibility analysis of electro-optical sampling using nonlinear crystals, biasing receivers, field electron emission or third harmonic to generate photocurrent, and study of an oxide layer for reduction of the dark current. Results of each experiment helped to reach the goals of this research.

6.2.1. Future fiber coupled transmitters and receivers

A portable and compact THz-TDS system must be independent of any free space alignment. This vision necessitates fabrication of fiber coupled transceivers. Therefore, next step is to find practical solutions for mounting optical fibers directly on the surface of the PCAs. At this time, many companies have implemented this technology into their THz modules and it should be possible with current facilities at the University of Victoria.

6.2.2. Future waveguide based THz-TDS

Rather than radiating the THz wave from an antenna, the generated THz can be coupled into a waveguide. Waveguide based THz-TDS may offer advantage on packaging and performance. They can be robust against vibration and misalignment because they use fiber-based laser guiding and focusing to the active area and a rigid THz waveguide. The combination of PE-LT-GaAs PCSs and THz waveguides can potentially pave the wave to industrialization of cost effective portable THz systems.

Bibliography

1. Y. Lee, *Principles of terahertz science and technology* (Springer, 2009).

2. S. Preu, G. H. Döhler, S. Malzer, L. J. Wang, and A. C. Gossard,"Tunable, continuous-wave terahertz photomixer sources and applications", J. Appl. Phys. **109**, 061301 (2011).

3. Technische Universität Kaiserslautern, "Terahertz waves - between electronics and optics,"http://www.physik.uni-kl.de/uploads/pics/Bild_01_spectrum_engl.jpg.

4. M. van Exter, C. Fattinger, and D. Grischkowsky,"Terahertz time-domain spectroscopy of water vapor", Opt. Lett. **14**, 1128 (1989).

5. L. Ho, M. Pepper, and P. Taday,"Terahertz spectroscopy: Signatures and fingerprints", Nature Photon. **2**, 541-543 (2008).

6. B. M. Fischer, M. Walther, and P. U. Jepsen,"Far-infrared vibrational modes of DNA components studied by terahertz time-domain spectroscopy", Phys. Med. Biol. **47**, 3807-3814 (2002).

7. X. Fu, H. Wu, X. Xi, and J. Zhou,"Molecular rotation-vibration dynamics of low-symmetric hydrate crystal in the terahertz region", J. Phys. Chem. A. **118**, 333-338 (2014).

8. S. Yu, B. J. Drouin, and J. C. Pearson,"Terahertz spectroscopy of the bending vibrations of acetylene12c2h2", Astrophys. J. **705**, 786-790 (2009).

9. B. B. Hu, and M. C. Nuss,"Imaging with terahertz waves", Opt. Lett. **20**, 1716-1718 (1995).

10. P. U. Jepsen, D. G. Cooke, and M. Koch,"Terahertz spectroscopy and imaging - modern techniques and applications", Laser Photonics Rev. **5**, 124-166 (2011).

11. D. M. Mittleman, M. Gupta, R. Neelamani, R. G. Baraniuk, J. V. Rudd, and M. Koch,"Recent advances in terahertz imaging", Appl. Phys. B **68**, 1085-1094 (1999).

12. K. Serita, S. Mizuno, H. Murakami, I. Kawayama, Y. Takahashi, M. Yoshimura, Y. Mori, J. Darmo, and M. Tonouchi,"Scanning laser terahertz near-field imaging system", Opt. Express **20**, 12959-12965 (2012).

13. Y. C. Shen, T. Lo, P. F. Taday, B. E. Cole, W. R. Tribe, and M. C. Kemp,"Detection and identification of explosives using terahertz pulsed spectroscopic imaging", Appl. Phys. Lett. **86**, 241116 (2005).

14. S. L. Dexheimer, *Terahertz spectroscopy: Principles and applications* (CRC, 2008).

15. D. Doyle, G. Pilbratt, and J. Tauber,"The herschel and planck space telescopes", Proc. IEEE **97**, 1403-1411 (2009).

16. M. J. Molina, and F. S. Rowland,"Stratospheric sink for chlorofluoromethanes: Chlorine atomc-atalysed destruction of ozone", Nature **249**, 810-812 (1974).

17. K. Moon, H. Park, J. Kim, Y. Do, S. Lee, G. Lee, H. Kang, and H. Han,"Subsurface nanoimaging by broadband terahertz pulse near-field microscopy", Nano Lett. **15**, 549-552 (2015).

18. K. Kawase, Y. Ogawa, Y. Watanabe, and H. Inoue,"Non-destructive terahertz imaging of illicit drugs using spectral fingerprints", Opt. Express **11**, 2549-2554 (2003).

19. C. Yu, S. Fan, Y. Sun, and E. Pickwell-Macpherson,"The potential of terahertz imaging for cancer diagnosis: A review of investigations to date", Quant. Imaging Med. Surg. **2**, 33-45 (2012).

20. T. Inagaki, I. D. Hartley, S. Tsuchikawa, and M. Reid,"Prediction of oven-dry density of wood by time-domain terahertz spectroscopy", Holzforschung **68** (2014).

21. C. Jansen, S. Wietzke, O. Peters, M. Scheller, N. Vieweg, M. Salhi, N. Krumbholz, C. Jordens, T. Hochrein, and M. Koch,"Terahertz imaging: Applications and perspectives", Appl. Opt. **49**, E48-57 (2010).

22. Online article from Toptica,"Terahertz applications - hydration monitoring".

23. Online article from advancedphotonix, "Thz security imaging ".

24. M. H. Arbab, D. P. Winebrenner, T. C. Dickey, A. Chen, M. B. Klein, and P. D. Mourad,"Terahertz spectroscopy for the assessment of burn injuries in vivo", J. Biomed. Opt. **18**, 077004 (2013).

25. N. N. Zinov'ev, A. F. Fitzgerald, S. M. Strafford, D. J. Wood, F. A. Carmichael, R. E. Miles, M. A. Smith, and J. M. Chamberlain,"Identification of tooth decay using terahertz imaging and spectroscopy", J. Infrared Millimeter Waves, 13-14 (2002).

26. T. Idehara, T. Saito, I. Ogawa, S. Mitsudo, Y. Tatematsu, and S. Sabchevski,"The potential of the gyrotrons for development of the sub-terahertz and the terahertz

frequency range — a review of novel and prospective applications", Thin Solid Films **517**, 1503-1506 (2008).

27. M. Mukherjee, N. Mazumder, S. K. Roy, and K. Goswami,"Gan impatt diode: A photo-sensitive high power terahertz source", Semicond. Sci. Technol. **22**, 1258-1267 (2007).

28. M. Tonouchi,"Cutting-edge terahertz technology", Nature Photon. **1**, 97-105 (2007).

29. B. Heshmat Dehkordi, "Enhancing terahertz photoconductive switches using nanotechnology," (University of Victoria 2013).

30. J. R. Mayes, "Analytical modelling of a linear gaas photoconductive switch for short pulse excitation," presented at the 12th IEEE International Pulsed Power Conference (1999).

31. P. U. Jepsen, R. H. Jacobsen, and S. R. Keiding,"Generation and detection of terahertz pulses from biased semiconductor antennas", J. Opt. Soc. Am. B **13**, 2424-2436 (1996).

32. M. Tani, S. Matsuura, K. Sakai, and S.-i. Nakashima,"Emission characteristics of photoconductive antennas based on low-temperature-grown gaas and semi-insulating gaas", Appl. Opt. **36**, 7853-7859 (1997).

33. N. Wang, and M. Jarrahi,"Noise analysis of photoconductive terahertz detectors", J. Infrared Millim. Terahertz Waves **34**, 519-528 (2013).

34. K. Sala, G. Kenney-Wallace, and G. Hall,"Cw autocorrelation measurements of picosecond laser pulses", IEEE J. Quantum Electron. **16**, 990-996 (1980).

35. E. Castro-Camus, J. Lloyd-Hughes, and M. Johnston,"Three-dimensional carrier-dynamics simulation of terahertz emission from photoconductive switches", Phys. Rev. B **71**, 195301 (2005).

36. I. S. Gregory, C. Baker, W. R. Tribe, I. V. Bradley, M. J. Evans, E. H. Linfield, A. G. Davies, and M. Missous,"Optimization of photomixers and antennas for continuous-wave terahertz emission", IEEE J. Quantum Electron. **41**, 717-728 (2005).

37. E. R. Brown, F. W. Smith, and K. A. McIntosh,"Coherent millimeter-wave generation by heterodyne conversion in low-temperature-grown gaas photoconductors", J. Appl. Phys. **73**, 1480 (1993).

38. S. Verghese, K. A. McIntosh, and E. R. Brown,"Highly tunable fiber-coupled photomixers with coherent terahertz output power", IEEE Trans. Microwave Theory Tech. **45**, 1301-1309 (1997).

39. C. W. Berry, M. R. Hashemi, S. Preu, H. Lu, A. C. Gossard, and M. Jarrahi,"High power terahertz generation using 1550 nm plasmonic photomixers", Appl. Phys. Lett. **105**, 011121 (2014).

40. F. Nakajima, T. Furuta, and H. Ito, "High-power terahertz-wave generation from a resonant-antenna-integrated uni-traveling-carrier photodiode," presented at the IEEE International Topical Meeting on Microwave Photonics (2004).

41. A. Nahata, A. S. Weling, and T. F. Heinz,"A wideband coherent terahertz spectroscopy system using optical rectification and electro-optic sampling", Appl. Phys. Lett. **69**, 2321 (1996).

42. P. Y. Han, and X. C. Zhang,"Free-space coherent broadband terahertz time-domain spectroscopy", Meas. Sci. Technol. **12**, 1747-1756 (2001).

43. R. Huber, A. Brodschelm, F. Tauser, and A. Leitenstorfer,"Generation and field-resolved detection of femtosecond electromagnetic pulses tunable up to 41 thz", Appl. Phys. Lett. **76**, 3191 (2000).

44. D. Auston, K. Cheung, J. Valdmanis, and D. Kleinman,"Cherenkov radiation from femtosecond optical pulses in electro-optic media", Phys. Rev. Lett. **53**, 1555-1558 (1984).

45. D. H. Auston, and K. P. Cheung,"Coherent time-domain far-infrared spectroscopy", J. Opt. Soc. Am. B **2**, 606 (1985).

46. X. C. Zhang, X. F. Ma, Y. Jin, T. M. Lu, E. P. Boden, P. D. Phelps, K. R. Stewart, and C. P. Yakymyshyn,"Terahertz optical rectification from a nonlinear organic crystal", Appl. Phys. Lett. **61**, 3080 (1992).

47. Y. J. Ding, and I. B. Zotova,"Second-order nonlinear optical materials for ecient generation and amplication of temporally-coherent and narrow-linewidth terahertz waves", Opt. Quantum Electron. **32**, 531-552 (2000).

48. Z. Zhao, A. Schwagmann, F. Ospald, D. C. Driscoll, H. Lu, A. C. Gossard, and J. H. Smet,"Thickness dependence of the terahertz response in (110)-oriented gaas crystals for electro-optic sampling at 1.55 microm", Opt. Express **18**, 15956-15963 (2010).

49. A. Nahata, J. T. Yardley, and T. F. Heinz,"Free-space electro-optic detection of continuous-wave terahertz radiation", Appl. Phys. Lett. **75**, 2524 (1999).

50. C. W. Berry, M. R. Hashemi, and M. Jarrahi,"Generation of high power pulsed terahertz radiation using a plasmonic photoconductive emitter array with logarithmic spiral antennas", Appl. Phys. Lett. **104**, 081122 (2014).

51. I. S. Gregory, W. R. Tribe, B. E. Cole, M. J. Evans, E. H. Linfield, A. G. Davies, and M. Missous,"Resonant dipole antennas for continuous-wave terahertz photomixers", Appl. Phys. Lett. **85**, 1622 (2004).

52. H. Tanoto, J. H. Teng, Q. Y. Wu, M. Sun, Z. N. Chen, S. A. Maier, B. Wang, C. C. Chum, G. Y. Si, A. J. Danner, and S. J. Chua,"Greatly enhanced continuous-wave terahertz emission by nano-electrodes in a photoconductive photomixer", Nature Photon. **6**, 121-126 (2012).

53. C. A. Balanis, *Antenna theory analysis and design* (JOHN WILEY & SONS, 2005).

54. M. Kominami, D. Pozar, and D. Schaubert,"Dipole and slot elements and arrays on semi-infinite substrates", IEEE Trans. Antennas Propag. **33**, 600-607 (1985).

55. S. M. Duffy, S. Verghese, A. McIntosh, A. Jackson, A. C. Gossard, and S. Matsuura,"Accurate modeling of dual dipole and slot elements used with photomixers for coherent terahertz output power", IEEE Trans. Microwave Theory Tech. **49**, 1032-1038 (2001).

56. T. K. Nguyen, T. A. Ho, H. Han, and I. Park,"Numerical study of self-complementary antenna characteristics on substrate lenses at terahertz frequency", J. Infrared Millim. Terahertz Waves **33**, 1123-1137 (2012).

57. A. Krotkus, K. Bertulis, R. Adomavičius, V. Pačebutas, and A. Geižutis,"Semiconductor materials for ultrafast optoelectronic applications", Lith. J. Phys. **49**, 359-372 (2009).

58. S. A. Jensen, R. Ulbricht, A. Narita, X. Feng, K. Mullen, T. Hertel, D. Turchinovich, and M. Bonn,"Ultrafast photoconductivity of graphene nanoribbons and carbon nanotubes", Nano Lett. **13**, 5925-5930 (2013).

59. X. He, N. Fujimura, J. M. Lloyd, K. J. Erickson, A. A. Talin, Q. Zhang, W. Gao, Q. Jiang, Y. Kawano, R. H. Hauge, F. Leonard, and J. Kono,"Carbon nanotube terahertz detector", Nano Lett. **14**, 3953-3958 (2014).

60. J. J. H. Pijpers, R. Ulbricht, K. J. Tielrooij, A. Osherov, Y. Golan, C. Delerue, G. Allan, and M. Bonn,"Assessment of carrier-multiplication efficiency in bulk pbse and pbs", Nat. Phys. **5**, 811-814 (2009).

61. G. E. Stillman, C. M. Wolfe, and J. O. Dimmock,"Hall coefficient factor for polar mode scattering in n-type gaas", J. Phys. Chem. Solids **31**, 1199-1204 (1970).

62. B. B. Hu, X. Zhang, and D. H. Auston,"Terahertz radiation induced by subband-gap femtosecond optical excitation of gaas", Phys. Rev. Lett. **67**, 2709-2712 (1991).

63. H. Nyquist,"Thermal agitation of electric charge in conductors", Phys. Rev. **32**, 110-113 (1928).

64. P. J. Hale, J. Madeo, C. Chin, S. S. Dhillon, J. Mangeney, J. Tignon, and K. M. Dani,"20 thz broadband generation using semi-insulating gaas interdigitated photoconductive antennas", Opt. Express **22**, 26358-26364 (2014).

65. K.-T. Tsen, J. Lloyd-Hughes, E. Castro-Camus, M. D. Fraser, H. H. Tan, C. Jagadish, M. B. Johnston, J.-J. Song, and H. Jiang,"carrier dynamics in ion-implanted semiconductors studied by simulation and observation of terahertz emission", **6118**, 61180K-61111 (2006).

66. M. Mikulics,"Photomixers fabricated on nitrogen-ion-implanted gaas", Appl. Phys. Lett. **87**, 041106 (2005).

67. T.-A. Liu, M. Tani, M. Nakajima, M. Hangyo, and C.-L. Pan,"Ultrabroadband terahertz field detection by photoconductive antennas based on multi-energy arsenic-ion-implanted gaas and semi-insulating gaas", Appl. Phys. Lett. **83**, 1322 (2003).

68. T.-A. Liu, M. Tani, and C.-L. Pan,"Thz radiation emission properties of multienergy arsenic-ion-implanted gaas and semi-insulating gaas based photoconductive antennas", J. Appl. Phys. **93**, 2996 (2003).

69. M. Kaminska, Z. Liliental-Weber, E. R. Weber, T. George, J. B. Kortright, F. W. Smith, B. Y. Tsaur, and A. R. Calawa,"Structural properties of as-rich gaas grown by molecular beam epitaxy at low temperatures", Appl. Phys. Lett. **54**, 1881 (1989).

70. D. C. Look, D. C. Walters, M. O. Manasreh, J. R. Sizelove, C. E. Stutz, and K. R. Evans,"Anomalous hall-effect results in low-temperature molecular-beam-epitaxial gaas: Hopping in a denseel2-like band", Phys. Rev. B **42**, 3578-3581 (1990).

71. K. Krambrock, M. Linde, J. M. Spaeth, D. C. Look, D. Bliss, and W. Walukiewicz,"Arsenic antisite-related defects in low-temperature mbe grown gaas", Semicond. Sci. Technol. **7**, 1037-1041 (1992).

72. H. Shen, F. C. Rong, R. Lux, J. Pamulapati, M. Taysing-Lara, M. Dutta, E. H. Poindexter, L. Calderon, and Y. Lu,"Fermi level pinning in low-temperature molecular beam epitaxial gaas", Appl. Phys. Lett. **61**, 1585 (1992).

73. D. C. Look, Z. Q. Fang, H. Yamamoto, J. R. Sizelove, M. G. Mier, and C. E. Stutz,"Deep traps in molecular-beam-epitaxial gaas grown at low temperatures", J. Appl. Phys. **76**, 1029 (1994).

74. J. Störmer, W. Triftshäuser, N. Hozhabri, and K. Alavi,"Vacancy-type defects in molecular beam epitaxy low temperature grown gaas, a positron beam lifetime study", Appl. Phys. Lett. **69**, 1867 (1996).

75. A. J. Lochtefeld, M. R. Melloch, J. C. P. Chang, and E. S. Harmon,"The role of point defects and arsenic precipitates in carrier trapping and recombination in low-temperature grown gaas", Appl. Phys. Lett. **69**, 1465 (1996).

76. J. K. Luo, H. Thomas, D. V. Morgan, and D. Westwood,"Transport properties of gaas layers grown by molecular beam epitaxy at low temperature and the effects of annealing", J. Appl. Phys. **79**, 3622 (1996).

77. S. Rihani, R. Faulks, H. E. Beere, I. Farrer, M. Evans, D. A. Ritchie, and M. Pepper,"Enhanced terahertz emission from a multilayered low temperature grown gaas structure", Appl. Phys. Lett. **96**, 091101 (2010).

78. M. Tani, K. Sakai, and H. Mimura,"Ultrafast photoconductive detectors based on semi-insulating gaas and inp", Jpn. J. Appl. Phys. **36**, L1175-L1178 (1997).

79. I. S. Gregory, C. Baker, W. R. Tribe, M. J. Evans, H. E. Beere, E. H. Linfield, A. G. Davies, and M. Missous,"High resistivity annealed low-temperature gaas with 100 fs lifetimes", Appl. Phys. Lett. **83**, 4199 (2003).

80. S. Kono, K. Sakai, and M. Tani,"Coherent detection of mid-infrared radiation up to 60 thz with an lt-gaas photoconductive antenna", IEEE Proceedings - Optoelectronics **149**, 105-109 (2002).

81. S. U. Dankowski, D. Streb, M. Ruff, P. Kiesel, M. Kneissl, B. Knüpfer, G. H. Döhler, U. D. Keil, C. B. Sørenson, and A. K. Verma,"Above band gap absorption spectra of the arsenic antisite defect in low temperature grown gaas and algaas", Appl. Phys. Lett. **68**, 37 (1996).

82. R. M. Feenstra, J. M. Woodall, and G. D. Pettit,"Observation of bulk defects by scanning tunneling microscopy and spectroscopy: Arsenic antisite defects in gaas", Phys. Rev. Lett. **71**, 1176-1179 (1993).

83. D. V. Lang,"Study of electron traps in n-gaas grown by molecular beam epitaxy", J. Appl. Phys. **47**, 2558 (1976).

84. M. C. Beard, G. M. Turner, and C. A. Schmuttenmaer,"Subpicosecond carrier dynamics in low-temperature grown gaas as measured by time-resolved terahertz spectroscopy", J. Appl. Phys. **90**, 5915-5923 (2001).

85. I. S. Gregory, C. M. Tey, A. G. Cullis, M. J. Evans, H. E. Beere, and I. Farrer,"Two-trap model for carrier lifetime and resistivity behavior in partially annealed gaas grown at low temperature", Phys. Rev. B **73** (2006).

86. O. Svelto, S. D. Silvestri, and G.Oenardo, *Ultrafast processes in spectroscopy* (Springer, 1995).

87. M. Tani, K.-S. Lee, and X. C. Zhang,"Detection of terahertz radiation with low-temperature-grown gaas-based photoconductive antenna using 1.55 μm probe", Appl. Phys. Lett. **77**, 1396 (2000).

88. T. Kataoka, K. Kajikawa, J. Kitagawa, Y. Kadoya, and Y. Takemura,"Improved sensitivity of terahertz detection by gaas photoconductive antennas excited at 1560 nm", Appl. Phys. Lett. **97**, 201110 (2010).

89. M. D. Sturge,"Optical absorption of gallium arsenide between 0.6 and 2.75 ev", Phys. Rev. **127**, 768-773 (1962).

90. T. Fuyuki, M. Ito, K. Kado, and M. Yoshimoto,"Localized states in gaas1-xbix and gaas/gaas1-xbix heterointerface", J Soc Mater Sci. Japan, **62**, 672-678 (2013).

91. B. Čechavičius, R. Adomavičius, A. Koroliov, and A. Krotkus,"Thermal annealing effect on photoexcited carrier dynamics in gabixas1−x", Semicond. Sci. Technol. **26**, 085033 (2011).

92. V. Pačebutas, A. Bičiūnas, S. Balakauskas, A. Krotkus, G. Andriukaitis, D. Lorenc, A. Pugžlys, and A. Baltuška,"Terahertz time-domain-spectroscopy system based on femtosecond yb:Fiber laser and gabias photoconducting components", Appl. Phys. Lett. **97**, 031111 (2010).

93. B. Heshmat, M. Masnadi-Shirazi, R. B. Lewis, J. Zhang, T. Tiedje, R. Gordon, and T. E. Darcie,"Enhanced terahertz bandwidth and power from gaasbi-based sources", Adv. Opt. Mater. **1**, 714-719 (2013).

94. V. PacÌŒebutas, K. Bertulis, A. BicÌŒiuÌ„nas, and A. n. Krotkus,"Low-temperature mbe-grown gabias layers for terahertz optoelectronic applications", Phys. Status Solidi C **6**, 2649-2651 (2009).

95. K. Liu, J. Xu, T. Yuan, and X. C. Zhang,"Terahertz radiation from inas induced by carrier diffusion and drift", Phys. Rev. B **73** (2006).

96. P. Gu, M. Tani, S. Kono, K. Sakai, and X. C. Zhang,"Study of terahertz radiation from inas and insb", J. Appl. Phys. **91**, 5533 (2002).

97. J. N. Heyman, P. Neocleous, D. Hebert, P. A. Crowell, T. Müller, and K. Unterrainer,"Terahertz emission from gaas and inas in a magnetic field", Phys. Rev. B **64** (2001).

98. A. C. Irvine, and D. W. Palmer,"First observation of the el2 lattice defect in indium gallium arsenide grown by molecular-beam epitaxy", Phys. Rev. Lett. **68**, 2168-2171 (1992).

99. B. Grandidier, H. Chen, R. M. Feenstra, D. T. McInturff, P. W. Juodawlkis, and S. E. Ralph,"Scanning tunneling microscopy and spectroscopy of arsenic antisites in low temperature grown ingaas", Appl. Phys. Lett. **74**, 1439 (1999).

100. H. Künzel, J. Böttcher, R. Gibis, and G. Urmann,"Material properties of ga0.47in0.53as grown on inp by low-temperature molecular beam epitaxy", Appl. Phys. Lett. **61**, 1347 (1992).

101. M. Suzuki, and M. Tonouchi,"Fe-implanted ingaas photoconductive terahertz detectors triggered by 1.56μm femtosecond optical pulses", Appl. Phys. Lett. **86**, 163504 (2005).

102. C. D. Wood, O. Hatem, J. E. Cunningham, E. H. Linfield, A. G. Davies, P. J. Cannard, M. J. Robertson, and D. G. Moodie,"Terahertz emission from metal-organic chemical vapor deposition grown fe:Ingaas using 830 nm to 1.55μm excitation", Appl. Phys. Lett. **96**, 194104 (2010).

103. A. Schwagmann, Z. Y. Zhao, F. Ospald, H. Lu, D. C. Driscoll, M. P. Hanson, A. C. Gossard, and J. H. Smet,"Terahertz emission characteristics of eras:Ingaas-based photoconductive antennas excited at 1.55μm", Appl. Phys. Lett. **96**, 141108 (2010).

104. F. Ospald, D. Maryenko, K. von Klitzing, D. C. Driscoll, M. P. Hanson, H. Lu, A. C. Gossard, and J. H. Smet,"1.55μm ultrafast photoconductive switches based on eras:Ingaas", Appl. Phys. Lett. **92**, 131117 (2008).

105. B. Globisch, R. J. B. Dietz, D. Stanze, T. Göbel, and M. Schell,"Carrier dynamics in beryllium doped low-temperature-grown ingaas/inalas", Appl. Phys. Lett. **104**, 172103 (2014).

106. A. Takazato, M. Kamakura, T. Matsui, J. Kitagawa, and Y. Kadoya,"Detection of terahertz waves using low-temperature-grown ingaas with 1.56μm pulse excitation", Appl. Phys. Lett. **90**, 101119 (2007).

107. R. J. Dietz, M. Gerhard, D. Stanze, M. Koch, B. Sartorius, and M. Schell,"Thz generation at 1.55 microm excitation: Six-fold increase in thz conversion efficiency by separated photoconductive and trapping regions", Opt. Express **19**, 25911-25917 (2011).

108. B. Sartorius, H. Roehle, H. Künzel, J. Böttcher, M. Schlak, D. Stanze, H. Venghaus, and M. Schell,"All-fiber terahertz time-domain spectrometer operating at 1.5 μm telecom wavelengths", Opt. Express **16**, 9565 (2008).

109. Y. Chen, S. S. Prabhu, S. E. Ralph, and D. T. McInturff,"Trapping and recombination dynamics of low-temperature-grown ingaas/inalas multiple quantum wells", Appl. Phys. Lett. **72**, 439 (1998).

110. H. Roehle, R. J. Dietz, H. J. Hensel, J. Bottcher, H. Kunzel, D. Stanze, M. Schell, and B. Sartorius,"Next generation 1.5 microm terahertz antennas: Mesa-structuring of ingaas/inalas photoconductive layers", Opt. Express **18**, 2296-2301 (2010).

111. D. Stanze, A. Deninger, A. Roggenbuck, S. Schindler, M. Schlak, and B. Sartorius,"Compact cw terahertz spectrometer pumped at 1.5 μm wavelength", J Infrared Millim. Terahertz Waves **32**, 225-232 (2010).

112. R. H. Ritchie,"Plasma losses by fast electrons in thin films", Phys. Rev. **106**, 874-881 (1957).

113. B. Heshmat, H. Pahlevaninezhad, Y. Pang, M. Masnadi-Shirazi, R. Burton Lewis, T. Tiedje, R. Gordon, and T. E. Darcie,"Nanoplasmonic terahertz photoconductive switch on gaas", Nano Lett. **12**, 6255-6259 (2012).

114. C. W. Berry, and M. Jarrahi,"Terahertz generation using plasmonic photoconductive gratings", New J. Phys. **14**, 105029 (2012).

115. T. W. Ebbesen, H. J. Lezec, H. F. Ghaemi, T. Thio, and P. A. Wolff,"Extraordinary optical transmission through sub-wavelength hole arrays", Nature **391**, 667-669 (1998).

116. J. Zhang, and L. Zhang,"Nanostructures for surface plasmons", Adv. Opt. Photonics **4**, 157 (2012).

117. M. Fehrenbacher, S. Winnerl, H. Schneider, J. Doring, S. C. Kehr, L. M. Eng, Y. Huo, O. G. Schmidt, K. Yao, Y. Liu, and M. Helm,"Plasmonic superlensing in doped gaas", Nano Lett. **15**, 1057-1061 (2015).

118. N. P. Hylton, X. F. Li, V. Giannini, K. H. Lee, N. J. Ekins-Daukes, J. Loo, D. Vercruysse, P. Van Dorpe, H. Sodabanlu, M. Sugiyama, and S. A. Maier,"Loss mitigation in plasmonic solar cells: Aluminium nanoparticles for broadband photocurrent enhancements in gaas photodiodes", Sci. Rep. **3**, 2874 (2013).

119. J. Y. Kim, B. J. Kang, J. Park, Y. M. Bahk, W. T. Kim, J. Rhie, H. Jeon, F. Rotermund, and D. S. Kim,"Terahertz quantum plasmonics of nanoslot antennas in nonlinear regime", Nano Lett. **15**, 6683-6688 (2015).

120. J. Lee, S. Mubeen, X. Ji, G. D. Stucky, and M. Moskovits,"Plasmonic photoanodes for solar water splitting with visible light", Nano Lett. **12**, 5014-5019 (2012).

121. P. N. Melentiev, A. E. Afanasiev, A. A. Kuzin, A. S. Baturin, and V. I. Balykin,"Giant optical nonlinearity of a single plasmonic nanostructure", Opt. Express **21**, 13896-13905 (2013).

122. D. M. Mittleman,"Frontiers in terahertz sources and plasmonics", Nature Photon. **7**, 666-669 (2013).

123. S. Palomba, M. Danckwerts, and L. Novotny,"Nonlinear plasmonics with gold nanoparticle antennas", J. Opt. A-Pure Appl. Op. **11**, 114030 (2009).

124. J. A. Schuller, E. S. Barnard, W. Cai, Y. C. Jun, J. S. White, and M. L. Brongersma,"Plasmonics for extreme light concentration and manipulation", Nature materials **9**, 193-204 (2010).

125. O. Benson, "Plasmonics," in *Elements of nanophotonics,* Humboldt University of Berlin, (2009).

126. D. Wu, N. Fang, C. Sun, X. Zhang, W. J. Padilla, D. N. Basov, D. R. Smith, and S. Schultz,"Terahertz plasmonic high pass filter", Appl. Phys. Lett. **83**, 201 (2003).

127. F. Kneubuhl,"Diffraction grating spectroscopy", Appl. Opt. **8**, 505-519 (1969).

128. C.-L. Chang, G. Acharya, and C. A. Savran,"In situ assembled diffraction grating for biomolecular detection", Appl. Phys. Lett. **90**, 233901 (2007).

129. M. Okai, T. Tsuchiya, K. Uomi, N. Chinone, and T. Harada,"Corrugation-pitch modulated mqw-dfb lasers with narrow spectral linewidth", IEEE J. Quantum Electron. **27**, 1767-1772 (1991).

130. G. Veronis, Ş. E. Kocabaş, D. A. B. Miller, and S. Fan,"Modeling of plasmonic waveguide components and networks", J. Comput. Theor. Nanosci. **6**, 1808-1826 (2009).

131. D. K. Gramotnev, and S. I. Bozhevolnyi,"Nanofocusing of electromagnetic radiation", Nature Photon. **8**, 13-22 (2013).

132. S. A. Maier, S. R. Andrews, L. Martin-Moreno, and F. J. Garcia-Vidal,"Terahertz surface plasmon-polariton propagation and focusing on periodically corrugated metal wires", Phys. Rev. Lett. **97**, 176805 (2006).

133. H. Aouani, J. Wenger, D. Gerard, H. Rigneault, E. Devaux, T. W. Ebbesen, F. Mahdavi, T. Xu, and S. Blair,"Crucial role of the adhesion layer on the plasmonic fluorescence enhancement", ACS nano **3**, 2043-2048 (2009).

134. A. Jooshesh, L. Smith, M. Masnadi-Shirazi, V. Bahrami-Yekta, T. Tiedje, T. E. Darcie, and R. Gordon,"Nanoplasmonics enhanced terahertz sources", Opt. Express **22**, 27992-28001 (2014).

135. S. G. Park, K. H. Jin, M. Yi, J. C. Ye, J. Ahn, and K. H. Jeong,"Enhancement of terahertz pulse emission by optical nanoantenna", ACS nano **6**, 2026-2031 (2012).

136. C. W. Berry, N. Wang, M. R. Hashemi, M. Unlu, and M. Jarrahi,"Significant performance enhancement in photoconductive terahertz optoelectronics by incorporating plasmonic contact electrodes", Nature commun. **4**, 1622 (2013).

137. A. D. Boardman, *Electromagnetic surface modes* (Wiley, 1982).

138. S. A. Maier, *Plasmonics: Fundamentals and applications* (Springer, 2007).

139. A. K. Azad, Y. Zhao, W. Zhang, and M. He,"Effect of dielectric properties of metals on terahertz transmission in subwavelength hole arrays", Opt. Lett. **31**, 2637 (2006).

140. A. K. Azad, and W. Zhang,"Resonant terahertz transmission in subwavelength metallic hole arrays of sub-skin-depth thickness", Opt. Lett. **30**, 2945 (2005).

141. X. Chen, H. R. Park, N. C. Lindquist, J. Shaver, M. Pelton, and S. H. Oh,"Squeezing millimeter waves through a single, nanometer-wide, centimeter-long slit", Sci. Rep. **4**, 6722 (2014).

142. Y. Zhao, and D. R. Grischkowsky,"2-d terahertz metallic photonic crystals in parallel-plate waveguides", IEEE Trans. Microwave Theory Tech. **55**, 656-663 (2007).

143. T. Matsui, A. Agrawal, A. Nahata, and Z. V. Vardeny,"Transmission resonances through aperiodic arrays of subwavelength apertures", Nature **446**, 517-521 (2007).

144. J. Han, X. Lu, and W. Zhang,"Terahertz transmission in subwavelength holes of asymmetric metal-dielectric interfaces: The effect of a dielectric layer", J. Appl. Phys. **103**, 033108 (2008).

145. V. V. Preobrazhenskii, M. A. Putyato, O. P. Pchelyakov, and B. R. Semyagin,"Experimental determination of the incorporation factor of as4 during molecular beam epitaxy of gaas", J. Cryst. Growth **201-202**, 170-173 (1999).

146. W. Braun, *Applied rheed: Reflection high energy electron diffraction during crystal growth* (springer, 1999).

147. V. P. LaBella, M. R. Krause, Z. Ding, and P. M. Thibado,"Arsenic-rich gaas(0 0 1) surface structure", Surf. Sci. Rep. **60**, 1-53 (2005).

148. P. Rodgers,"Nanopatterning: What diffraction limit?", Nat. Nanotechnol. (2009).

149. F. Lukeš,"Oxidation of si and gaas in air at room temperature", Surf Sci. **30**, 91-100 (1972).

150. A. R. Clawson,"Guide to references on iii–v semiconductor chemical etching", Materials Science and Engineering: R: Reports **31**, 1-438 (2001).

151. K. S. S. Harsha, *Principles of vapor deposition of thin films* (Elsevier, 2006).

152. S. Iida, and K. Ito,"Selective etching of gallium arsenide crystals in H 2 SO 4 - H 2 O 2 - H 2 O system", J. Electrochem. Soc. **118**, 768 (1971).

153. N. Vieweg, F. Rettich, A. Deninger, H. Roehle, R. Dietz, T. Göbel, and M. Schell,"Terahertz-time domain spectrometer with 90 db peak dynamic range", J Infrared Millim. Terahertz Waves **35**, 823-832 (2014).

154. Y. Kane,"Numerical solution of initial boundary value problems involving maxwell's equations in isotropic media", IEEE Trans. Antennas Propag. **14**, 302-307 (1966).

155. E. Palik, *Handbook of optical constants of solids* (elsevier, 1997).

156. P. B. Johnson, and R. W. Christy,"Optical constants of the noble metals", Phys. Rev. B **6**, 4370-4379 (1972).

157. N. Khiabani, Y. Huang, L. E. Garcia-Munoz, Y.-C. Shen, and A. Rivera-Lavado,"A novel sub-thz photomixer with nano-trapezoidal electrodes", IEEE Trans. THz Sci. Technol. **4**, 501-508 (2014).

158. R. O. Carlson, G. A. Slack, and S. J. Silverman,"Thermal conductivity of gaas and gaas1−xpx laser semiconductors", J. Appl. Phys. **36**, 505 (1965).

159. S. S. Gevorgian, T. Martinsson, P. L. J. Linner, and E. L. Kollberg,"Cad models for multilayered substrate interdigital capacitors", IEEE Trans. Microwave Theory Tech. **44**, 896-904 (1996).

160. B. V. Zeghbroeck, *Principles of semiconductor devices* (University of Colorado Online Textbook, 2011).

161. J.-M. Rämer, F. Ospald, G. von Freymann, and R. Beigang,"Generation and detection of terahertz radiation up to 4.5 thz by low-temperature grown gaas photoconductive antennas excited at 1560 nm", Appl. Phys. Lett. **103**, 021119 (2013).

162. A. Jooshesh, V. Bahrami-Yekta, J. Zhang, T. Tiedje, T. E. Darcie, and R. Gordon,"Plasmon-enhanced below bandgap photoconductive terahertz generation and detection", Nano Lett. **15**, 8306-8310 (2015).

Appendix A: Nanoplasmonics enhanced terahertz sources

(2014, Optics Express)

Reprinted with permission

The manuscript was written by Afshin Jooshesh and Prof. Reuven Gordon. Sample fabrication was done by Afshin Jooshesh, Vahid Bahrami Yekta and Mostafa Masnadi. THz emission and detection results were measured by Levi Smith and Afshin Jooshesh. The project was founded and supported by Prof. T. Darcie and Prof. R. Gordon.

Nanoplasmonics enhanced terahertz sources

Afshin Jooshesh[1], Levi Smith[1], Mostafa Masnadi-Shirazi[2], Vahid Bahrami-Yekta[1], Thomas Tiedje[1], Thomas E. Darcie[1] and Reuven Gordon[1,*]

[1]*Department of Electrical and Computer Engineering, University of Victoria, 3800 Finnerty Road, Victoria, British Colombia V8P 5C2, Canada*

[2]*Department of Electrical and Computer Engineering, University of British Columbia, 2329 West Mall, Vancouver, British Colombia V6T 1Z4, Canada*

**rgordon@uvic.ca*

Abstract: Arrayed hexagonal metal nanostructures are used to maximize the local current density while effectively removing heat at the nanoscale, thereby allowing for increased emission from photoconductive terahertz (THz) sources. The THz emission field amplitude was increased by 60% above that of a commercial THz photoconductive antenna, even though the hexagonal nanostructured device has 75% of the bias voltage. The arrayed hexagonal outperforms our previously investigated strip array nanoplasmonic structure by providing stronger localization of the current density near the metal surface with an operating bandwidth of 2.6 THz. This approach is promising to achieve efficient THz sources.

OCIS codes: (250.5403) Plasmonics, (160.5140) Photoconductive materials, (040.2235) Far infrared or terahertz.

References and links

1. P. U. Jepsen, R. H. Jacobsen, and S. R. Keiding, "Generation and detection of terahertz pulses from biased semiconductor antennas," J. Opt. Soc. Am. B **13**(11), 2424-2436 (1996).
2. D. Auston, K. Cheung, J. Valdmanis, and D. Kleinman, "Cherenkov Radiation from Femtosecond Optical Pulses in Electro-Optic Media," Phys. Rev. Lett. **53**(16), 1555-1558 (1984).
3. B. B. Hu, and M. C. Nuss, "Imaging with terahertz waves," Opt. Lett. **20**(16), 1716-1718 (1995).
4. C. Jansen, S. Wietzke, O. Peters, M. Scheller, N. Vieweg, M. Salhi, N. Krumbholz, C. Jordens, T. Hochrein, and M. Koch, "Terahertz imaging: applications and perspectives," Appl. Opt. **49**(19), E48-57 (2010).
5. P. U. Jepsen, D. G. Cooke, and M. Koch, "Terahertz spectroscopy and imaging - Modern techniques and applications," Laser Photonics Rev. **5**(1), 124-166 (2011).
6. Kasalynas, R. Venckevicius, and G. Valusis, "Continuous Wave Spectroscopic Terahertz Imaging With InGaAs Bow-Tie Diodes at Room Temperature," IEEE Sensors J. **13**(1), 50-54 (2013).
7. K. Kawase, Y. Ogawa, Y. Watanabe, and H. Inoue, "Non-destructive terahertz imaging of illicit drugs using spectral fingerprints," Opt. Express **11**(20), 2549-2554 (2003).
8. D. M. Mittleman, M. Gupta, R. Neelamani, R. G. Baraniuk, J. V. Rudd, and M. Koch, "Recent advances in terahertz imaging," Appl. Phys. B **68**(6), 1085-1094 (1999).
9. K. Serita, S. Mizuno, H. Murakami, I. Kawayama, Y. Takahashi, M. Yoshimura, Y. Mori, J. Darmo, and M. Tonouchi, "Scanning laser terahertz near-field imaging system," Opt. Express **20**(12), 12959-12965 (2012).

10. Y. C. Shen, T. Lo, P. F. Taday, B. E. Cole, W. R. Tribe, and M. C. Kemp, "Detection and identification of explosives using terahertz pulsed spectroscopic imaging," Appl. Phys. Lett. **86**(24), 241116 (2005).
11. C. Yu, S. Fan, Y. Sun, and E. Pickwell-Macpherson, "The potential of terahertz imaging for cancer diagnosis: A review of investigations to date," Quant. Imaging Med. Surg. **2**(1), 33-45 (2012).
12. S. L. Dexheimer, *Terahertz Spectroscopy: Principles and Applications* (CRC, 2008).
13. R. Faulks, S. Rihani, H. E. Beere, M. J. Evans, D. A. Ritchie, and M. Pepper, "Pulsed terahertz time domain spectroscopy of vertically structured photoconductive antennas," Appl. Phys. Lett. **96**(8), 081106 (2010).
14. B. M. Fischer, M. Walther, and P. U. Jepsen, "Far-infrared vibrational modes of DNA components studied by terahertz time-domain spectroscopy," Phys. Med. Biol. **47**(21), 3807-3814 (2002).
15. S. Yu, B. J. Drouin, and J. C. Pearson, "Terahertz Spectroscopy of the Bending Vibrations of Acetylene12c2h2," Astrophys. J. **705**(1), 786-790 (2009).
16. M. Walther, D. Cooke, C. Sherstan, M. Hajar, M. Freeman, and F. Hegmann, "Terahertz conductivity of thin gold films at the metal-insulator percolation transition," Phys. Rev. B **76**(12), 125408 (2007).
17. B. Heshmat, M. Masnadi-Shirazi, R. B. Lewis, J. Zhang, T. Tiedje, R. Gordon, and T. E. Darcie, "Enhanced Terahertz Bandwidth and Power from GaAsBi-based Sources," Adv. Opt. Mater. **1**(10), 714-719 (2013).
18. B. Heshmat, H. Pahlevaninezhad, Y. Pang, M. Masnadi-Shirazi, R. Burton Lewis, T. Tiedje, R. Gordon, and T. E. Darcie, "Nanoplasmonic terahertz photoconductive switch on GaAs," Nano Lett. **12**(12), 6255-6259 (2012).
19. S. G. Park, K. H. Jin, M. Yi, J. C. Ye, J. Ahn, and K. H. Jeong, "Enhancement of terahertz pulse emission by optical nanoantenna," ACS Nano **6**(3), 2026-2031 (2012).
20. D. M. Mittleman, "Frontiers in terahertz sources and plasmonics," Nature Photon. **7**(9), 666-669 (2013).
21. C. W. Berry, M. R. Hashemi, and M. Jarrahi, "Generation of high power pulsed terahertz radiation using a plasmonic photoconductive emitter array with logarithmic spiral antennas," Appl. Phys. Lett. **104**(8), 081122 (2014).
22. S. Jafarlou, M. Neshat, and S. Safavi-Naeini, "A hybrid analysis method for plasmonic enhanced terahertz photomixer sources," Opt. Express **21**(9), 11115-11124 (2013).
23. V. Pačebutas, K. Bertulis, L. Dapkus, G. Aleksejenko, A. Krotkus, K. M. Yu, and W. Walukiewicz, "Characterization of low-temperature molecular-beam-epitaxy grown GaBiAs layers," Semicond. Sci. Technol. **22**(7), 819-823 (2007).
24. V. PacÌŒebutas, K. Bertulis, A. BicÌŒiuÌ„nas, and A. n. Krotkus, "Low-temperature MBE-grown GaBiAs layers for terahertz optoelectronic applications," Phys. Status Solidi (c) **6**(12), 2649-2651 (2009).
25. C. Baker, I. S. Gregory, W. R. Tribe, I. V. Bradley, M. J. Evans, E. H. Linfield, and M. Missous, "Highly resistive annealed low-temperature-grown InGaAs with sub-500 fs carrier lifetimes," Appl. Phys. Lett. **85**(21), 4965 (2004).
26. M. Awad, M. Nagel, H. Kurz, J. Herfort, and K. Ploog, "Characterization of low temperature GaAs antenna array terahertz emitters," Appl. Phys. Lett. **91**(18), 181124 (2007).
27. J. Sigmund, C. Sydlo, H. L. Hartnagel, N. Benker, H. Fuess, F. Rutz, T. Kleine-Ostmann, and M. Koch, "Structure investigation of low-temperature-grown GaAsSb, a material for photoconductive terahertz antennas," Appl. Phys. Lett. **87**(25), 252103 (2005).
28. Kostakis, D. Saeedkia, and M. Missous, "Terahertz Generation and Detection Using Low Temperature Grown InGaAs-InAlAs Photoconductive Antennas at 1.55," IEEE Trans. THz Sci. Technol. **2**(6), 617-622 (2012).

29. M. Mittendorff, M. Xu, R. J. Dietz, H. Kunzel, B. Sartorius, H. Schneider, M. Helm, and S. Winnerl, "Large area photoconductive terahertz emitter for 1.55 mum excitation based on an InGaAs heterostructure," Nanotechnology **24**(21), 214007 (2013).
30. K. Moon, D. W. Park, I. M. Lee, N. Kim, H. Ko, S. P. Han, D. Lee, J. W. Park, S. K. Noh, and K. H. Park, "Low-temperature-grown InGaAs terahertz photomixer embedded in InP thermal spreading layer regrown by metalorganic chemical vapor deposition," Opt. Lett. **38**(24), 5466-5469 (2013).
31. S. Rihani, R. Faulks, H. E. Beere, I. Farrer, M. Evans, D. A. Ritchie, and M. Pepper, "Enhanced terahertz emission from a multilayered low temperature grown GaAs structure," Appl. Phys. Lett. **96**(9), 091101 (2010).
32. M. Tani, S. Matsuura, K. Sakai, and S.-i. Nakashima, "Emission characteristics of photoconductive antennas based on low-temperature-grown GaAs and semi-insulating GaAs," Appl. Opt. **36**(30), 7853-7859 (1997).
33. Y. Lee, *Principles of Terahertz Science and Technology* (Springer, 2009).
34. S. Preu, G. H. Döhler, S. Malzer, L. J. Wang, and A. C. Gossard, "Tunable, continuous-wave Terahertz photomixer sources and applications," J. Appl. Phys. **109**(6), 061301 (2011).
35. J. Y. Suen, W. Li, Z. D. Taylor, and E. R. Brown, "Characterization and modeling of a terahertz photoconductive switch," Appl. Phys. Lett. **96**(14), 141103 (2010).
36. L. Tian, and W. Shi, "Analysis of operation mechanism of semi-insulating GaAs photoconductive semiconductor switches," J. Appl. Phys. **103**(12), 124512 (2008).
37. P. N. Melentiev, A. E. Afanasiev, A. A. Kuzin, A. S. Baturin, and V. I. Balykin, "Giant optical nonlinearity of a single plasmonic nanostructure," Opt. Express **21**(12), 13896-13905 (2013).
38. K. Wang, E. Schonbrun, P. Steinvurzel, and K. B. Crozier, "Trapping and rotating nanoparticles using a plasmonic nano-tweezer with an integrated heat sink," Nat. Commun. **2**, 469 (2011).
39. H. Aouani, J. Wenger, D. Gerard, H. Rigneault, E. Devaux, T. W. Ebbesen, F. Mahdavi, T. Xu, and S. Blair, "Crucial role of the adhesion layer on the plasmonic fluorescence enhancement," ACS Nano **3**(7), 2043-2048 (2009).
40. M. van Exter, and D. R. Grischkowsky, "Characterization of an optoelectronic terahertz beam system," IEEE Trans. Microwave Theory Tech. **38**(11), 1684-1691 (1990).
41. E. Castro-Camus, J. Lloyd-Hughes, and M. Johnston, "Three-dimensional carrier-dynamics simulation of terahertz emission from photoconductive switches," Phys. Rev. B **71**(19), 195301 (2005).
42. K. Sala, G. Kenney-Wallace, and G. Hall, "CW autocorrelation measurements of picosecond laser pulses," IEEE J. Quantum Electron. **16**(9), 990-996 (1980).
43. C. W. Berry, M. R. Hashemi, S. Preu, H. Lu, A. C. Gossard, and M. Jarrahi, "High power terahertz generation using 1550 nm plasmonic photomixers," Appl. Phys. Lett. **105**(1), 011121 (2014).

1. Introduction

A photoconductive antenna (PCA) can produce terahertz (THz) bandwidth pulses by the generation of photocarriers in the antenna gap using a femtosecond laser [1, 2]. Such THz waves (0.3~10 THz) have applications in security, imaging [3-11], near-field scanning microscopy and spectroscopy [12-16]. Today, PCAs are commercially available as THz sources, with compact size, low cost, and room temperature operation.

Previously, nanoplasmonic structures have been investigated to enhance the performance of THz detectors [17-19]. The main advantage of the nanoplasmonic structure for detection is to create a fast sweep out time, and thereby allow for the usage of a low-cost high-mobility long

carrier lifetime substrate like semi-insulating GaAs [18, 20-22], as opposed to other less common substrates with short carrier lifetimes (such as low-temperature GaAs or GaBiAs) [23-31]. For pulsed THz sources, however, the carrier lifetime is not a limiting factor [32], yet nanoplasmonic structures can still provide an advantage, as we will investigate in this work.

To understand the advantage of nanoplasmonic structures for THz sources, we consider that the radiated THz field amplitude is proportional to the photocurrent density $E_{THz} \propto \partial J(t)/\partial t$ with $J(t)=n(t)q\mu E(t)$, where $n(t)$ is photocarrier density as a function of time, q is the electron charge, μ is mobility, and $E(t)$ is the bias field [33]. It is desirable to maximize J to maximize the THz generated; however, the bias field and charge density are limited by material breakdown, charge screening and thermal damage [1, 34-36]. Among these, the most significant factor is thermal damage. Many researchers in the nanoplasmonics community have realized the ability of metal nanostructures to effectively remove heat in high-field applications such as nonlinear optics [37] and optical tweezers [38]. Here we demonstrate that both the bias field and the carrier density can be increased in a nanoplasmonic structure by effectively removing heat generated near the metal nanostructures. Therefore, the main role of the nanostructured metal is to localize the current density near the metal, where the heat generated can be efficiently removed.

2. Fabrication

Figure 1 shows the nanoplasmonic structures investigated in this work. We used a 500 µm SI-GaAs (100) wafer with 10 MΩ·cm resistivity and electron mobility of ~5500 cm^2/V.s. Closed-gap dipole antennas were patterned using contact UV-photolithography on cleaved substrates. The samples were then placed in an e-beam evaporator to deposit 100 nm gold with a 5 nm titanium (Ti) adhesion layer. We used Ti instead of Cr to increase the electric field of the surface plasmons of the gold and semiconductor interface [39]. Finally, plasmonic structures were milled through the gold using a focused ion beam Hitachi FB-2100 at 11.6 pA current and 40 kV bias. Two 100 nm hexagonal array plasmonic samples, one 100 nm gap strip array plasmonic structure and a 5 µm gap dipole were fabricated for the experiment. The periodicity p and the apex angle θ of the hexagonal structure were optimized using FDTD to increase the field intensity in the substrate (see supporting A).

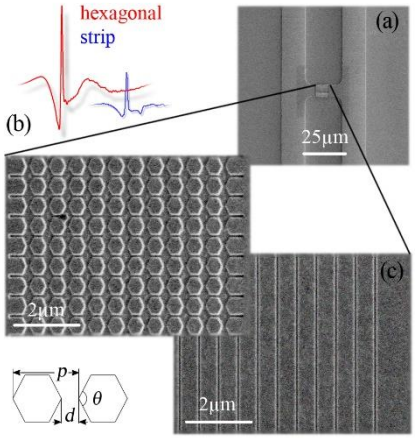

Fig. 1. a) Scanning electron microscope image of the 20 µm dipole on SI-GaAs substrate. b) The active area of the hexagonal plasmonic array. c) The active area of the strip plasmonic array. The diagram shows apex angle θ, gap size d and periodicity p.

3. Results and discussion

Figure 2 a) shows the PCA testing setup. Samples were mounted on printed board circuit (PCB) and positioned against a high resistivity float zone silicon aspheric focusing lens with focal length of 53 mm. The femtosecond-laser is a 785 nm mode-locked fiber laser, which generates 100 fs optical pulses with a 68.9 MHz repetition rate. The delay line was used to sample a 100 ps time window of the THz pulse. In this setup, transmitters were biased with a chopped voltage and received an average 10 mW of optical power. A commercial BATOP (PCA-40-05-10-800-a) photoconductive antenna was placed as a receiver during the measurements at the distance of 10.6 mm from the transmitter with an average 13 mW of optical power. A lock-in amplifier (Stanford SR830) was used to measure the current at the receiver, which is proportional to the THz field. The time domain response and power spectra are shown in Figure 2 b) and c). Clearly, the 100 nm hexagonal array has the highest intensity and bandwidth.

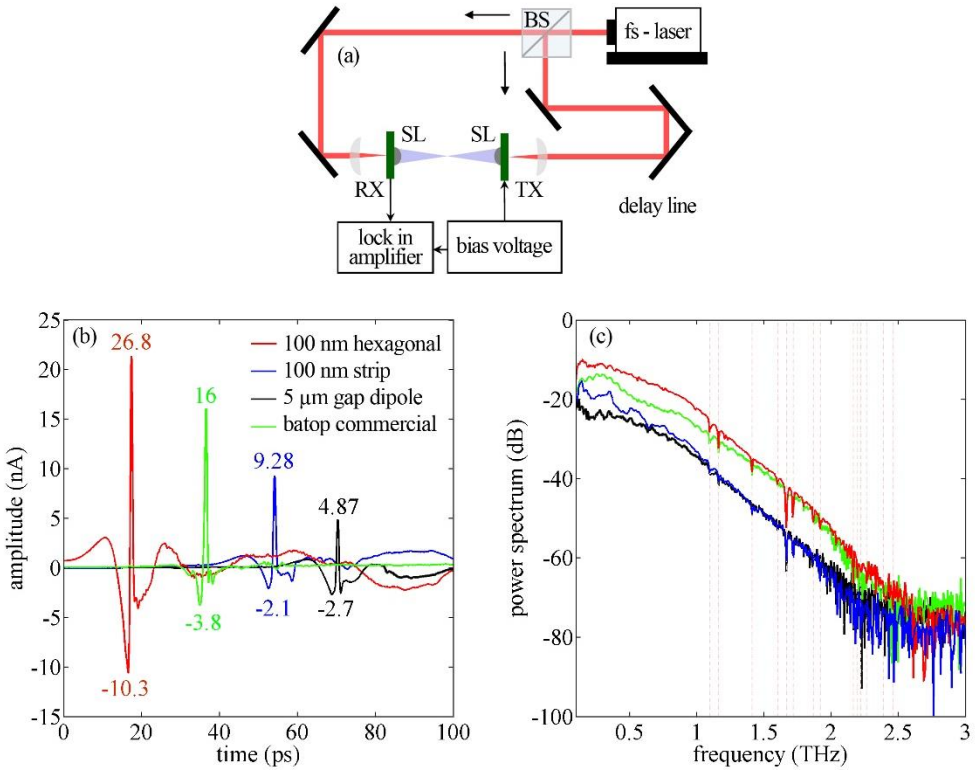

Fig. 2. a) Pulsed mode terahertz setup. BS is a Beam splitter, SL is silicon lens, TX is the transmitter PCA and RX is the commercial PCA receiver. b) and c) are received time and frequency domain signals. Red line is the response of the hexagonal array device resulting in 32 nA peak-to-peak current amplitude, blue line is the strip array device with 11.38 nA peak-to-peak current, green line is the Batop commercial device as a transmitter with 19.8 nA peak-to-peak current and black line is the received THz signal of a 5 µm gap dipole with 7.57 nA peak-to-peak current. Dashed lines in c) are HITRAN water absorption lines.

The higher intensity in Figure 2 b) is directly proportional to the photocurrent. The maximum photocurrent is limited by the bias that can be achieved prior to thermally induced breakdown. To determine the bias, we measured the IV characteristics under illumination, as shown in Figure 3. Using the results from Figure 3, the bias was set to 20% of the on-set of breakdown, to be

consistent with the operating characteristics of the commercial sample. Even though the voltage is higher for the 5 micron gap structure, the local bias field is higher in the nanoplasmonic structures, due to the smaller gaps. Also, the hexagonal array structure has apexes that further act to confine the bias field, and thereby increase the local current density. We note that there is an offset in the I-V characteristic due to photocurrent which is not present under dark conditions (see supporting B).

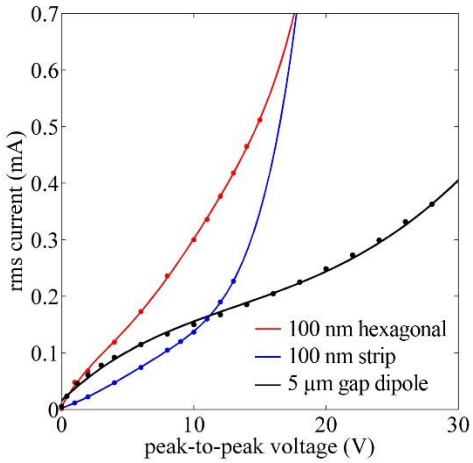

Fig. 3. Electrical characteristics of our semi-insulating GaAs based samples under laser illumination.

Figure 4 a) shows the THz power as a function of femtosecond laser average power, which generates the photocarriers. Comparing the hexagonal and strip array, we see that the initial slope in the THz power generated is higher for the hexagonal array structure, even for the same bias voltage of 10 V used here. This is due to a combination of the higher local bias field and the localization of the photocarriers near the apexes. Of course, screening plays a bigger role in the hexagonal array structure due to the larger photocarrier density, which can be seen from the saturation in the enhancement factor when normalizing to the 5 micron gap, as shown in Figure 4 b).

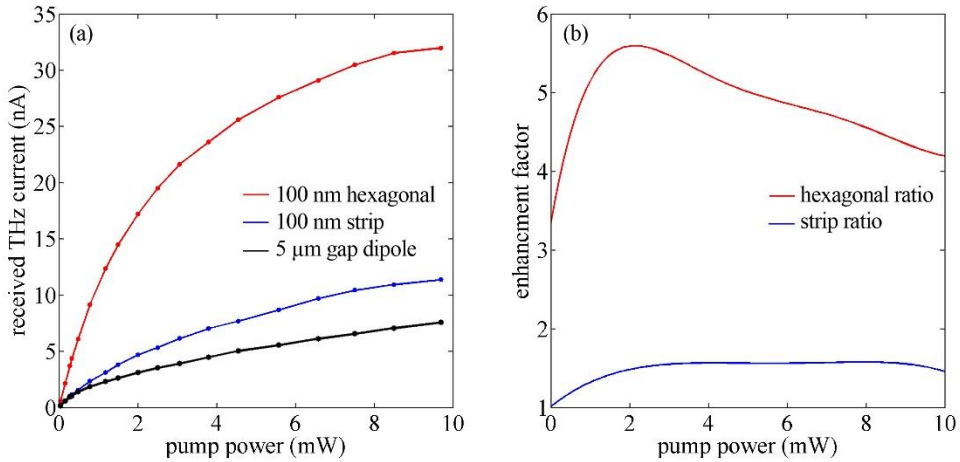

Fig. 4. a) Peak THz received current of the samples as the function of the pump power. b) Enhancement ratio with respect to 5 µm gap dipole (Iplasmonic/I5 µm gap).

As mentioned previously, the improvements to performance are related to the increased photocurrent that can be achieved, due to increased local bias field and photocarriers generated. Gold has a thermal conductivity (3.14W/cm·K) that is 6 times that of GaAs (0.55 W/cm·K). The current density is localized underneath the gold edges for the nanoplasmonic structures, so this benefits efficient heat removal. We use numerical simulation to quantify local current density in the various structures investigated and relate this to the experimental observations. In Table 1, we consider the photocurrent enhancement by integrating the bias field times the laser power in the GaAs (which is proportional to the photocarriers generated) as determined by finite-difference time-domain simulations (see Appendix C for details): $\eta=\int E.Pdv$. We see that the hexagonal array nanoplasmonic structure has the highest enhancement. If we multiply these by the experimentally used voltage, we see reasonable quantitative agreement with our experimentally measured peak THz field, to within a constant scaling factor ($C=0.93$) dependent on the experimental setup. We have neglected screening in this analysis, which has a bigger influence on the hexagonal structures, as described above. This can explain the lower measured current for the hexagonal structure as compared with the numerical prediction.

Table 1. Theoretical and measured emission amplitudes of plasmonic photoconductive antennas.

gap structure	η	bias (V)	$I_{THz}=\eta\times C\times V$ (a.u.)	measured I_{THz} (nA)
hexagonal	4.26	10	39.6	32
strip	1.13	10	10.51	11.38
5 μm gap	0.29	20	5.39	7.57

The bandwidth obtained is comparable for all devices and similar to past works [26, 40, 41]. We have used a short dipole to give a more uniform emission pattern than our past work [18]. We estimate the RC time constant of around 0.5 fs (see supporting D for details), and this is not a limiting factor in the bandwidth. In theory, a 100 fs Gaussian pulse corresponds to 4.4 THz bandwidth [42] and lower bandwidth in practical measurements may be the result of kinetic inductance; however, further investigation of this effect is required.

4. Conclusion

In conclusion, we have demonstrated that nanoplasmonic structures can be used to improve the performance of THz photoconductive sources. Nanoscale localization of the bias field and carrier density close to the metal surface allows for rapid removal of heat, which typically limits PCA power output. In the future, we hope to expand these thermal-management strategies to improve the performance of CW photomixers, where there have already been pioneering works using nanoplasmonics, but not focusing on the thermal management aspects [43].

Supporting A: Optimization of hexagonal array nanoplasmonic structure with finite-difference time-domain simulations

We used the particle swarm optimization method implemented in Lumerical FDTD with the goal of maximizing the transmission into the substrate. Johnson & Christy permittivity values were used for gold. Since the saturation velocity of electrons in GaAs is 1.2×10^7cm/s, a 100 nm gap is considered to allow electrons to reach the electrodes in

sub-picosecond time. Therefore, with a fixed 100 nm gap size, we varied the 2-dimensional periodicity of the gold from 400 nm to 800 nm and the apex angle θ between 90˚ and 180˚. We found that periodicity of 587 nm with θ=127˚ results in maximum transmission into the substrate with a source at 785 nm wavelength.

Figure 5 a) shows 2D optical power density profile of a single hexagonal cell with 100 nm gap size excited at 785 nm. A cross section view of the hexagonal plasmonic cells in Figure 5 b) shows a higher power density profile beneath the hexagon apexes, as compared with a strip array plasmonic structure shown in Figure 5 c). Therefore, we expect to generate a greater number of carriers close to the apexes of the hexagonal array nanostructures.

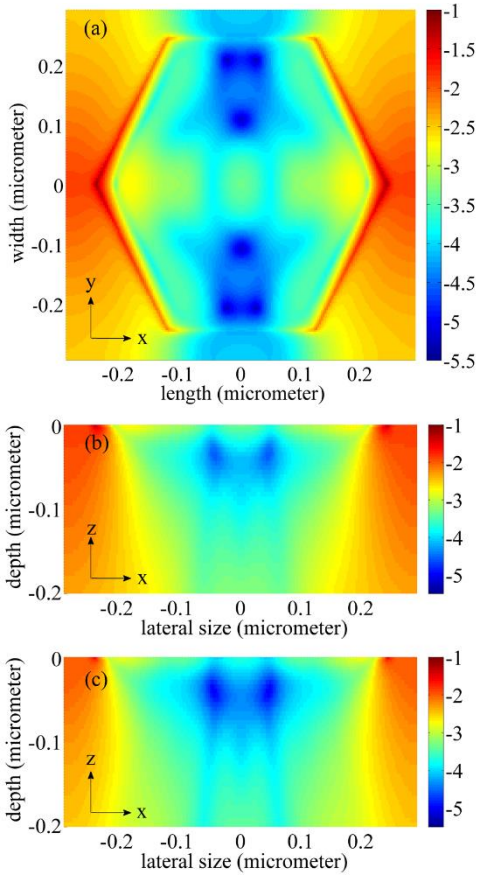

Fig. 5. FDTD simulation results for log10(|P|) at 785 nm and in an arbitrary scale. a) 2D surface power density profile of a single cell period from top, b) cross section view of a single hexagonal cell with 100 nm gap distance, c) cross section view of a 100 nm strip plasmonic structure.

Supporting B: Electrical characteristics of the in-house fabricated samples

Figure 6 shows the dark (without illumination) current-voltage characteristic of the photoconductive switches.

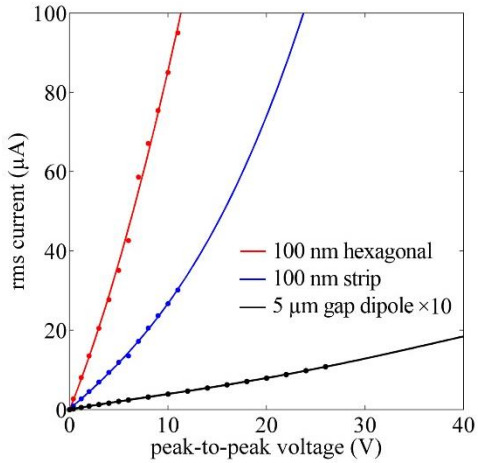

Fig. 6. Electrical characteristics of photoconductive switches at dark condition

Supporting C: Photocurrent enhancement

A key factor in determining the radiation efficiency of the photoconductive emitters is the photocurrent that is generated during the absorption of the pump. As explained in the manuscript, the hexagon structure confines both electric bias field and laser power into the area between apexes. Because the number of photo-generated carriers is proportional to the power inside the gap we can rewrite the current density as $J \propto P.E$ where P and E are the power at 785 nm and the bias electric field distribution profiles inside the gap. We used a plain wave source in FDTD at 0.5 THz (a nominal low frequency value) to determine the quasi-static electric field profile in a 3-dimentional unit cell (587 nm × 587 nm × 400 nm depth) of the plasmonic structures. Then, we normalized the electric field to the voltage drop over each cell of the array according to experimental conditions. Similarly the power profile of a 3-dimentional unit cell was obtained by FDTD simulations using a source at 785 nm. The product of P and E provides the current density distribution at each point. After integrating the P.E over YZ plane slices, the current profile can be plotted over the X axis as can be seen in Figure 7. Finally, the photocurrent enhancement $\eta = \int E.P dv$ obtained by integrating over the gap area along the X axes.

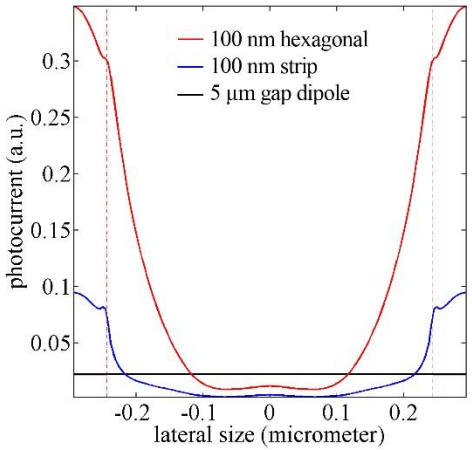

Fig. 7. FDTD simulation results for the photocurrent (P.E) over a unit cell of the plasmonic structures inside the SI-GaAs substrate. Red line is the photocurrent of the hexagonal structure. Blue line is the photocurrent of the strip structure and black is the photocurrent of the GaAs without plasmonic structures on the surface.

Supporting D: Capacitive time constant of the structure

We found a resistivity of 0.5 Ω for the hexagonal array plasmonic structure, 1.2 Ω for the strip array plasmonic structure and 27 Ω for the 5 µm gap photoconductive antenna, using their current-voltage characteristics. Electrostatic simulations in COMSOL Multiphysics suggest a capacitance between 1 fF to 1.5 fF for the plasmonic and 5 µm gap dipole that gives a resistance-capacitance time constant of around 0.5 fs. Therefore, we believe that the RC-roll off does not limit the bandwidth of the THz pulse.

Appendix B: Plasmon-Enhanced below Bandgap Photoconductive Terahertz Generation and Detection

(2015, Nano-letters)

The manuscript was written by Afshin Jooshesh and Prof. Reuven Gordon. Sample fabrication was done by Afshin Jooshesh and Vahid Bahrami Yekta. THz emission and detection results were measured by Afshin Jooshesh. The project was founded and supported by Prof. T. Darcie, Prof. R. Gordon, and Prof. T. Tiedje.

Plasmon-Enhanced below Bandgap Photoconductive Terahertz Generation and Detection

*Afshin Jooshesh, Vahid Bahrami-Yekta, Jinye Zhang, Thomas Tiedje, Thomas E. Darcie, Reuven Gordon**

Department of Electrical and Computer Engineering, University of Victoria, Victoria, BC, Canada V8P5C2.

KEYWORDS: Nanoplasmonics, terahertz, photoconductive switches, femtosecond physics, mid-gap states.

Abstract: We use plasmon enhancement to achieve terahertz (THz) photoconductive switches that combine the benefits of low-temperature grown GaAs with mature 1.5 micron femtosecond lasers operating below the bandgap. These below bandgap plasmon-enhanced photoconductive receivers and sources significantly outperform commercial devices based on InGaAs, both in terms of bandwidth and power, even though they operate well below saturation. This paves the way for high-performance low-cost portable systems to enable emerging THz applications in spectroscopy, security, medical imaging and communication.

There has been considerable interest in terahertz (THz) systems for applications[1-4] including process control[5], imaging[6-8], security[9], medical[10-14], communications[15, 16], and spectroscopy[17-26]. For these applications, portable and low-cost THz systems have been enabled by 1.5 micron femtosecond fiber laser technologies[27-30]. Yet the small bandgap, low resistivity and slower carrier response of 1.5 micron photoconductive antennas using InGaAs limits the performance in terms of output power and bandwidth[27, 30-35]. In addition, InGaAs photoconductive switches are currently several times more expensive than comparable LT-GaAs devices. Interestingly, it has been recognized that LT-GaAs can be used to absorb 1.5 micron light by means of mid-gap arsenic states[36-38]. However, past photoconductive analysis of such devices showed weak photocurrent – an order of magnitude smaller than would be desired for useful devices[36].

Plasmon enhanced THz devices, using nanostructured metals to enhance light-matter interaction, have recently been investigated for THz technologies[39-51]. These have already allowed improved performance in terms of bandwidth, power and thermal management[52]. Here we show significant benefit of applying plasmon enhancement for the two-stage mid-gap absorption process associated with LT-GaAs with 1.57 micron laser sources, as depicted in Figure 1a. In particular, we demonstrate plasmon enhanced LT-GaAs (PE-LT-GaAs) photoconductive switches with twice the peak-to-peak current and three times the bandwidth of current commercial InGaAs devices. It is important to note that plasmonic arrays do not necessarily improve InGaAs based photoconductive switches because they further decrease resistance of the sample.

Figure 1b shows a scanning electron microscope image of one of the tested photoconductive devices. It consists of 2 microns of LT-GaAs grown on GaAs. The growth temperature is 226 Celsius followed by annealing at 630 Celsius for 1 minute. Photolithography was used to define a THz dipole antenna of 15 microns in width in 150 nm of gold with a 5 nm titanium adhesion layer, deposited by e-beam evaporation. Here we implement a simple slit array plasmonic structure with 100 nm gaps and 490 nm

periodicity. These parameters were chosen using finite-difference time-domain simulations, which will be explained later. 18 periods of the array were chosen to have an approximately square active region for optical excitation (considering the width of the bridge was around 10 microns). The slit array was fabricated with focused ion beam milling, and there was an additional trench milled around the dipole to eliminate short-circuiting. A hydrochloric acid etch was used to remove excess gallium deposited by the ion beam.

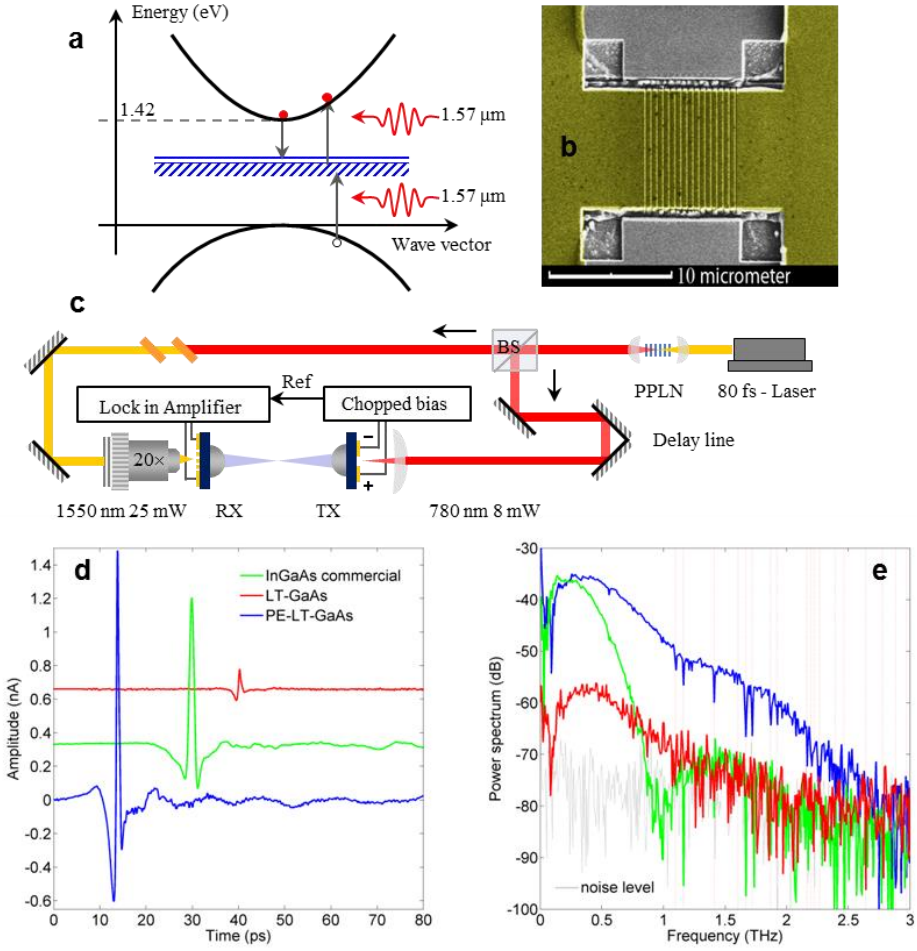

Figure 9. Plasmon enhanced detection characteristics. (a) Schematic of two step 1.57 micron photon absorption process enabled by mid-gap states in arsenic-rich LT-GaAs. (b) Scanning electron microscope image of plasmonic photoconductive switch with 100 nm gaps and 490 nm periodicity. (c) Experimental setup for measuring THz detection using 1570 nm femtosecond laser to excite carriers in photoconductive switches (InGaAs, LT-GaAs, PE-LT-GaAs). THz excitation using commercial LT-GaAs photoconductive switch for all samples. (d) Time domain THz driven current detected at receiver – each curve is offset for clarity. (e) Power spectrum of THz response obtained from results in d.

Figure 1c shows a schematic of the THz detection experiment. For characterization purposes, we relied on second harmonic generation in a periodically poled lithium niobate crystal and a commercial LT-GaAs photoconductive switch for the THz source (BATOP, PCA-40-05-10-800-a). This was done to ensure a high-bandwidth high-power THz source; however, all the receiver devices where pumped only with 1.57 micron 80 fs

light (as ensured by dual long-pass filters – Edmund Optics 950 nm dichroic). The transmitter was biased according to specifications (chopped for lock-in) and the receivers were each directly connected to the lock-in amplifier.

Figure 1d shows the THz driven photocurrent detected at the receiver for three separate devices: commercial InGaAs (BATOP, PCA-40-05-10-1550-a), an LT-GaAs dipole with 5 micron gap, and a PE-LT-GaAs device as shown in the SEM of Figure 1b. The curves are offset for clarity. It is clear from this figure that the PE-LT-GaAs device has a sharper and higher peak response than the commercial device for the same operating conditions. It is interesting to note that our devices do not have any antireflection coatings, which are used in the commercial devices to improve coupling. Figure 1e shows the power spectrum of these photoconductor receivers, showing that the bandwidth is three times larger for the PE-LT-GaAs device as compared to the commercial sample. Of course, the bandwidth may be improved by further averaging to lower the noise floor; therefore the roll-off is also an important characteristic. Here we obtain a roll-off that is typically better than the 20 dB/THz obtained in commercial InGaAs devices (also those provided by other vendors). This shows the benefit of using LT-GaAs in these applications due to its superior material response characteristics. The usual water absorption lines are seen in the power spectrum (denoted with vertical dashed lines in Figure 1e) since the experiment was performed in ambient conditions. We estimate an approximately 0.05 μW of power[53] generated by the PE-LT-GaAs (also see supporting information for the electric field). Table 1 summarizes experimental results for the receiver configuration.

While it is clear that the PE-LT-GaAs device shows improved performance up to 25 mW pump power, it is important to note that this is well below the saturation power for this device. The InGaAs commercial device begins to saturate below 20 mW (i.e., the linear curve rolls off) as shown in Figure 2a. By contrast, the LT-GaAs and PE-LT-GaAs devices do not show saturation up to 25 mW. The superiority of the LT-GaAs material at 1.5 μm is more noticeable at greater pump powers. Therefore, we used maximum capacity of our femtosecond laser to illuminate PE-LT-GaAs and LT-GaAs samples (see Supporting Information for THz time domain results at a same power). We increased the pump power to 200 mW using an external erbium-doped fiber amplifier and still did not see saturation (see Figure 2b); however, this external amplifier degrades the pulse bandwidth and so it was not used in general. Nevertheless, this shows the potential of these devices to operate using commercially available higher power femtosecond 1.5 micron devices. The high power potential of these PE-LT-GaAs devices is enabled by three factors: the lack of direct bandgap absorption, the lower absorption from the gold at 1.5 microns (as compared to 800 nm), and the fast heat dissipation by the adjacent gold material[52]. We also note that there is an initial super-linear dependence ($P^{1.35}$) observed for low powers in the PE-LT-GaAs and LT-GaAs devices This is expected from the two-stage absorption process before the saturation of the mid-gap states[36-38].

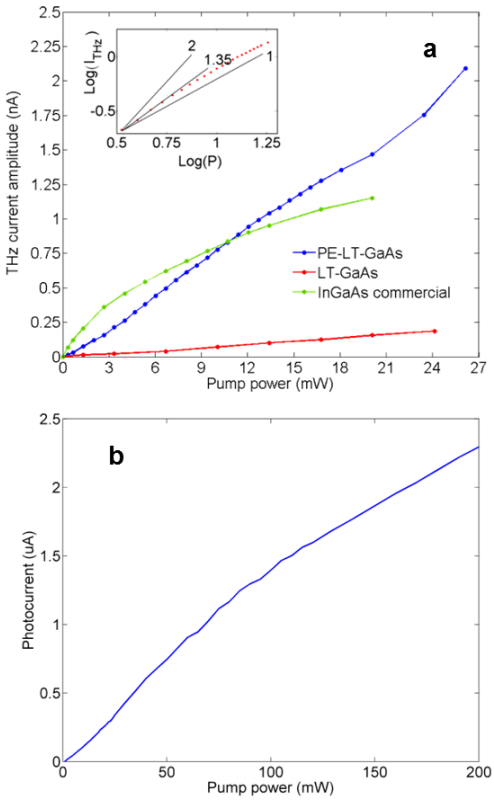

Figure 2. Power dependence of photocurrent. (a) Pump-power dependent peak-to-peak THz signal of three devices tested as a receiver. Inset shows a 1.35 power dependence of LT-GaAs up to the saturation of the mid-gap states, as reported in past works. (b) Photocurrent of a PE-LT-GaAs device under 1.5 micron laser excitation. The device was biased at 1 V DC during the measurement.

Finally, we investigate the performance of these devices as THz sources, as shown schematically in Figure 3a. The LT-GaAs and PE-LT-GaAs samples were biased at 20 V and the InGaAs device was biased at 3V (following the specification sheet). The 20 V bias was selected to be 20% lower than the on-set of breakdown on both in-house fabricated samples, to be consistent with operation specification of the InGaAs commercial sample. The higher bias is allowed in LT-GaAs devices due to the higher resistivity. Overall, similar performance enhancements as for the receiver are seen for the PE-LT-GaAs photoconductive source with respect to the commercial InGaAs device and the LT-GaAs dipole, as shown in Figures 3b and c.

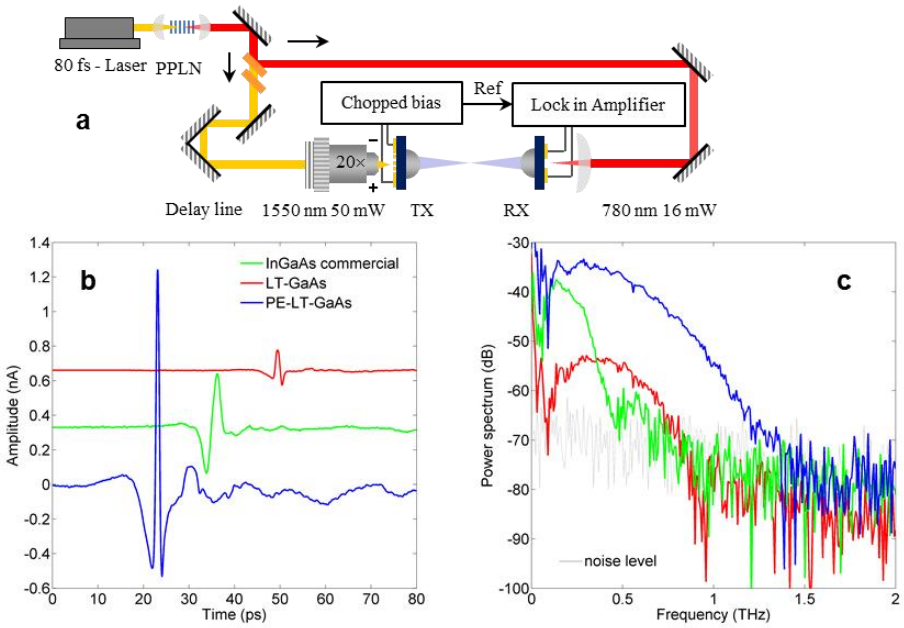

Figure 3. Plasmon enhanced generation characteristics. (a) Experimental setup for measuring THz generation using 1570 nm femtosecond laser to excite carriers in photoconductive switches (InGaAs, LT-GaAs, PE-LT-GaAs). THz detection using commercial LT-GaAs photoconductive switch for all samples. (b) Time domain THz driven current detected at receiver, offset for clarity. (c) Power spectrum of THz response obtained from results in b.

Table 1. Summary of the measurements and comparison with past works.

Sample	THz amplitude	Bandwidth
PE-LT-GaAs	2.10 (nA)	2.43 (THz)
LT-GaAs 5 µm gap	0.187 (nA) 0.08 (nA) - Tani et al.36	1.57 (THz) 3.2 (THz) with 70 fs laser - Ramer et al.38
InGaAs commercial	1.137 (nA) 1.7 (nA) planar system - Roehle et al.54	0.95 (THz) 1.5 (THz) – BATOP GmbH

We performed finite-difference time-domain simulations to design our PE-LT-GaAs structures. With a fixed 100 nm gap width, we swept the period from 100 nm to 1500 nm and the thickness from 100 to 150 nm using Lumerical's FDTD Solutions with the goal of maximizing the transmission into the substrate. Johnson & Christy and Palik permittivity values were used for gold and GaAs, respectively. We found that periodicity of 490 nm results in maximum transmission (40%) into the substrate with a source at 1.57 µm wavelength at the thickness of 150 nm (maximum Ion beam milling fabrication thickness for 100 nm gap size). From these simulations, we found that the maximum local electric field intensity inside the PE-LT-GaAs structure is enhanced by 25 times with respect to the 5 micron gap LT-GaAs dipole. The plasmonic enhancement is shown

in Figure 4. This peak enhancement occurs over a reduced volume where there are plasmonic hot-spots, so the increased PE-LT-GaAs linear absorption from the mid-gap states (once saturation of the mid-gap states is achieved) is less than 25. The enhancement of LT-GaAs mid-gap absorption has the characteristics that make it well-suited for plasmonics: there is a weak optical process that requires high bandwidth response and losses can be tolerated[55].

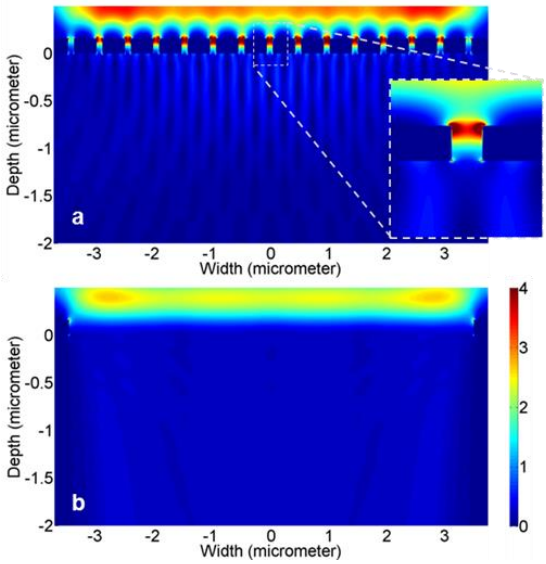

Figure 4. Cross section of plasmonic enhancement showing local intensity increase. (a) PE-LT-GaAs. (b) LT-GaAs.

We performed polarization analysis on the PE-LT-GaAs and LT-GaAs photoconductive switches in receiver mode and found strong polarization dependence (with extinction down to zero) for the plasmon enhanced device, and a weaker polarization dependence for the 5 micron gap device (see Supplementary Information). The strong polarization dependence is expected since the 100 nm slits can transmit only TM polarization. There is weaker polarization dependence from the metal edges of the LT-GaAs device.

In summary, we have demonstrated a plasmon-enhanced LT-GaAs photoconductive antenna as a THz detector and source. This device achieves performance characteristics superior to existing InGaAs-based photoconductive devices as summarized in Table 1. This technology is poised to have a transformative impact on emerging applications for low-cost portable THz systems by leveraging well-established high-power 1.5 micron fiber-laser technologies.

ACKNOWLEDGMENT

The authors acknowledge funding from the NSERC Strategic Project Grants program.

ASSOCIATED CONTENT

Supporting Information

THz generation and detection using LT-GaAs based devises under 1.57 laser excitation

Figure S1 shows THz generation and detection using 1.57 um laser excitation on both LT-GaAs based samples. We used the LT-GaAs commercial sample (BATOP, PCA-40-05-10-800-a) as a transmitter and the PE-LT-GaAs sample as a receiver. First, we aligned the THz path at 780 nm. Then, the periodically poled lithium niobate crystal was entirely removed from the laser path and we realigned optics to illuminate the gap area of both samples. Due to poor performance of the large gap LT-GaAs commercial sample, the signal amplitude is low but it clearly shows operation of LT-GaAs based devices under 1.57 um laser excitation

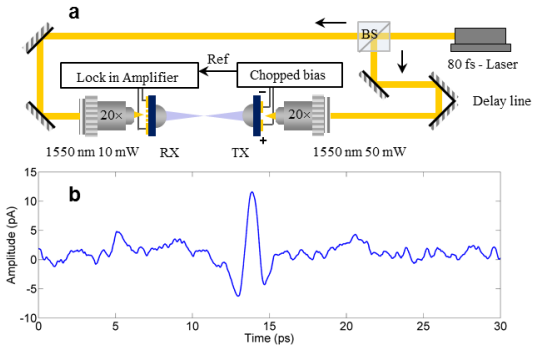

Figure S1. Time domain THz current of both LT-GaAs based source and receiver at 1570 nm. Transmitter is a LT-GaAs commercial sample and detector is the PE-LT-GaAs sample.

THz current detection at a fixed pump power

Figure S2 shows THz current detected by PE-LT-GaA, LT-GaAs and InGaAs commercial samples under 20 mW of laser power. Samples were tested in the THz setup shown in Figure 1c.

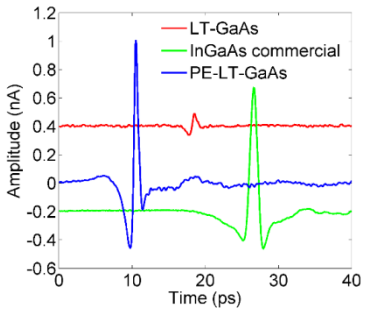

Figure S2. Time domain THz driven current detected with 20 mW of 1.57 um laser power.

Polarization dependence

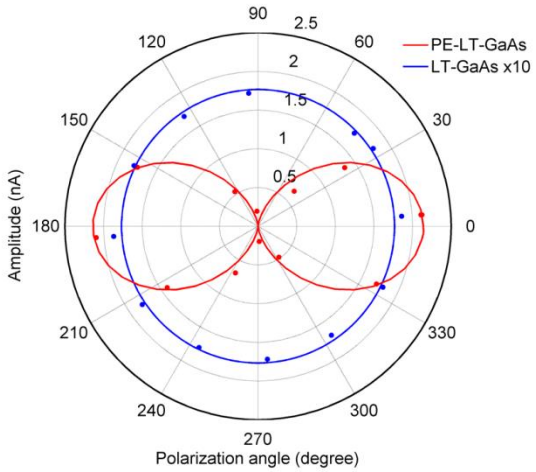

Figure S3. Polarization dependence. The driven THz current detected at the receiver as a function of 1.57 micron laser beam polarization. The measurement was performed using a zero-order 1.5 micron wavelength half wave plate in front of the receiver.

As expected from the FDTD simulations, the PE-LT-GaAs device showed a strong polarization dependence since the slits only transmit TM waves.

Estimation of the electric field

Based on simple electrical considerations of the receiver current and resistance, we estimate a peak THz field of 280 V/m at the receiver generated by the PE-LT-GaAs excited by 1570 nm. This includes a factor of 10 field enhancement estimated for the gap antenna[1]. Assuming 10% power coupling efficiency between the transmitter and receiver, the field at the PE-LT-GaAs source would be ~90 V/m.

REFERENCES

1. Low, T.; Avouris, P. ACS nano 2014, 8, 1086-1101.
2. Preu, S.; Döhler, G. H.; Malzer, S.; Wang, L. J.; Gossard, A. C. J. Appl. Phys. 2011, 109, 061301.
3. Fu, X.; Wu, H.; Xi, X.; Zhou, J. J. Phys. Chem. A 2014, 118, 333-338.
4. Horiuchi, N. Nature Photon. 2010, 4, 140-140.
5. Park, H.-R.; Chen, X.; Nguyen, N.-C.; Peraire, J.; Oh, S.-H. ACS Photonics 2015, 2, 417-424.
6. Jansen, C.; Wietzke, S.; Peters, O.; Scheller, M.; Vieweg, N.; Salhi, M.; Krumbholz, N.; Jordens, C.; Hochrein, T.; Koch, M. Appl. Opt. 2010, 49, E48-57.
7. Serita, K.; Mizuno, S.; Murakami, H.; Kawayama, I.; Takahashi, Y.; Yoshimura, M.; Mori, Y.; Darmo, J.; Tonouchi, M. Opt. Express 2012, 20, 12959-12965.
8. Mittleman, D. M.; Gupta, M.; Neelamani, R.; Baraniuk, R. G.; Rudd, J. V.; Koch, M. Appl. Phys. B 1999, 68, 1085-1094.
9. Shen, Y. C.; Lo, T.; Taday, P. F.; Cole, B. E.; Tribe, W. R.; Kemp, M. C. Appl. Phys. Lett. 2005, 86, 241116.
10. Park, H. R.; Ahn, K. J.; Han, S.; Bahk, Y. M.; Park, N.; Kim, D. S. Nano Lett. 2013, 13, 1782-1786.
11. Fischer, B. M.; Walther, M.; Jepsen, P. U. Phys. Med. Biol. 2002, 47, 3807-3814.

12. Yu, C.; Fan, S.; Sun, Y.; Pickwell-Macpherson, E. Quant. Imaging Med. Surg. 2012, 2, 33-45.
13. Kawase, K.; Ogawa, Y.; Watanabe, Y.; Inoue, H. Opt. Express 2003, 11, 2549-2554.
14. Ma, Y.; Huang, M.; Ryu, S.; Bark, C. W.; Eom, C. B.; Irvin, P.; Levy, J. Nano Lett. 2013, 13, 2884-2888.
15. Zhang, Y.; Qiao, S.; Liang, S.; Wu, Z.; Yang, Z.; Feng, Z.; Sun, H.; Zhou, Y.; Sun, L.; Chen, Z.; Zou, X.; Zhang, B.; Hu, J.; Li, S.; Chen, Q.; Li, L.; Xu, G.; Zhao, Y.; Liu, S. Nano Lett. 2015, 15, 3501-3506.
16. Degl'Innocenti, R.; Jessop, D. S.; Shah, Y. D.; Sibik, J.; Zeitler, J. A.; Kidambi, P. R.; Hofmann, S.; Beere, H. E.; Ritchie, D. A. ACS nano 2014, 8, 2548-2554.
17. Guglietta, G. W.; Diroll, B. T.; Gaulding, E. A.; Fordham, J. L.; Li, S.; Murray, C. B.; Baxter, J. B. ACS nano 2015, 9, 1820-1828.
18. Moon, K.; Park, H.; Kim, J.; Do, Y.; Lee, S.; Lee, G.; Kang, H.; Han, H. Nano Lett. 2015, 15, 549-552.
19. Faulks, R.; Rihani, S.; Beere, H. E.; Evans, M. J.; Ritchie, D. A.; Pepper, M. Appl. Phys. Lett. 2010, 96, 081106.
20. Inagaki, T.; Hartley, I. D.; Tsuchikawa, S.; Reid, M. Holzforschung 2014, 68.
21. Jepsen, P. U.; Cooke, D. G.; Koch, M. Laser Photon. Rev. 2011, 5, 124-166.
22. Loata, G. C.; Thomson, M. D.; Löffler, T.; Roskos, H. G. Appl. Phys. Lett. 2007, 91, 232506.
23. Schall, M.; Helm, H.; Keiding, S. R. Int. J. Infrared Milli. 1999, 20, 595-604.
24. Tomasino, A.; Parisi, A.; Stivala, S.; Livreri, P.; Cino, A. C.; Busacca, A. C.; Peccianti, M.; Morandotti, R. Sci. Rep. 2013, 3, 3116.
25. Tonouchi, M. Nature Photon. 2007, 1, 97-105.
26. Grischkowsky, D.; Keiding, S.; Exter, M. v.; Fattinger, C. J. Opt. Soc. Am. B 1990, 7, 2006.
27. Mittendorff, M.; Xu, M.; Dietz, R. J.; Kunzel, H.; Sartorius, B.; Schneider, H.; Helm, M.; Winnerl, S. Nanotechnology 2013, 24, 214007.
28. Berry, C. W.; Hashemi, M. R.; Preu, S.; Lu, H.; Gossard, A. C.; Jarrahi, M. Appl. Phys. Lett. 2014, 105, 011121.
29. Vieweg, N.; Rettich, F.; Deninger, A.; Roehle, H.; Dietz, R.; Göbel, T.; Schell, M. J. Infrared Millim. Terahertz Waves 2014, 35, 823-832.
30. Kostakis, I.; Saeedkia, D.; Missous, M. IEEE Trans. THz Sci. Technol. 2012, 2, 617-622.
31. Moon, K.; Park, D. W.; Lee, I. M.; Kim, N.; Ko, H.; Han, S. P.; Lee, D.; Park, J. W.; Noh, S. K.; Park, K. H. Opt. Lett. 2013, 38, 5466-5469.
32. Ospald, F.; Maryenko, D.; von Klitzing, K.; Driscoll, D. C.; Hanson, M. P.; Lu, H.; Gossard, A. C.; Smet, J. H. Appl. Phys. Lett. 2008, 92, 131117.
33. Suzuki, M.; Tonouchi, M. Appl. Phys. Lett. 2005, 86, 051104.
34. Takazato, A.; Kamakura, M.; Matsui, T.; Kitagawa, J.; Kadoya, Y. Appl. Phys. Lett. 2007, 90, 101119.
35. Globisch, B.; Dietz, R. J. B.; Stanze, D.; Göbel, T.; Schell, M. Appl. Phys. Lett. 2014, 104, 172103.
36. Tani, M.; Lee, K.-S.; Zhang, X. C. Appl. Phys. Lett. 2000, 77, 1396.
37. Kataoka, T.; Kajikawa, K.; Kitagawa, J.; Kadoya, Y.; Takemura, Y. Appl. Phys. Lett. 2010, 97, 201110.
38. Rämer, J.-M.; Ospald, F.; von Freymann, G.; Beigang, R. Appl. Phys. Lett. 2013, 103, 021119.
39. Seo, M. A.; Park, H. R.; Koo, S. M.; Park, D. J.; Kang, J. H.; Suwal, O. K.; Choi, S. S.; Planken, P. C. M.; Park, G. S.; Park, N. K.; Park, Q. H.; Kim, D. S. Nature Photon. 2009, 3, 152-156.
40. Ramakrishnan, G.; Kumar, N.; Ramanandan, G. K. P.; Adam, A. J. L.; Hendrikx, R. W. A.; Planken, P. C. M. Appl. Phys. Lett. 2014, 104, 071104.

41. Bahk, Y. M.; Kang, B. J.; Kim, Y. S.; Kim, J. Y.; Kim, W. T.; Kim, T. Y.; Kang, T.; Rhie, J.; Han, S.; Park, C. H.; Rotermund, F.; Kim, D. S. Phys. Rev. Lett. 2015, 115, 125501.
42. Chen, X.; Park, H. R.; Pelton, M.; Piao, X.; Lindquist, N. C.; Im, H.; Kim, Y. J.; Ahn, J. S.; Ahn, K. J.; Park, N.; Kim, D. S.; Oh, S. H. Nature commun. 2013, 4, 2361.
43. Polyushkin, D. K.; Hendry, E.; Stone, E. K.; Barnes, W. L. Nano Lett. 2011, 11, 4718-4724.
44. Kabiri, A.; Girgis, E.; Capasso, F. Nano Lett. 2013, 13, 6040-6047.
45. Fehrenbacher, M.; Winnerl, S.; Schneider, H.; Doring, J.; Kehr, S. C.; Eng, L. M.; Huo, Y.; Schmidt, O. G.; Yao, K.; Liu, Y.; Helm, M. Nano Lett. 2015, 15, 1057-1061.
46. Mittleman, D. M. Nature Photon. 2013, 7, 666-669.
47. Berry, C. W.; Wang, N.; Hashemi, M. R.; Unlu, M.; Jarrahi, M. Nature commun. 2013, 4, 1622.
48. Kim, J. Y.; Kang, B. J.; Park, J.; Bahk, Y. M.; Kim, W. T.; Rhie, J.; Jeon, H.; Rotermund, F.; Kim, D. S. Nano Lett. 2015, 15, 6683–6688.
49. Heshmat, B.; Pahlevaninezhad, H.; Pang, Y.; Masnadi-Shirazi, M.; Burton Lewis, R.; Tiedje, T.; Gordon, R.; Darcie, T. E. Nano Lett. 2012, 12, 6255-6259.
50. Park, S. G.; Jin, K. H.; Yi, M.; Ye, J. C.; Ahn, J.; Jeong, K. H. ACS nano 2012, 6, 2026-2031.
51. Cai, X.; Sushkov, A. B.; Jadidi, M. M.; Nyakiti, L. O.; Myers-Ward, R. L.; Gaskill, D. K.; Murphy, T. E.; Fuhrer, M. S.; Drew, H. D. Nano Lett. 2015, 15, 4295-4302.
52. Jooshesh, A.; Smith, L.; Masnadi-Shirazi, M.; Bahrami-Yekta, V.; Tiedje, T.; Darcie, T. E.; Gordon, R. Opt. Express 2014, 22, 27992-28001.
53. MacDonald, K. F.; Sámson, Z. L.; Stockman, M. I.; Zheludev, N. I. Nature Photon. 2008, 3, 55-58.

Appendix C: THz Field Enhancement by Antenna Coupling to a Tapered Thick Slot Waveguide

(2014, IEEE JOURNAL OF LIGHTWAVE TECHNOLOGY)

Reprinted with permission

The manuscript was written by Levi Smith. Sample fabrication was done by Levi Smith and Farid Ahmed. Measurements were done by Levi Smith and Afshin Jooshesh. The project was founded and supported by Prof. T. Darcie. Jinye Zhang provided his knowledge of optics and material, which helped with interpreting the measured data.

THz Field Enhancement by Antenna Coupling to a Tapered Thick Slot Waveguide

Levi Smith, Farid Ahmed, Afshin Jooshesh, Jinye Zhang, Member, IEEE, Martin Jun, and Thomas Darcie, Fellow, IEEE

Abstract—We demonstrate experimentally the coupling of a THz beam into a laser-machined double-tapered thick slot waveguide operating between 0.3 and 2 THz. Simulation reveals that the THz field generated by a standard photoconductive antenna coupled to an undoped aspheric HRFZ-silicon focusing lens can be enhanced by 30 dB in the 40 μm taper waist, relative to a traditional Gaussian beam waist (at 1 THz). Analysis of the 8 dB insertion loss reveals positive implications for coupling between THz transceivers and in-plane-emitting antennas or low-loss THz waveguides.

Index Terms—Parallel plate waveguide, tapered waveguide, terahertz, terahertz field enhancement.

Optical guiding and focusing mechanisms are commonly used in the terahertz (THz) frequency domain. Reflective (metallic) or transmissive (typically silicon or Teflon) lenses are generally used in commonplace THz time-domain spectrometers to focus the THz beam into a sample region. More recently, it has become desirable to increase THz field intensity beyond that which can be obtained using traditional Gaussian beam optics for sensitive spectroscopy and non-linear THz applications [1]. Previous studies have investigated tapered parallel-plate waveguides where the field confinement geometry is well defined [1]–[3] as a means of achieving sub-wavelength beam dimensions and hence high field intensities. For plate separations of 40 μm, enhancements of approximately 30 dB have
been demonstrated [2].

Parallel-plate waveguides show promising characteristics, but they suffer due to complex construction and implementation. Parallel-plate waveguides are usually implemented by translating one or both waveguide plates using a micrometer stage, a technique that requires significant interaction and could not be simply integrated into a turn-key system. The thick slot wave- guide presented here is capable of attaining similar performance, but with significant ease of construction.

Adiabatic field compression and expansion of parallel-plate waveguides has been demonstrated by others. Zhang and Grischkowsky [4] investigated a double-tapered parallel-plate waveguide which utilizes Si lenses to couple the THz field in and out of the waveguide. While the approach shows good results, it is subject to reflective losses at the lens interfaces and challenging alignment. Shutler and Grischkowsky [5] have developed a double-tapered parallel-plate waveguide without THz lenses utilizing cylinders. In this work we use a thick slot wave- guide rather than a parallel-plate waveguide. Our structures can be manufactured easily with other planar circuit elements (resonators, filters, etc).

The novelty of the work presented in this paper is primarily associated with the simplicity and effectiveness of the tapered thick slot waveguide. Using femtosecond laser micromachining, efficient tapered thick slot waveguides can be accurately constructed and implemented.

In addition to enhancing the strength of the THz field, adiabatic waveguide tapers may provide other useful functions. Typical semiconductor THz sources and receivers have dimensions of typically a few μm. For example, a typical photoconductive antenna (PCA) has a gap width of less than 5 microns [6]. Active circuits operating at THz frequencies [7] use extremely small features sizes such that these oscillators or mixers are much smaller than the wavelengths of the signals to be generated. However, as has been demonstrated through numerous recent studies, low-loss waveguide propagation requires waveguide dimensions more comparable to the wavelength (i.e. 0.3 mm at 1 THz). Two-wire or parallel-plate waveguides of these dimensions are capable of propagation loss at 1 THz of less than

1.87 dB/cm [8], [9], substantially lower than for any wave- guide with dimensions comparable to transceiver dimensions. Waveguide tapers offer an attractive means for coupling into and out of low-loss THz waveguides.

Another application for tapers is antenna coupling. A conventional PCA places the photoconductive gap at the center of a planar dipole or other planar antenna. Resulting radiation is emitted normal to and into the semiconductor surface and collimated or focused typically using a silicon lens at the back of the substrate. An alternative is to define an antenna aperture at the output of a slotline taper and to capture the emission in the plane of the semiconductor. Such in-plane-emitting antennas offer a wealth of design possibilities with potentially significantly reduced beamwidths, as demonstrated in many examples at microwave frequencies [10].

Similar taper structures are required for all three applications discussed above; enhancing field intensity, matching between small sources and larger waveguides, and defining in-plane antennas. Enhancing field intensity requires a two-sided taper to compress and re-expand an incident THz beam. The other two applications require just an expansion taper, which is just one half of the two-sided taper. Ideally, structures would convert be- tween a photoconductive gap of a few microns and an aperture width or waveguide conductor separation of several millimeters. In the previously explored parallel-plate structures, the plate thickness is greater than the plate separation. While performance is potentially good, these structures are rather difficult to manufacture and implement into a system. Our preference is to consider a planar structure fabricated using a standard thin

($\approx 400\mu m$) copper sheet and laser machining to define the thick

slot waveguide taper with high precision.

Section I will describe the individual components associated with developing a practical waveguide. Section II will describe the simulation techniques and results obtained for the wave- guide taper. Section III will describe our experimental procedure and analyze the results. Section IV discusses our results which exhibit good agreement between simulation and experiment. Section V concludes the paper with a brief summary and a forecast of the impact that this waveguide can have on other THz applications.

I. TAPERED THICK SLOT WAVEGUIDE

This section explains the design philosophy behind our tapered thick slot waveguides. After a introduction to slotlines waveguide (Section I-A) and the PCAs used to generate and detect the THz signals in our experiment (Section I-B), the design and fabrication of our waveguide is described.

A. Slotline Waveguide

A slotline waveguide is a printed or etched metalization on a dielectric substrate which is commonly used at microwave frequencies. A slotline is typically used since it only requires a single-sided metalization on a substrate. Alternatives, such as a microstrip waveguides operate on a dielectric with a two-sized metalization. For most THz applications, fabrication, coupling, and loss (conductor and dielectric) limit the usefulness of microstrips. The slotline also has the added benefit that it doesn't require the field to exist in the dielectric because the field can exist in the air between the two metalizations; although, to note, the field fringes into the substrate. Slotlines on dielectric sub- strates are prone to high-frequency dielectric losses which originate from leaky-wave (or shock-wave) radiation; to mitigate the leaky-wave radiation loss, the slotline can be sandwiched between two identical dielectric substrates [9].

B. PCA Basics

PCAs are one of the simplest and cheapest methods to gener- ate broadband THz signals. In essence a PCA is a metalization on a high-mobility photoconductive substratetypically GaAs, LT-GaAs, or InAs. Most commercial THz PCAs are constructed using LT-GaAs where the sub-ps carrier lifetime allows for use as either a transmitting or receiving antenna. The metalization is used to supply charge to the antenna that will be impulsed by a femtosecond laser which in turn emits a broadband THz field. Upon generation of the THz field, most of the radiation is transmitted pseudo-omnidirectionally into the substrate due to comparatively high dielectric constant. At the substrate/air interface at the back of the substrate a THz lens must be used

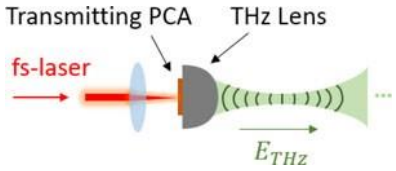

Fig. 1. A THz field is generated by pulsing a biased PCA with a femtosecond laser. The transmitted field profile of the THz beam is dependent on the aspheric focusing Si THz lens.

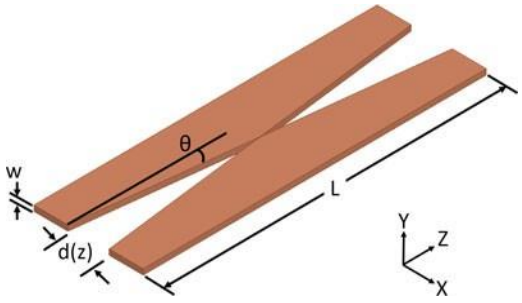

Fig. 2. Overview of the thick slot waveguide structure used in the experi- ments. For our experiments: dma x = 5 mm, dmin = 40 μm, w = 400 μm,
L = 40.4 mm, and θ = 7◦.

to maximize useful power by overcoming the total internal re- flection condition at the interface. The THz lens can either be focusing, collimating, or diverging. Fig. 1 illustrates a typical THz transmitter mounted to a focusing lens.
This work uses commercially available PCAs coupled to an aspheric focusing lens as a source and detector of THz radiation. The source radiation is coupled into and received from the laser- machined tapered thick slot waveguide. Consideration is made, as discussed below, to match the taper aperture to the THz beam profile from the PCA.

C. Thick Slot Waveguide Tapers

Slotline tapers for THz applications have been analyzed in detail [11], but in the absence of strong experimental results publication of these analytical and simulation results is limited [12], [13]. Based on these prior findings, Fig. 2 illustrates the tapered waveguide structure used in the current work. The waveguide consists of a planar input and output taper which are designed to match to the convergence angle of the PCA's Si focusing lens to optimize coupling. The waveguides plate separation, d(z), tapers from 5 mm to 40 μm and then tapers back to 5mm. The waveguide was constructed using a high conductivity copper sheet with a thickness, w, of 0.4 mm. The waveguide tapers were machined using a femtosecond laser as discussed later.
Waveguide dimensions have been selected to provide significant field enhancement and to minimize the frequency dependent conductor loss. Conductor loss has been estimated by Eqn.
(1) [14] and Fig. 3 illustrates the total integrated conductor loss for the entire waveguide. It can be observed that the loss is low and therefore should not pose significant detrimental effects to

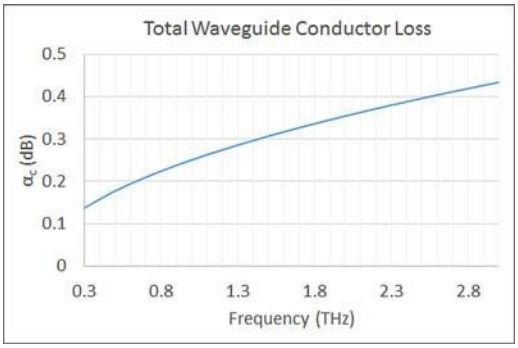

Fig. 3. Worst case integrated conductor loss along the length of the waveguide modeled using the equation for a TEM parallel-plate waveguide.

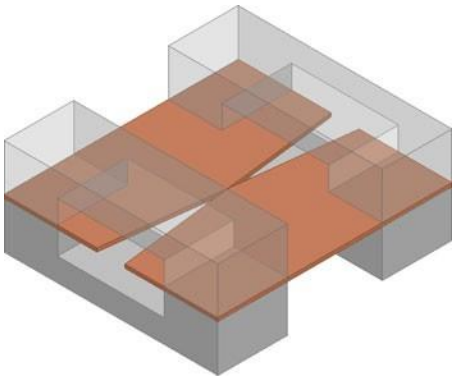

Fig. 4. Copper tapered thick slot waveguide supported by two Teflon braces. Braces are bolted together (not shown) though the conductors.

the waveguides performance:

$$\alpha_c = \frac{R_s}{\eta_0 d(z)} = \frac{1}{\eta_0 d(z)} \sqrt{\frac{\omega \mu_0}{2\sigma_{Cu}}}. \tag{1}$$

Our design differs from a slotline waveguide because the thickness of the metalization exceeds the wavelength for frequencies greater than 0.75 THz; hence the name, thick slot waveguide. Closed form solutions are not readily available for analysis of such a structure. Others who have investigated the effect of metal thickness on slotline operation have concluded that the metal thickness does not significantly affect the propagation constant[15]; this is consistent with the attenuation and pulse distortion seen in our experimental results discussed later. To mechanically support the structure illustrated in Fig. 2 a Teflon brace was used which is illustrated in Fig. 4; the bolts
fastening the structure have been omitted for clarity.

II. SIMULATION

Simulations of the tapered waveguide structure were completed using Ansys HFSS with a combination of solution techniques; standard frequency domain finite element method (FEM) and the transient analysis which utilizes the discontinuous Galerkin finite element method (DGTD). These solution types were selected due to their ability to accurately model geometries and closely model a THz pulse in the time domain.

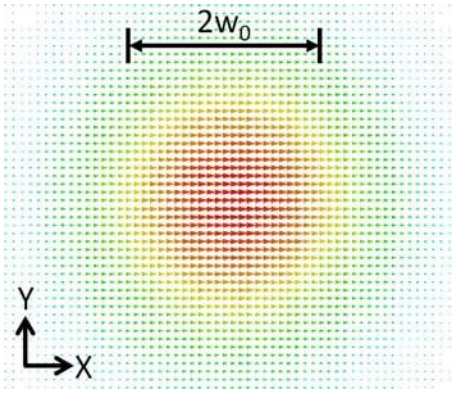

Fig. 5. Ideal Gaussian beam E-field profile at the waist of the THz beam.

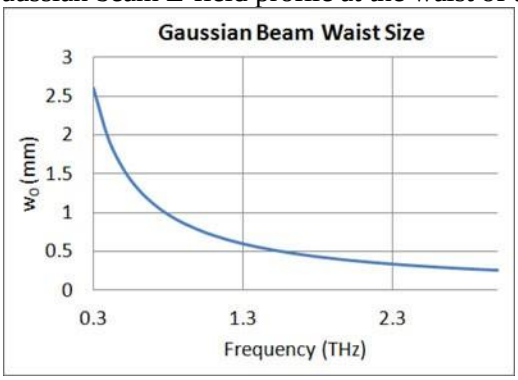

Fig. 6. Gaussian beam waist size (w0) versus frequency. Referring to Fig. 5 it becomes apparent that as the frequency increases, the THz waist intensity increases.

The simulations were excited using various sources depending on the goal. Waveport excitation was used when well-defined
conductor geometry permitted it. Incident wave (plane, Gaussian, spherical) excitation was used when it would closely model the experiment. Plane-wave excitations were for transient simulations. Simulation boundaries were commonly set to PML regions due to their ability to minimize reflections.

A. Field Coupling

Fig. 5 illustrates the idealized field profile at the focal point of the THz lens which is representative of the maximum field intensity attainable. Fig. 6 plots the Gaussian beam waist size, w0 , vs frequency using a THz lens with a convergence angle of
7◦. Fig. 7 illustrates the waveguides TE field profile for a few
discrete values of d(z).
Optimum coupling exists between the Gaussian beam and the waveguide when the field overlap is maximized. The overlap integral (Eqn. (2) [16]) can be interpreted visually by overlaying Fig. 5 onto Fig. 7(a) and approximating the similarities between the two field profiles:

$$\eta = \frac{|\int \vec{E}_1^* \vec{E}_2 dA|^2}{\int |\vec{E}_1|^2 dA \int |\vec{E}_2|^2 dA}. \tag{2}$$

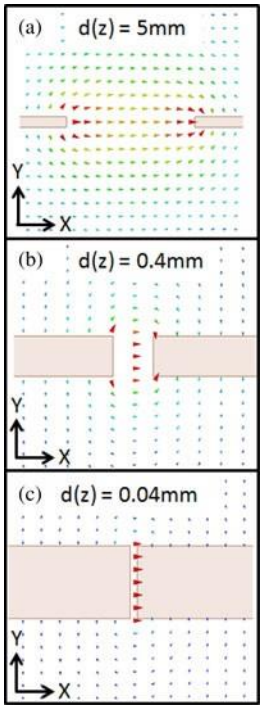

Fig. 7. The E-field profile for various plate separations, d(z), which correspond to different locations within the taper. It can be seen from these plots that field confinement is dependent on the d(z). Also to note is that a.) and b.) are better approximations to the Gaussian field plotted in Fig 5, hence coupling is dependent on d(z).

Our estimation for sufficient coupling was to locate the focal point where the plate separation was equal to the beam diameter, d(z) = 2w0 (2 THz). This estimation could be enhanced by vigorous analysis and optimization of Eqn. (2) and the respective co-directional and counter-directional coupled-wave equations. For this initial proof of concept design we did not deem this necessary due to the various complicated relationships which exist between the frequency dependent Gaussian beam wavefront and the fringing fields of the waveguide.

B. Field Enhancement

Using techniques similar to [1] and [2], we can provide field enhancement by coupling the radiated field into an adiabatic taper. For the waveguide, maximum field intensity occurs when the plate separation is at a minimum; similarly, for maximum field enhancement we want d(z) as small as possible. Using laser micromachining techniques it is possible to obtain a mini- mum plate separation of around 20 μm, although for our initial experiments we used a plate separation of 40 μm.

Fig. 8 pictorially illustrates the E-field enhancement achieved by the adiabatically tapering conductors. To provide a measure of achievable field enhancement the waveguide was implemented in a FEM simulation with a plane-wave excitation. Upon completion of the simulation Eqn. (3) was solved numerically where Ein and Eout represents the field at dmax and dmin ,

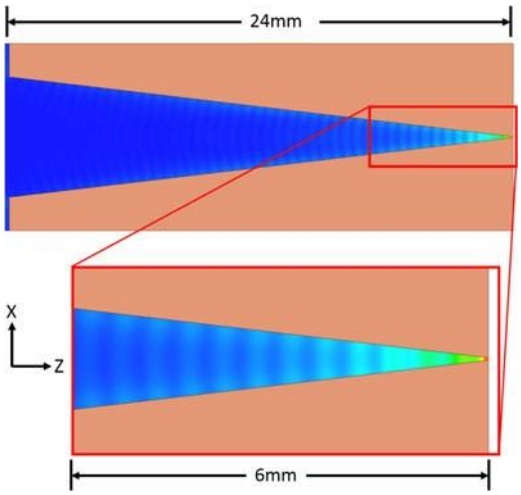

Fig. 8. FEM simulation which demonstrates the E-field enhancement for f = 0.3 THz. Note that this illustration only shows half the waveguide structure.

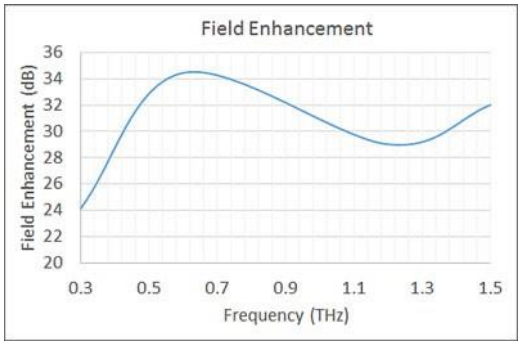

Fig. 9. FEM field enhancement simulation for f = 0.3–1.5 THz for dma x = 0.5 mm.

Respectively:

$$\frac{E_{\text{out}}}{E_{\text{in}}} = \frac{V_{\text{out}}/d_{\text{min}}}{V_{\text{in}}/d_{\text{max}}} = \frac{d_{\text{max}}}{d_{\text{min}}} \frac{\int_{l_{\text{out}}} \vec{E}_{\text{out}} \cdot dl}{\int_{l_{\text{in}}} \vec{E}_{\text{in}} \cdot dl}. \tag{3}$$

Due to the extremely large mesh sizes required to simulate the waveguide in its entirety, the simulation was truncated to dmax = 0.5 mm, where in reality dmax = 5 mm. This truncation means the simulation is simply an approximation, but it should not result in any significant errors since the TE field profile is well defined between the conductors. Fig. 9 plots the simulated results representing Eqn. (3), the average field enhancement is 30 dB. Referring to Eqn. (3) the enhancement scales with dmax , so it can be assumed that the structure likely provides a greater field enhancement than the simulation suggests.

C. Radiation Pattern

The waveguide has similar characteristics to the Gaussian beam since the input and output taper angles are matched to the respective convergence and divergence angles.

Also to note, it is rather important to maintain the divergence angle to ensure adequate focusing of the THz beam onto the receiver PCA. The main observable difference in the waveguide arises from the planar confinement geometry which doesn't affect the radiated field much providing the waveguide width, d(zout), is sufficient. To demonstrate this idea, Fig. 10 plots the simulated radiation patterns in the YZ-plane for a couple different values of the plate separation at the output. For values of d(zout) <w the radiation pattern in not as focused as for larger values where d(zout) > w. Therefore a rather simple criterion exists: d(zout) » w; for our experiments examined in the next section, d(zout) ≈ 12.5 w. Due to the existence of the bounding conductors, the radiation pattern in the XZ-plane (not illustrated) doesn't show similar beam deformation.

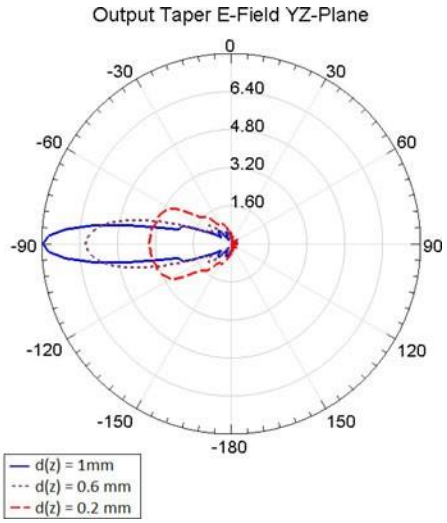

Fig. 10. Radiation patterns at f = 1 THz for various plate separations at the output taper. The plotted radiation patterns conclude to a rather intuitive result: the output taper should be designed to provide adequate directivity. This can be accomplished by tapering the conductors such that d(zout) » w

III. EXPERIMENT

A. Waveguide Fabrication

A femtosecond laser (Spectra-Physics Ultrafast Ti: Sapphire laser) was used to fabricate the tapered waveguide structure on a 0.4 mm thick copper sheet. The kilohertz ultrafast laser operating at 800 nm has the pulse duration of 120 femtosecond and a maximum average output power of 1 watt. A computer controlled electronic shutter and a motorized power attenuator was used to deposit adequate pulse energy into the work piece. To reduce heat affected zone and restrict the width of laser cut within 20 μm, the beam diameter was reduced from 6 to 2 mm using an iris diaphragm. The laser beam was focused using a microscope objective lens (magnification: 20×, numerical aperture: 0.42). The sample was mounted on a computer controlled 3-axis stage and the software, LaserCAM was used to generate scanning path of the laser head. The waveguide fabrication was done with an average laser power of 0.3 W (pulse energy of 300 μJ) and

scanning speed of 100 μm/sec using 20 passes, each vertically offset by 20 μm. To ensure desired machining accuracy, the micromachining process was monitored in-situ using a CCD camera.

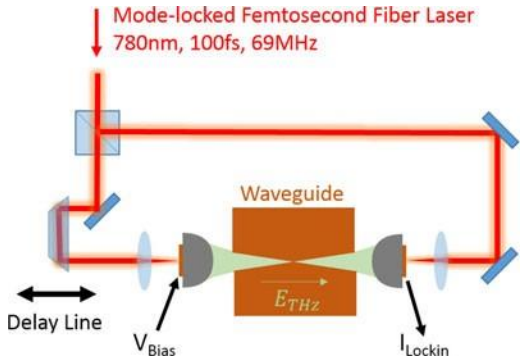

Fig. 11. The experimental setup used is similar to a typical THz-TDS setup, a key benefit for the tapered thick slot waveguide. To test the waveguide, it is simply placed in between two PCA's with Si focusing lenses and then translated and rotated to achieve maximum transmission.

B. Waveguide Testing

Fig. 11 illustrates the experiment setup. We start by splitting a mode-locked femtosecond laser pulse into two paths; one for the transmitter, the other for the receiver. The transmitter path passes through an optical delay line which becomes translated to obtain the THz pulses temporal response. The receiver path is directed to the receiver PCA to gate the antenna; the output of the receiver PCA is connected to current input on a lock-in amplifier.

For our experiments copper plates were placed perpendicular to the waveguide to scatter surface waves potentially excited by the Gaussian beam; therefore ensuring our experimental measurements were the result of the confined waveguide fields. The experimental spectral response for the waveguide in Fig. 12 demonstrates that the waveguide gives minimal pulse distortion and acceptable insertion losses (≈ 8 dB). The majority of the loss originates from sub-optimal coupling in and out the waveguide. Coupling loss could be decreased by increasing the waveguide thickness, w. The coupling enhancement would originate from greater field matching in the overlap integral [see Eqn. (2)]. Although greater coupling can be achieved, it comes at expense of decreased laser machining accuracy and more difficulty in integrating with small THz transceivers, trade-offs that require further consideration in future work. Even with an 8 dB insertion loss, the waveguide is capable of providing a localized 30 dB field enhancement which can be utilized to mitigate some of this loss irrespective of the coupling losses.

The dips in the spectral response in Fig. 12 correspond to water vapor absorption peaks; out of convenience we typically do not run experiments in a purged environment unless doing sensitive spectroscopy. These peaks are useful to precisely calibrate our spectral response by correlating with data obtained from the HITRAN database.

A comparison between the experiment and simulation results is seen by inspecting Figs. 12 and 13. The main point to observe is that pulse broadening and ringdown are minimal

in both experiment and simulation. This concept illustrates negligible dispersion and higher-order mode excitation; other literature [17] which focuses on exciting higher-order modes clearly illustrates the ringdown effect.

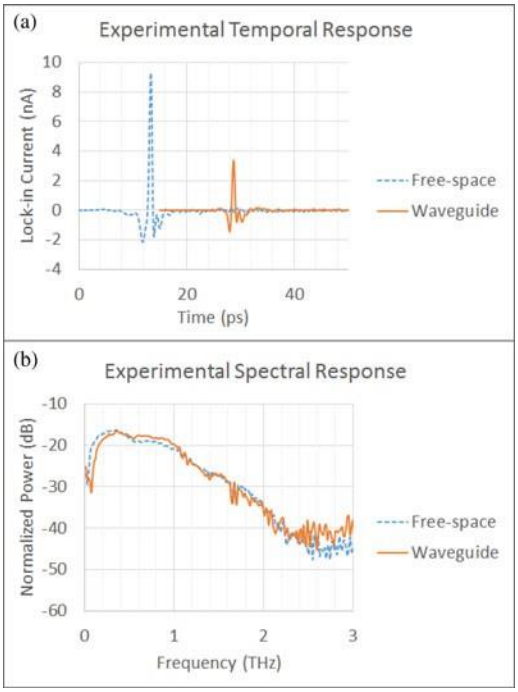

Fig. 12. Experiment: The received pulse when transmitted though free-space as a reference, and the received pulse when transmitted through the thick slot waveguide.

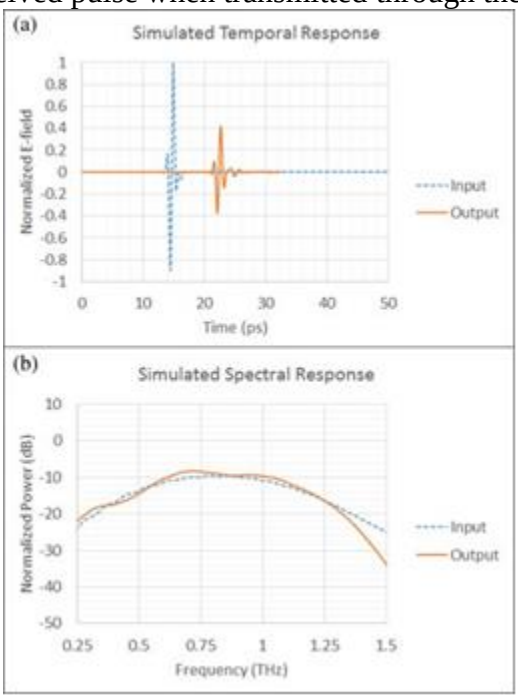

Fig. 13. DGTD simulation: The pulse at the input to the waveguide as a reference, and the pulse at the output of the thick slot waveguide.

experiment and simulation. This concept illustrates negligible dispersion and higher-order mode excitation; other literature [17] which focuses on exciting higher-order modes clearly illustrates the ringdown effect.

The differences between the experimental and simulation responses are attributed to different excitation sources and de- tection mechanisms. Due to software limitations the excitation source for the DGTD simulation is a Gaussian monopulse with a uniform wavefront; a cylindrical wavefront would provide a better approximation to the experiment. Experimental detection of the THz field is given by: $J(\nu) = \sigma s\ (\nu).ETHz(\nu)$, where $J(\nu)$, $\sigma s\ (\nu)$, and $ETHz(\nu)$ are the Fourier transforms of the photocurrent, surface conductivity, and THz field [18]. The simulation directly measures $ETHz(\nu)$ and is unaffected by the transient surface conductivity of the detector; thus a direct comparison cannot be made.

IV. DISCUSSION

Using the tapered thick slot waveguide in combination with commercial PCAs enables a simple method to generate high THz field intensities. A number of applications exist which can be enhanced by using this technique; such as spectroscopy, biomarker detection, non-linear THz applications, or high resolution surface imaging.

The results presented in this work show good agreement with theory; we have been able to successfully transmit THz pulses through laser machined waveguides. During the experiments it was found that alignment was simple in comparison to the free-space optics which we use regularly. This is likely due to the directive nature of the output taper as plotted in Fig. 10. In the free-space optical setup two PCAs are roughly aligned onto one another, then carefully tilted and adjusted to maximize the THz signal. Introduction of the waveguide allowed us to steer the THz beam by gently tilting the waveguide without need of realigning the laser on the receiving PCA.

Fig. 10 illustrates that the tapered thick slot waveguide can operate similar to an antenna. For our proof of concept design we didn’t do any extensive antenna optimization or beam shaping since we wanted broadband operation. Future tapered thick slot waveguides designed for continuous wave operation could shift the focus towards antenna design where existing frequency dependent antenna theory could be utilized.

Using a similar concept to the previous paragraph, frequency dependent waveguide structures could be machined into the tapered thick slot waveguide. For example, referring to the position of minimum plate separation, dmin ; it can be found for similar geometries ($d(z) \ll w$) eigenmodes are defined simply by existing parallel plate waveguide theory. Using mode-matching theory highly efficient filters, resonators, and power splitters can be machined into the waveguide and impedance matched to the tapered thick slot waveguide/antenna. Using a combination of these techniques antenna arrays can be developed to provide THz beam steering capabilities.

V. CONCLUSION

We have demonstrated experimentally our goal of coupling a commercial PCA to a tapered thick slot waveguide; the wave- guide provides significant field enhancement over a simple silicon lens according to theory and simulation. The tapered thick slot waveguide was designed specifically for field enhancement and coupling into and out of a commercial PCA [6]. Therefore, this waveguide may not operate identically across all manufactures designs, but the design process demonstrated in the work can be easily adjusted for other THz optics. The tapered thick slot waveguide simply consists of two tapers; adiabatic compression and expansion. This was done to provide a simple qualitative measure to the concept of planar waveguide structures. More advanced designs can be easily laser machined into planar conductors such as a filters or resonators. Using this waveguide in combination with microfluidic channels which traverse through the high field region could allow for simple small signature detection of both gas and liquid phase samples in a spectroscopy application.

REFERENCES

[1] H. Zhan, R. Mendis, and D. Mittleman, "Superfocusing terahertz waves below lambda/250 using plasmonic parallel-plate waveguides," Opt. Exp., vol. 18, pp. 9643–9650, 2010.
[2] K. Iwaszczuk, A. Andryieuski, A. Lavrinenko, X.-C. Zhang, and P. Jepsen, "Terahertz field enhancement to the MV/cm regime in a tapered parallel plate waveguide," Opt. Exp., vol. 20, pp. 8344–8455, 2012.
[3] H. Zhan, R. Mendis, and D. M. Mittleman, "Characterization of the tera- hertz near-field output of parallel-plate waveguides," JOSA B, vol. 28, pp. 558–566, 2011.
[4] J. Zhang and D. Grischkowsky, "Adiabatic compression of parallel-plate metal waveguides for sensitivity enhancement of waveguide THz time- domain spectroscopy," Appl. Phys. Lett., vol. 86, p. 061109, 2005.
[5] A. Shutler and D. Grischkowsky, "Gap independent coupling into parallel plate terahertz waveguides using cylindrical horn antennas," J. Appl. Phys., vol. 112, p. 073102, 2012.
[6] (2013). [Online]. Available: Batop. www.batop.com
[7] H. Kanaya, H. Shibayama, R. Sogabe, S. Suzuki, and M. Asada, "Funda- mental oscillation up to 1.31 THz in resonant tunneling diodes with thin well and barriers," Appl. Phys. Exp., vol. 5, 124101, 2012.
[8] H. Pahlevaninezhad, T. Darcie, and B. Heshmat, "Two-wire waveguide for terahertz," Opt. Exp., vol. 18, pp. 7415–7420, 2010.
[9] H. Pahlevaninezhad, B. Heshmat, and T. Darcie, "Efficient terahertz slot- line waveguides," Opt. Exp., vol. 19, pp. B47–B55, 2011.
[10] K. Wong, Planar Antennas for Wireless Communications. New York, NY, USA: Wiley, 2002.
[11] H. Pahlevaninezhad, "Design and implementation of efficient terahertz waveguides," Ph.D. dissertation, Dept. Electr. Comput. Eng., Univ. Victoria, Victoria, BC, Canada, 2012.
[12] H. Pahlevaninezhad, B. Heshmat, and T. Darcie, "Advances in terahertz waveguides and sources (invited paper)," IEEE Photon. J., vol. 3, no. 2, pp. 307–310, Apr. 2011.
[13] B. Vidal, T. Nagatsuma, N. Gomes, and T. Darcie, "Photonic technologies for millimeter- and submillimeter-wave signals," Advances Opt. Technol., vol. 2012, pp. 1–18, 2012.
[14] D. Pozar, Microwave Engineering, 4th ed. New York, NY, USA: Wiley, 2011.
[15] T. Kitazawa, Y. Fujiki, Y. Hayashi, and M. Suzuki, "Slotline with thick metal coating," IEEE Trans. Microw. Theory Tech., vol. 21, no. 9, pp. 580–582, Sep.1973.

[16] R. Paschotta, Encyclopedia for Photonics and Laser Technology. New York, NY, USA: Wiley.
[17] R. Mendis and D. Mittleman, "Comparison of the lowest-order transverse- electric (te1) and transverse-magnetic (tem) modes of the parallel-plate waveguide for terahertz pulse applications," Opt. Exp., vol. 17, pp. 14839– 14850, 2009.
[18] Y.-S. Lee, Principles of Terahertz Science and Technology. New York, NY, USA: Springer, 2008

Appendix D: THz-TDS Using a Photoconductive Free-Space Linear Tapered Slot Antenna Transmitter

(2016, IEEE PHOTONICS TECHNOLOGY LETERS)

Submitted

The manuscript was written by Levi Smith. Sample fabrication was done by Levi Smith. Measurements were done by Levi Smith and Afshin Jooshesh. The project was founded and supported by Prof. T. Darcie.

THz-TDS Using a Photoconductive Free-Space Linear Tapered Slot Antenna Transmitter

Levi Smith, Afshin Jooshesh, and Thomas Darcie, Fellow, IEEE

Abstract—A photoconductive free-space linear tapered slot antenna has been constructed as a planar alternative to the standard photoconductive switch coupled to a high resistivity silicon substrate lens. Experimental results show that a 1.6 THz bandwidth with a ≈50dB dynamic range is achievable using a semi-insulating gallium arsenide substrate and copper conductors.

Index Terms—THz, THz-TDS, Terahertz, antenna, linear tapered slot antenna, LTSA.

I. INTRODUCTION

ERAHERTZ photoconductive (PC) switches have existed for a number of years and were investigated as early as 1984 [1]. In [1] two PC switches were placed on opposing sides of the same substrate and did not include free-space propagation. Afterwards extensive research pursued in free-space antenna design and optimization. At this point two approaches appeared for the radiating and focusing THz pulses: guided-wave electronic antennas [2][5] and optical lensing from a point source [6], [7]. Electronic antennas were found to distort the temporal THz pulse due to dispersion and reflections which limit the ability to function as a broadband THz spectrometer. In this letter we will investigate a hybrid between a substrate lens and a guided-wave electronic antenna termed a photoconductive free-space linear tapered slot antenna (PC-FS-LTSA) which can be used for THz time-domain spectrometry (THz-TDS).

II. DESIGN

Standard photoconductive antennas (PCAs) are commonly coupled to a high-resistivity float-zone (HRFZ) silicon lens to overcome the total internal reflection (TIR) of substrate back- face [8]. It is desirable to eliminate the need for a HRFZ-Si lens because they are costly, lossy, and introduce dispersion thus limiting the transmitted power and bandwidth. Here we focus on the design of a PC-FS-LTSA for THz generation as a potential alternative to the standard HRFZ-Si lens.

Fig. 1 illustrates the PC-FS-LTSA which consists of a photo-conductive active-area on SI-GaAs which is edge coupled to copper conductors (i.e. the FS-LTSA). The photoconductive active-area was pattered using standard UV-lithography and the metallization (15nm Ti, 150nm Au) was fabricated using E- beam deposition and lift-off. A SI-GaAs substrate was selected for its low-cost, high DC resistivity and high responsivity to 785nm [9].

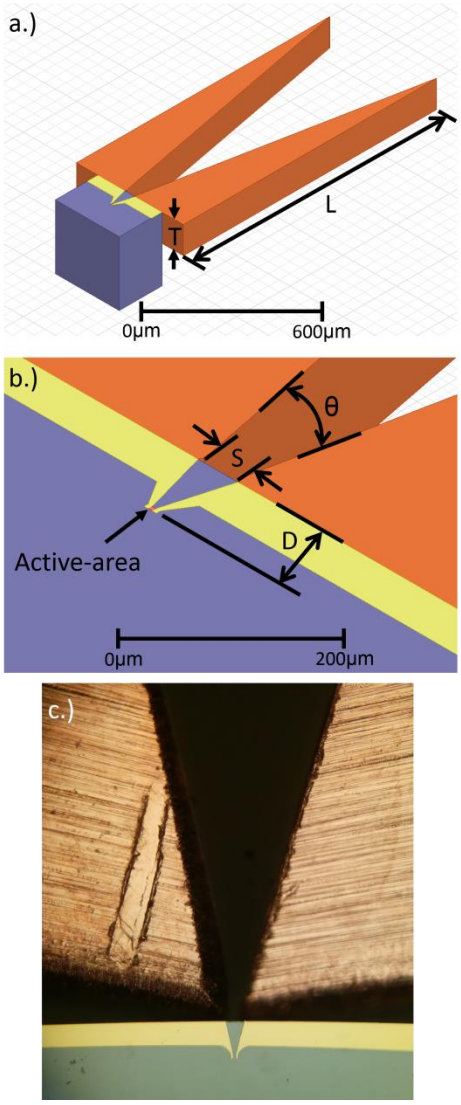

Fig. 1. Design of the PC-FS-LTSA. a) Overall structure b) Active-area to FS-LSTA c) Image of experimental structure where T≈127μm, S≈45μm, D≈85μm, L≈15mm, and θ ≈28◦.

The metallization pattern was selected to bias the active- area and guide the generated THz field into the FS-LTSA. It was found through simulation that the geometry illustrated in Figure 1b was able to couple to the FS-LTSA without significant pulse distortion. The FS-LTSA [8] is constructed out of a 127μm (0.005") thick copper sheet which was hand-cut and polished. Ideally the FS-LTSA should be thin (≈50μm) to reduce Fabry-Pe´rot resonances in the transverse plane (see Appendix A) but due to the limitations of hand-polishing this was found to be difficult. A FS-LTSA was selected (instead of a broadband Vivaldi taper [10]) for this proof-of-concept experiment for the manufacturing convenience. The FS-LTSA can be easily constructed by-hand whereas a Vivaldi taper requires precision micromachining.

A key difference between this work and past work [2]–[4] is the usage of a metallic slit based [11], [12] free-space LTSA. A free-space antenna has a number of advantages over planar substrate based antennas, namely, after the field is coupled to the FS-LTSA the

effect of substrate radiation, surface-waves, and dispersion are mostly eliminated. Another advantage is the reduction of conductor loss. Substrate-based antennas closely model coplanar strip transmission lines which have losses of ≈17dB/mm at 1 THz [13], whereas the metallic slit geometry has a loss of ≈0.35dB/mm at 1 THz [11]. To note, these numbers are not representative of all designs, but they illustrate the possible large difference between the expected loss.

The loss of a metallic slit waveguide is dependent on the conductor material, separation, and thickness. For the copper FS-LTSA used in this experiment a FEM simulation was used to estimate the loss. Given the FS-LTSA dimensions at the entrance to the antenna (T=127μm, S=45μm, f=1THz), the loss is ≈0.11dB/mm. As the FS-LTSA expands (S increases) the field localization on the conductors reduces resulting in a lower loss.

A. Simulation

The design of the PC-FS-LTSA was aided by simulations performed using Ansys HFSS's transient solver which utilizes the Discontinuous Galerkin Time Domain (DGTD) method. Key observations that resulted from the simulations were: the existence of a transverse Fabry-Pe´rot resonance in the FS- LTSA which will disperse the THz pulse (cavity length=T); a resonance between the PC active-area and the FS-LTSA edge (cavity length=D); combination of both cavities (cavity length = D+T); and when the active-area is not located at the end of an open-circuited transmission line then either half the power will be lost or resonances will occur. To summarize, the FS- LTSA should be thin and the active-area should be close to the substrate edge.

Fig. 2 illustrates the simulated E-field of the PC-FS-LTSA after transient excitation. Fig. 4 plots the simulated pulse shape at the output of the PC-FS-LTSA. The active-area in the simulation is modeled by a current pulse with a rise time of 800fs. The simulation illustrates that relatively few resonances are introduced by the waveguide and metalization geometries. To note the length, L, of the simulated structure is 2.25mm, whereas the experimental structure has a length of ≈15mm. The shorter length in the simulation was used to reduce the simulation time. This is not expected to have a large effect on THz pulse because as the conductors separation increases the field confinement on the conductors reduces resulting in a radiated wave [10].

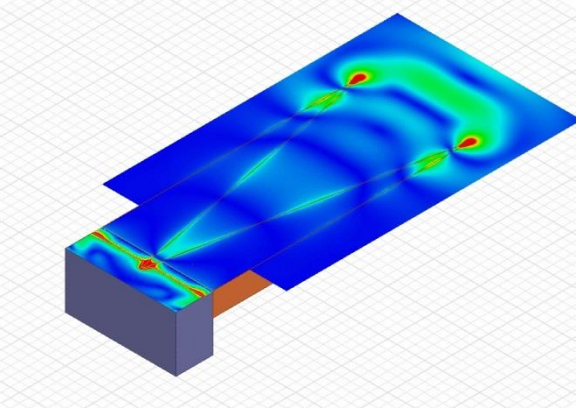

Fig. 2. Radiated field.

III. EXPERIMENT

We used a standard THz-TDS arrangement (Fig. 3) to investigate the PC-FS-LTSA's performance. A 1570nm fiber laser with a 100mW average power producing 100fs pulses at 38MHz was used. The 1570nm beam is frequency doubled using a periodically-polled lithium niobate (PPLN) crystal resulting in ≈20mW at 785nm to excite the experiment. Then the optical beam is split into two paths to excite the transmitter and gate the receiver. The transmitter optical beam path length can be varied using a mechanical delay line which is used to obtain the temporal response of THz field. The optical beam passes through an optical chopper, then afterwards the optical beam is focused onto the active-area to generate a THz field which is coupled to the FS-LTSA then radiated. Then the THz beam is passed through an iris to block or scatter off-axis wave-front components which increases the detectable bandwidth but reduces the detectable power. A portion of the THz beam reaches and biases the commercial LT-GaAs PCA receiver [14] which is detected by a lock-in amplifier.

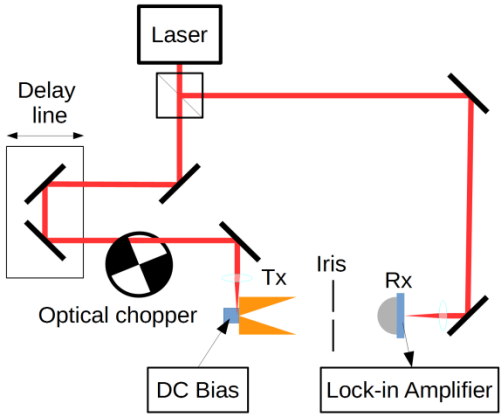

Fig. 3. Experimental setup for testing the PC-FS-LTSA. The active-area consisted of a 5×5μm area biased by 20Vdc. The average optical power focused onto the transmitter and receiver were 6mW and 7mW, respectively. The iris (opening = 5mm diameter) was placed midway between the trans- mitter and receiver which were separated by 10cm. The optical chopper was set at 1.1kHz. The receiver was connected to the current input of a lock-in amplifier.

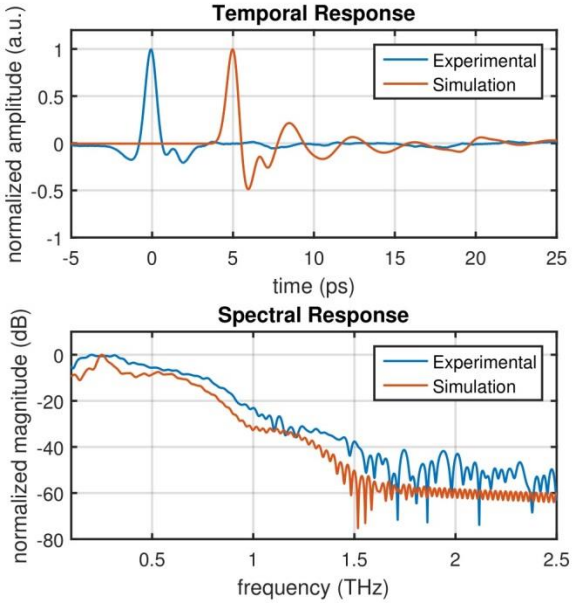

Fig. 4. Experimental and simulated response obtained from the setup illustrated in Fig. 3.

IV. DISCUSSION

Fig. 4 plots the result of the experiment illustrated in Fig. 3. The temporal response of the PC-FS-LTSA resembles that of a standard HRFZ-Si PCA which is desirable. The bandwidth of the PC-FS-LTSA is reaches around 1.6THz which is admirable considering the simplicity of the design. It is also expected that the PC-FS-LTSA should become lossy at higher frequencies due excitation of transverse Fabry-Pe´rot modes (see Appendix A).

A notable feature in Fig. 4 is the presence of the water vapor absorption lines which are observable around 1.26THz. Presence of these absorption lines indicate that the PC-FS-LTSA is capable of functioning as a THz-TDS source. It is required to note that these lines do not originate from the previously stated Fabry-Pe´rot resonance because the "cavity" has a low Q. When comparing the simulated and experimental results (Fig. 4) an obvious discrepancy is observed. For the simulated results the pulse has a strong negative portion whereas for the experiment this is minor. This is expected since the simulation defines the source as an impulse, whereas a SI-GaAs trans- mitter has a slow carrier decay (step-like response) resulting in a small negative peak [9]. Also note that the simulation peak at ≈0.255THz originates from a cavity (length=D+T, ne ≈ ./(12.9 + 1)/2 = 2.64) which is stronger for the simulated structure due to ideal edges. Referring to Fig. 4, a common trait of a LTSA is observed. After the initial transient, a small "double hump" occurs which is characteristic of the LTSA [2]. The double hump is undesirable because it broadens the pulse thus limiting the bandwidth. The simple method to eliminate this feature is to use a Vivaldi taper instead of a linear taper.

The bandwidth of the PC-FS-LTSA could be increased by correcting non-idealities with the following adjustments: utilize a thinner FS-LTSA (T≈50μm); reduce the distance between the active-area and the FS-LTSA (D≈10μm); and use a Vivaldi taper.

V. CONCLUSION

We have shown that the PC-FS-LTSA provides an alternative method to HRFZ-Si lensing for guiding and radiating a THz field produced by the photoconductive switching. Experimental results have shown that a ≈1.6THz bandwidth with a ≈50dB dynamic range can be achieved. Water vapor absorption lines can be resolved which confirms that the PC- FS-LTSA is a functional THz-TDS transmitter.
The PC-FS-LTSA allows for a planar THz setup which could be used for imaging or spectroscopy in a less bulky arrangement than current implementations which utilize PCAs coupled to a HRFZ-Si lenses.

APPENDIX A FABRY-PE´ ROT RESONANCE

The Fabry-Pe´rot modes can be excited when a thick (with respect to wavelength) metallic slit waveguide is used. Fig. 5 illustrates the results of a time-domain simulation that show the Fabry-Pe´rot resonance when the metallic slit is thick. The start and stop frequency of the excitation pulse are
0.3 and 3THz respectively. Fig. 6 illustrates the removal of the resonance by reducing the thickness of the metallic slit waveguide. Fig. 6b illustrates the desired undistorted response.

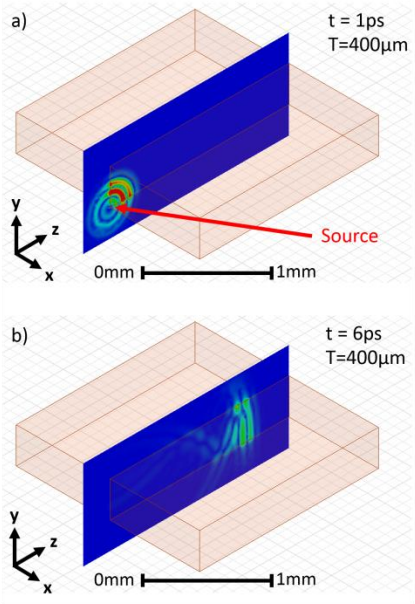

Fig. 5. Transient E-field plot illustrating the Fabry-Pe´rot resonance for a thick (T=400µm, Δν=0.375THz) metallic slit waveguide. a) Field profile around the source location just after excitation (t=1ps) b) Field profile of guided-wave after 6ps, note that the field profile is dispersed by reflections.

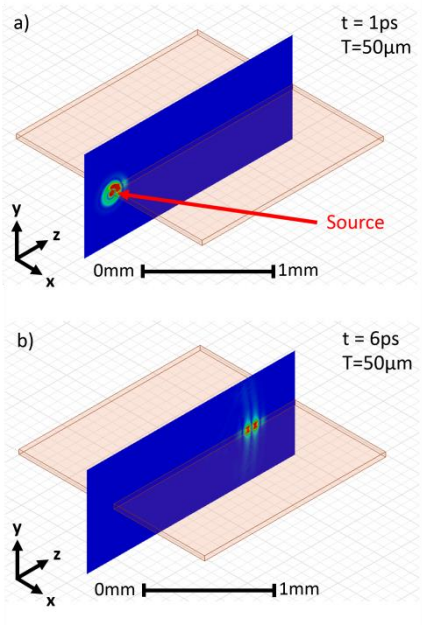

Fig. 6. Transient E-field plot illustrating the removal of the Fabry-Pe´rot resonance by reducing the thickness (T=50µm, Δν=3THz) of the metallic slit waveguide, a) Field profile around the source location just after excitation (t=1ps) b) Field profile of guided-wave after 6ps, note that the field profile is relatively undispersed and confined to the waveguide.

REFERENCES

[1] D. H. Auston, K. P. Cheung, and P. R. Smith, "Picosecond photocon- ducting hertzian dipoles," Appl. Phys. Lett., vol. 45, p. 284, 1984.
[2] A. P. DeFonzo, M. Jarwala, and C. Lutz, "Transient response of planar integrated optoelectronic antennas," Appl. Phys. Lett., vol. 50, p. 1155, 1987.
[3] A. P. DeFonzo and C. R. Lutz, "Optoelectronic transmission and reception of ultrashort electrical pulses," Appl. Phys. Lett., vol. 51, p. 212, 1987.
[4] Y. Pastol, G. Arjavalingam, J. Halbout, and G. Kopcsay, "Characteri- sation of an optoelectronically pulsed broadband microwave antenna," Electronics Letters, vol. 24, pp. 1318–1319, 1988.
[5] G. Rebeziz, "Millimeter-wave and terahertz integrated circuit antennas," Proceedings of the IEEE, vol. 80, 1992.
[6] C. Fattinger and D. Grischkowsky, "Point source terahertz optics," Appl. Phys. Lett., vol. 53, p. 1480, 1988.
[7] C. Fattinger. and D. Grischkowsky, "Terahertz beams," Appl. Phys. Lett., vol. 54, p. 490, 1989.
[8] D. Rutledge, "Integrated Circuit Antennas," in Infrared and Millimeter Waves, vol. 10, Millimeter Components and Techniques, Part II, K. J. Button, Ed. New York: Academic, 1983.
[9] M. Tani, S. Matsuura, K. Sakai, and S. Nakashima, "Emission charac- teristics of photoconductive antennas based on low-temperature-grown gaas and semi-insulating gaas," Applied Optics, vol. 36, pp. 7853–7859, 1997.

[10] D. Schaubert, E. Kollberg, T. Korzeniowski, and T. Thungren, “Endfire tapered slot antennas on dielectric substrates,” IEEE Transactions on Antennas and Propagation, vol. 33, pp. 1392 – 1400, 1985.
[11] M. Wchter, M. Nagel, and H. Kurz, “Metallic slit waveguide for dispersion-free low-loss terahertz signal transmission,” Applied Physics Letters, vol. 90, p. 061111, 2007.
[12] L. Smith, F. Ahmed, A. Jooshesh, J. Zhang, M. Jun, and T. Darcie, “Thz field enhancement by antenna coupling to a tapered thick slot waveguide,” Journal of Lightwave Technology, vol. 32, pp. 3676–3682, 2014.
[13] M. Y. Frankel, S. Gupta, J. A. Valdmanis, and G. A. Mourou, “Terahertz attenuation and dispersion characteristics of coplanar transmission lines,” IEEE Transactions on Microwave Theory and Techniques, vol. 39, pp. 910 – 916, 1991.
[14] Batop, www.batop.com.